AN EXPERIMENTAL STUDY OF THE DESIGN AND OVERLOAD CAPACITY OF STRUCTURAL GRILLAGES SUBJECTED TO ICE LOADS

By

© Hyunmin Kim, B.Sc.

A thesis submitted to the School of Graduate Studies

in partial fulfillment of the requirements for the degree of

Master of Engineering

Faculty of Engineering and Applied Science

Memorial University of Newfoundland

October 2014

St. John's Newfoundland and Labrador

ABSTRACT

It is well known that the design limit states for plating and framing of Polar Class ships are based on simplified plastic collapse mechanisms which ignore the beneficial effect of membrane stress and strain hardening; therefore, real structure will have a substantial reserve capacity beyond the design point. However, it is challenging to quantitatively estimate the level of the reserve capacity.

Significant research efforts have been carried out to further understand the interaction between ice and ship structures. However, most experimental studies of structural response have used steel plates or rigid indenters for ice loading rather than real ice. Similarly most ice crushing tests use rigid indenters to crush ice as opposed to compliant structures. However, while the results of previous experiments and simulations well present post-yield behavior of the grillage with rigid indenter, there was no insight in terms of the interaction between ice and ship structures.

In this study, laboratory grown conical shaped ice samples (1 m diameter) were used to load structural grillages, typical of a transversely framed 10,000 ton Ice Class PC6 midbody ice belt arrangement, well beyond its yield point and design point. This allowed for investigation into structural deformation considering the failure of ice. Two large grillages (named #1 and #2 respectively) were tested with ice specimens in a quasi-static condition (0.5 mm per second). The tests on Grillage #1 were performed in two load steps at identical loading positions in the midspan of the central stiffener and aimed at studying the ultimate load-carrying capacity of the grillage. The tests on Grillage #2 were carried out in three load steps at different loading positions along the span of the central stiffener;

right off-centre (330 mm away from the centre), centre, and left off-centre (330 mm away from the centre). The varying locations of Grillage #2 tests were intended to investigate the effect of damage at nearby locations on capacity of the structure.

These experiments suggest that local deformations of up to 11 % of the frame span and prior deformations nearby loading locations will not compromise the overall strength of the ship.

A finite element (FE) model was developed to analyze the experiments numerically. The load-deflection curves and deformation shapes measured by the MicroScribe® were used to validate the numerical results. The FE analysis results show strong agreement with the physical experiments and demonstrate that FE model can be used for analysis of an ice-strengthened ship structures subjected to extreme ice loading.

This thesis describes the procedure of the large grillage tests, discusses the results and pressure-area relationships, and compares against non-linear finite element analysis in conjunction with load-deflection curves and deformed shapes of the grillage. Each chapter presents several plots of data obtained from the experiments and uses photos to support the discussion of the results.

ACKNOWLEDGEMENTS

This thesis would be impossible without the help and support from a few great people. I would like to state my great gratitude to the following:

Dr. Claude Daley, my supervisor, professor at MUN, principal investigator of the STePS^2 Research Project, for his excellent direction, financial support, enthusiasm, and guidance.

Dr. Bruce Colbourne, professor at MUN, co-investigator and project manager of the STePS^2 Research Project, for your kindness and support throughout the research.

Dr. Phani Suresh Reddy Gudimetla, a fellow post doctorial researcher, for your wonderful help and support.

Mr. Matt Curtis, Lab. technologist of the Structures Laboratory, for wonderful help and support during the physical experiments.

Mr. JoongHyo Choi, a fellow graduate student at my office, for your remarkable help and knowledge.

Mr. John Dolny and Mr. Dan Oldford, researchers at the ABS Harsh Environment Technology Center, for your outstanding help.

I am also thankful to the STePS^2 research program for their generous financial support.

Lastly, I would like to thank my family for your unconditional support.
This thesis is dedicated to you.

Table of Contents

ABSTRACT i
ACKNOWLEDGEMENTS iii
Table of Contents iv
List of Tables vii
List of Figures viii
Nomenclature and Abbreviations xvi
List of Symbols xvii
1 INTRODUCTION 1
1.1 Scope and Objectives 2
1.2 IACS Unified Requirement for Polar Class ships 3
1.3 Design Ice Loads 5
1.4 Ice-Structure Interaction 14
1.5 Framing Design Cases and Mechanisms 17
1.5.1 Assumptions 17
1.5.2 Bending and Shear Interaction 17
1.5.3 Limits States 19
1.5.4 Limit State Equations 20
1.6 Previous Physical Grillage Experiments 24
1.7 Non-linear Finite Element Method 26
1.7.1 Solutions for Nonlinearities 27
1.7.2 Hardening Rules 29
2 LARGE GRILLAGE EXPERIMENTS 31
2.1 Introduction 31
2.2 Geometry 32
2.3 Test Preparation 34
2.3.1 Ice Specimen Preparation 35
2.3.2 Marking the Grillages 37

2.3.3 Data Acquisition System 38
2.3.4 Strain Gauges and LVDT 39
2.3.5 Position Transducers ('yo-yo' pots) and Pressure Transducer 41
2.3.6 Recording and Display Systems 42
2.3.7 Handling and Positioning Ice Samples 44
2.3.8 Digitizing Deformation using the MicroScribe® 3D Digitizer 45
2.4 Boundary Conditions 46
2.5 Loading Scenarios 48
2.5.1 G1T1 & G1T2 (Centre Loading Case) 48
2.5.2 G2T1, G2T2, and G2T3 (Off-Centre and Centre Loading Cases) 49
2.6 Summary of Experiments 51
3 ANALYSIS OF EXPERIMENTAL RESULTS 52
3.1 Introduction 52
3.2 Framing Design in the Unified Requirements 53
3.3 Grillage #1 56
3.3.1 G1T1 Result 56
3.3.2 G1T2 Result 64
3.3.3 Discussion of Grillage #1 73
3.4 Grillage #2 75
3.4.1 G2T1 Result 75
3.4.2 G2T2 Result 80
3.4.3 G2T3 Result 86
3.4.4 Discussions of Grillage #2 91
3.5 Discussions of Grillage #1 and #2 94
3.5.1 G1T1 and G2T1 (Comparison of different initial loading positions) 94
3.5.2 G1T2 and G2T2 (Comparison of different prior loading positions) 95
3.5.3 G2T1 and G2T3 (Comparison of symmetric loading positions) 96
3.6 Pressure-area Curves with Varying Calculation Methods for Contact Area 97

3.6.1 Pressure-area Interaction 97
3.6.2 Nominal Area Calculation 99
3.6.3 Nominal Area Calculation Considering Structural Deformation 102
3.6.4 Direct Measurement of the Contact Face 106
3.6.5 Discussions 108
3.7 Uniaxial Material Tensile Tests 110
3.8 Conclusion 114
4 NON-LINEAR FINITE ELEMENT ANALYSIS 116
4.1 Introduction 116
4.2 Structural Idealization 117
4.2.1 Structural Modeling 117
4.2.2 Element Type and Meshing 118
4.3 Material Property Model 119
4.4 Boundary Conditions 120
4.5 Loading 121
4.6 FE Analysis Results 124
4.6.1 Grillage #1 124
4.6.2 Grillage #2 128
4.7 Conclusion 133
5 CONCLUSIONS AND RECOMMENDATIONS 135
5.1 Conclusions 135
5.2 Recommendations 140
Bibliography 142
Appendix A: Load-Strain Curves of Grillage #1 146

List of Tables

Table 1-1: Polar Classes Descriptions (IACS, 2007).....4

Table 2-1: Ice sample parameters 35

Table 2-2: Description of the position transducers 41

Table 2-3: List of the large grillage tests 51

Table 3-1: Sample calculations for limit loads 55

Table 3-2: Summary of the pressure-area curves.....109

Table 3-3: Summary of direct measurements of the contact face.....109

Table 3-4: Summary of the uniaxial material tensile tests.....111

Table 3-5: True stress-strain properties 112

Table 4-1: Material parameters.....119

List of Figures

Figure 1-1: Design scenario - glancing collision on shoulder 5

Figure 1-2: Design scenario - flexural failure during glancing collision 6

Figure 1-3: Nominal contact geometry during oblique collision with an ice edge 7

Figure 1-4: Definition of hull angles. 7

Figure 1-5: Load patch shape from triangular to rectangular 11

Figure 1-6: Nominal and design rectangular load patches 12

Figure 1-7: Ice load patch configuration 13

Figure 1-8: Peak Pressure Factor used to design individual elements. 13

Figure 1-9: Sketch of ice contact with a ship structure (Daley, 2004) 14

Figure 1-10: Types areas and pressures related to pressure-area data (Daley, 2004) 15

Figure 1-11: Sketch of ice pressure and the meaning of a spatial pressure-area plot (Daley, 2004) 15

Figure 1-12: Sketch of measured ice pressure data and process pressure-area plots (Daley, 2004) 16

Figure 1-13: Bending/shear interaction diagrams 18

Figure 1-14: The 3 limit states considered for frames 19

Figure 1-15: Difference between linear and non-linear response 26

Figure 1-16: Newton-Raphson method (SolidWorks) 28

Figure 1-17: Modified Newton-Raphson method (SolidWorks) 28

Figure 1-18: Application example of the arc length method (SolidWorks) 29

Figure 1-19: Stress-strain behavior for isotropic hardening (ANSYS) 29

Figure 1-20: Stress-strain behavior for linear kinematic hardening (ANSYS) 30

Figure 2-1: Grillage test apparatus 31

Figure 2-2: Geometry of the large grillage 33
Figure 2-3: Test preparation.....34
Figure 2-4: Ice sample ready for shaping.....36
Figure 2-5: Shaping the ice sample.....36
Figure 2-6: Marking lines on the grillage 37
Figure 2-7: Data acquisition system 38
Figure 2-8: National Instruments® data acquisition devices 38
Figure 2-9: Arrangement of strain gauges and LVDT.....39
Figure 2-10: Strain gauges on the grillage 40
Figure 2-11: LVDT mounted on the instrument frame.....40
Figure 2-12: Arrangement of position transducers 41
Figure 2-13: The hydraulic ram outfitted with the pressure transducer and position transducer 42
Figure 2-14: Schematic arrangement of the recording and display systems.....43
Figure 2-15: Ice sample fitted into the forklift's fork extension.....44
Figure 2-16: Handling an ice sample using a forklift and overhead crane 44
Figure 2-17: MicroScribe® (Solution Technologies Inc.).....45
Figure 2-18: Scanning deformation using the MicroScribe® 45
Figure 2-19: Boundary conditions at the longitudinal ends.....47
Figure 2-20: Boundary conditions at the stringer ends.....47
Figure 2-21: G1T1 & G1T2 center loading setup.....48
Figure 2-22: The first test of Grillage #2 (G2T1) - right off-centre loading case.....50
Figure 2-23: The second test of Grillage #2 (G2T2) - centre loading case 50

Figure 2-24: The third test of Grillage #2 (G2T3) - left off-centre loading case.....50
Figure 3-1: Deformed shape of G1T1 using the MicroScribe® 57
Figure 3-2: Cross section view of G1T1.....57
Figure 3-3: Load-deflection curve of G1T1.....58
Figure 3-4: Deformation of the grillage support frame of G1T1.....58
Figure 3-5: Isometric view of G1T1 at 2.1 MN.....59
Figure 3-6: Side view of G1T1 at 2.1 MN.....59
Figure 3-7: Inside view of G1T1 at 2.1 MN 60
Figure 3-8: General view of G1T1 at 2.1 MN 60
Figure 3-9: Central longitudinal stiffener web.....61
Figure 3-10: Surface crack in the weld 61
Figure 3-11: Deformation of G1T1.....62
Figure 3-12: Inside view of the grillage support frame after unloading 62
Figure 3-13: Longitudinal stiffeners of G1T1 63
Figure 3-14: Distortion of longitudinal stiffeners near the stringer.....63
Figure 3-15: Deformed shape of G1T2 using the MicroScribe® 66
Figure 3-16: Cross section view of G1T2.....66
Figure 3-17: Load-deflection curve of G1T2.....67
Figure 3-18: Deformation of the grillage support frame of G1T2.....67
Figure 3-19: Isometric view of G1T2 at 2.8 MN.....68
Figure 3-20: Side view of G1T2 at 2.8 MN.....68
Figure 3-21: Inside view of G1T1 at 2.8 MN 69
Figure 3-22: General view of G1T2 at 2.8 MN 69

Figure 3-23: Surface crack in the end of the central longitudinal frame 70
Figure 3-24: Surface crack in the end of the central longitudinal frame 70
Figure 3-25: Distortion at the end of the longitudinal stiffeners 71
Figure 3-26: Deformation of the longitudinal stiffeners 71
Figure 3-27: Deformation of the cut-out of the stringer 72
Figure 3-28: Load-deflection curves of Grillage #1 tests 73
Figure 3-29: Deformed shape of G2T1 using the MicroScribe® 76
Figure 3-30: Cross section view of G2T1 76
Figure 3-31: Load-deflection curve of G2T1 77
Figure 3-32: Deformation of the grillage support frame of G2T1 77
Figure 3-33: Side view of G2T1 at 2.3 MN 78
Figure 3-34: General view of G2T1 at 2.3 MN 78
Figure 3-35: Deformation of G2T1 79
Figure 3-36: Deformed shape of G2T2 using the MicroScribe® 81
Figure 3-37: Cross section view of G2T2 81
Figure 3-38: Load-deflection curve of G2T2 82
Figure 3-39: Deformation of the grillage support frame of G2T2 82
Figure 3-40: Isometric view of G2T2 at 2.1 MN 83
Figure 3-41: Side view of G2T2 at 2.1 MN 83
Figure 3-42: Inside view of G2T2 at 2.1 MN 84
Figure 3-43: General view of G2T2 at 2.1 MN 84
Figure 3-44: Deformation of G2T2 85
Figure 3-45: MicroScribe® points of the deformed shape of G2T3 87

Figure 3-46: Cross section view of G2T3 87
Figure 3-47: Load-deflection curve of G2T3 88
Figure 3-48: Deformation of the grillage support frame of G2T3 88
Figure 3-49: Isometric view of G2T3 at 2.3 MN 89
Figure 3-50: Side view of G2T3 at 2.3 MN 89
Figure 3-51: Inside view of G2T3 at 2.3 MN 90
Figure 3-52: General view of G2T3 at 2.3 MN 90
Figure 3-53: Load-deflection curves of Grillage #2 Tests 91
Figure 3-54: Load-deflection curves of Grillage #2 Tests (G2T2 and G2T3 considers prior test deformation) 92
Figure 3-55: Consecutive section views at the right off-centre position 92
Figure 3-56: Consecutive section views at the midspan 93
Figure 3-57: Consecutive section views at the left off-centre position 93
Figure 3-58: G2T1 in comparison with G1T1 94
Figure 3-59: G1T2 in comparison with G2T2 95
Figure 3-60: G2T1 in comparison with G2T3 96
Figure 3-61: Ice and structure interaction of G1T1 98
Figure 3-62: Schematic of the calculation method based on the nominal area 99
Figure 3-63: Nominal pressure-area curves of Grillage #1 100
Figure 3-64: Nominal pressure-area curves of Grillage #2 101
Figure 3-65: Schematic of nominal area considering structural deformation 102
Figure 3-66: Ram stroke displacement and structural deformation of G2T1 103
Figure 3-67: Nominal pressure-area curves considering deformation of Grillage #1 104

Figure 3-68: Nominal pressure-area curves considering deformation of Grillage #2 105
Figure 3-69: Schematic of the method based on direct measurements of the contact face 106
Figure 3-70: Ice sample after unloading 107
Figure 3-71: Measurement of the diameter.....107
Figure 3-72: Pressure-area plot of direct measurements of the contact face 107
Figure 3-73: Comparison with pressure-area data of the Polar Sea (Daley, 2004) 108
Figure 3-74: Engineering stress-strain and true stress-strain curves.....112
Figure 3-75: The end part of the grillage where the material test specimens were taken 113
Figure 3-76: Material test machine (left) and necking at a specimen (right).....113
Figure 3-77: Completed specimens 113
Figure 4-1: Extent of the structural model 117
Figure 4-2: SHELL181 model (ANSYS).....118
Figure 4-3: Bilinear elasto-plastic stress-strain curve.....119
Figure 4-4: Boundary conditions 120
Figure 4-5: Loading scheme in Grillage #1 122
Figure 4-6: Loading conditions of Grillage #1 122
Figure 4-7: Loading scheme in Grillage #2 123
Figure 4-8: Loading conditions of Grillage #2 123
Figure 4-9: Loading steps in Grillage #2 123
Figure 4-10: FEM load-deflection curves in comparison with the experimental results ...124
Figure 4-11: Cross section views of deformation between experiments and FEA of Grillage #1 125
Figure 4-12: Vertical deflection of G1T1 FEM at 2.1 MN.....126
Figure 4-13: Equivalent plastic strain of G1T1 FEM at 2.1 MN.....126

Figure 4-14: Vertical deflection of G1T2 FEM at 2.8 MN.....127
Figure 4-15: Equivalent plastic strain of G1T2 FEM at 2.8 MN.....127
Figure 4-16: FEM load-deflection curves in comparison with experimental results.....128
Figure 4-17: Cross section views of the FEM in comparison with the experimental results..129
Figure 4-18: Deformation of G2T1 FEM at 2.3 MN.....130
Figure 4-19: Deformed shape with equivalent plastic strain of G2T1 FEM 130
Figure 4-20: Deformation of G2T2 FEM at 2.1 MN.....131
Figure 4-21: Deformed shape with equivalent plastic strain of G2T2 FEM 131
Figure 4-22: Deformation of G2T3 FEM at 2.3 MN.....132
Figure 4-23: Deformed shape with equivalent plastic strain of G2T3 FEM 132

Figure A- 1: Module 1 of G1T1.....147
Figure A- 2: Module 2 of G1T1.....147
Figure A- 3: Module 3 of G1T1.....148
Figure A- 4: Module 4 of G1T1.....148
Figure A- 5: Module 5 of G1T1.....149
Figure A- 6: Module 6 of G1T1.....149
Figure A- 7: Module 7 of G1T1.....150
Figure A- 8: Module 8 of G1T1.....150
Figure A- 9: Module 9 of G1T1.....151
Figure A- 10: Module 1 of G1T2.....152
Figure A- 11: Module 2 of G1T2.....152
Figure A- 12: Module 3 of G1T2.....153

Figure A- 13: Module 4 of G1T2.....153
Figure A- 14: Module 5 of G1T2.....154
Figure A- 15: Module 6 of G1T2.....154
Figure A- 16: Module 7 of G1T2.....155
Figure A- 17: Module 8 of G1T2.....155
Figure A- 18: Module 9 of G1T2.....156

Nomenclature and Abbreviations

ABS	American Bureau of Shipping
ASPPR	Arctic Shipping Pollution Prevention Regulations
DOE	Design of Experiment
DOF	Degree of freedom
FE	Finite Element
FEM	Finite Element Method
FSICR	Finnish-Swedish Ice Class Rules
IACS	International Association of Classification Societies
IACS Polar Rules	IACS Unified Requirements for Polar Class Ships
IMO	International Maritime Organization
MicroScribe®	A 3D digitizing device
MUN	Memorial University of Newfoundland
PC	Polar Class
STePS^2	Sustainable Technology for Polar Ships and Structures
UR	Unified Requirement
USGS	United States Geological Survey
WMO	World Meteorological Organization

List of Symbols

E	Young's modulus (Modulus of elasticity)
M_e	Effective mass
V_n	Normal velocity
h_{ice}	Ice thickness
Z_p	Plastic section modulus
Z_{pns}	Reduced plastic section modulus
$\{F\}$	Nodal force
$\{D\}$	Nodal displacement
$[K]$	Stiffness matrix
$\{R\}$	Load vector
$\{D\}$	Translation in the x direction
E_h	Strain-hardening tangent modulus
F_n	Normal force
$P_{\_Asym}$	Pressure causing collapse for end load case
P_{1h}	Pressure causing collapse for case of 0 fixed supports
P_{2h}	Pressure causing collapse for case of 1 fixed supports
P_{3h}	Pressure causing collapse for case of 2 fixed supports
k_w	Area ratio
k_z	Ratio of z_p to Z_p
σ_T	Ultimate tensile strength

a	Length of shear panel
a_1	Ratio of min. to actual web area
A_1	Shear factor in rule modulus equation
A_{1A}	Shear factor for 3-hinge mechanism
A_{1B}	Shear factor for shear mechanism
A_f	Area of the flange
A_o	Minimum web area
A_w	Area of the web
b	Height of the ice load patch
h_w	Height of the web
k_{a1}	Modulus correction factor
L	Length of frame
M_p	Plastic moment for frame
m_p	Sum of plastic moments in plate and flange
M_{pr}	Reduced plastic moment
N	Shear force
P	Pressure
S	Frame spacing
t_f	Thickness of the flange
t_p	Thickness of the shell plating
t_w	Thickness of the web
w	Length of the ice load patch

w_f	Width of the flange
Z_p	Plastic section modulus
z_p	Sum of plastic section moduli of plate and flange
Zp_{reqd}	Required plastic section modulus
δ	Deflection of the frame
σ_y	Yield stress
fz	Function of k_z
j	Number of fixed supports
l	Direction cosine
v	Poisson's ratio
δ	Normal ice penetration
ε	Strain
σ	Stress

1 INTRODUCTION

Interest in the Arctic is developing in response to promising estimates of potential natural resources and the advantages of new shipping route.

The United States Geological Survey (USGS) released data that estimates the amount of hydrocarbon resources in the Arctic; 90 billion barrels of oil, 44 billion of NGLs and 1,669 trillion cubic feet of gas (Gautier et al., 2009). Evidence of global warming and receding ice are providing operators longer open water seasons and, improved technologies are allowing for oil drilling and gas extraction in the area. Increased investment into the Arctic has led to the development of more advanced system for exploration such as compatible drilling units, production facilities and associated marine support and transportation activity.

Transshipments along the Northern Sea Route (Russian Arctic) and to a lesser extent the Northwest Passage (Canadian Arctic) have been shown to be attractive alternatives to traditional shipping routes such as the Suez and Panama Canal. The Northern Sea Route has 1/3 shorter distance than the Suez Canal and the Northwest Passage provides a 7,000 km shorter distance than the Panama Canal. These alternative shipping routes can save on time, fuel consumption, and costs.

The increased demands in the Arctic require the development of robust ice-strengthened ships which can safely transit in these harsh environments. It is necessary to advance our understanding about ice-structure interactions which can help design more efficient structures against ice impacts. Plastic response of ship structures has been adapted for designing ships and offshore structures. The International Association of Classification

Societies (IACS) Requirements Concerning Polar Class (IACS Polar Rules) are based on plastic limit states for the scantling requirements of plating and framing (IACS, 2007). The IACS Polar Rules allow ship structures to be optimized for plastic failure rather than elastic failure, resulting in a lighter and stronger ship design. The rationale of plastic limit states is the recognition that structures tend to have a large reserve capacity in the post yield region. Using some portion of the reserve capacity will lead to more efficient and producible design. However, it is challenging to quantitatively estimate the level of the reserve capacity.

1.1 Scope and Objectives

The present study is concerned with estimating the ultimate load-carrying capacity of a structural grillage subject to ice loading and understanding the effect of prior deformations at nearby locations on the capacity of the grillage. The objective of this thesis is to predict plastic response and quantify reserve capacity of structural grillages subject to ice loading through physical experiments and numerical analysis. This thesis consists of five main chapters. In addition the previous introduction, Chapter 1 provides a brief literature review of the subject matter. The IACS Unified Requirement for Polar Class Ships and ice-structure interaction are outlined and derivations of design ice loads and framing limit states are provided. Previous physical grillage experiments are described and non-linear finite element analysis methods are briefly introduced. Chapter 2 describes the preparation of the large grillage physical experiments in detail. Chapter 3 outlines the results of physical experiments together with a sample calculation of limit states, load-deflection curves, deformed shapes of the grillage, pressure-area relationships

and material tensile tests. The results from the experiments are compared with a numerical finite element analysis in chapter 4. Finally, chapter 5 concludes this thesis and presents recommendations for future research. Appendix-A presents the load-strain curves obtained from measurements of Grillage #1.

1.2 IACS Unified Requirement for Polar Class ships

A new International Association of Classification Societies (IACS) standard for Polar Ship design, in the form of a Unified Requirement has been developed by an international committee with representatives from many classification societies and participation of several polar nations (IACS, 2007). The IACS Polar Rules are a construction standard that prescribes minimum scantlings through a set of design ice load and structural formulae. Traditional design rules are based on the allowable stress method that is usually based on successful similar past experience to keep the stresses below yield when subject to design loads.

In contrast, the IACS Polar Rules are based on plastic limit states design which was developed by analytical solutions of plastic collapse mechanisms using energy methods. The descriptions of the polar classes are given in Table 1-1. The ice classes are described based on the operational period and ice condition to be encountered. The PC1 class ship can operate year round in all polar waters while the lower classes are intended for light ice conditions. Kendrick (2000) carried out a comprehensive comparison between requirements of the IACS Polar Rules and Finnish-Swedish Ice Class Rules (FSICR). It was found that the lowest the IACS Polar Rules (PC6 & PC7) are normally equivalent to

the highest FSICR (1A Super & 1A), respectively. It is likely that the IACS Polar Rules are based on calibrating existing rules from Canada, Russia and Finland-Sweden.

Table 1-1: Polar Classes Descriptions (IACS, 2007)

Polar Class	Ice Description (based on WMO Sea Ice Nomenclature)
PC1	Year round operation in all Polar Waters
PC2	Year round operation in moderate multi-year ice conditions
PC3	Year round operation in second year ice which may include multi-year ice inclusions
PC4	Year round operation in thick first year ice which may include old ice inclusions
PC5	Year round operation in medium first year ice which may include old ice inclusions
PC6	Summer/Autumn operation in medium first year ice which may include old ice inclusions
PC7	Summer/Autumn operation in first year ice which may include old ice inclusions

1.3 Design Ice Loads

The design ice load formulations were derived by Daley (2000) and repeated here. This procedure is later used to calculate the design ice loads when checking for compliance with IACS Polar Rules.

A glancing collision on the shoulders of the bow was used to form the basis of the ice loads for plating and framing design as shown in Figures 1-1 and 1-2. In the scenario, it was assumed that the ship is moving forward at the design speed, striking an angular ice edge. Throughout the collision, the ship penetrates the ice and rebounds away. The ship speed, ice thickness and ice strength are supposed to be class dependent. Through equating the normal kinetic energy with the energy used to crush the ice, the maximum force can be obtained. Therefore, the ice crushing force cannot exceed the force required to fail the ice in bending. The combination of collision angles, ice strength and thickness limit the force due to bending.

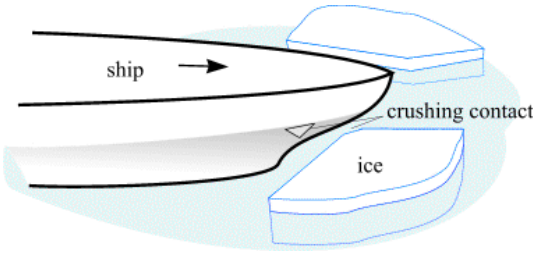

Figure 1-1: Design scenario - glancing collision on shoulder

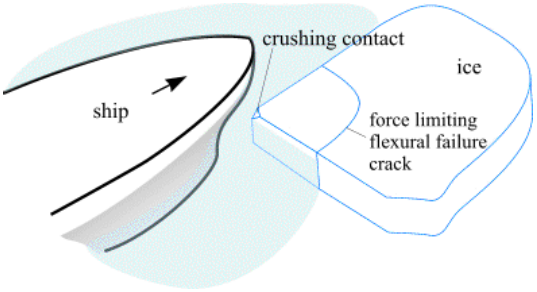

Figure 1-2: Design scenario - flexural failure during glancing collision

The ice load is derived for an oblique collision on the bow. The ice load model assumes a 'Popov' type of collision (Popov et al., 1967) with ice indentation described by a pressure-area relationship (Kendrick & Daley, 1998).

The force can be found by equating the normal kinetic energy with the ice crushing energy;

$$KE_n = E_{crush} \tag{1.1}$$

The crushing energy can be found by integrating the normal force over the penetration depth;

$$E_{crush} = \int_0^{\delta} F_n(\delta) \cdot d\delta \tag{1.2}$$

The normal kinetic energy combines the normal velocity with the effective mass at the collision point;

$$KE_n = \frac{1}{2} M_e \cdot V_n^2 \tag{1.3}$$

Combining these two energy terms;

$$\frac{1}{2} M_e \cdot V_n^2 = \int_0^{\delta m} F_n(\delta) \cdot d\delta \tag{1.4}$$

Using the ice penetration geometry with the pressure-area relationship, the force can be found. The nominal area is found for a penetration δ (see Figure 1-3).

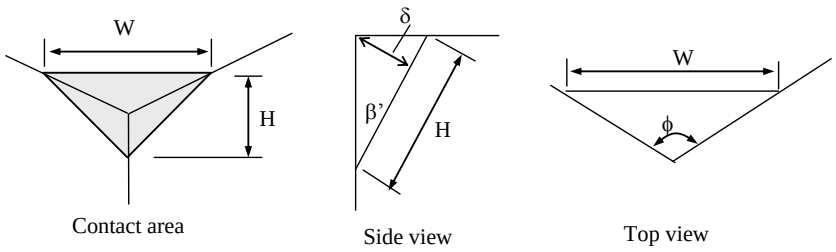

Figure 1-3: Nominal contact geometry during oblique collision with an ice edge

The nominal contact area can be found for a penetration δ *;*

$$A = W/2 \cdot H \tag{1.5}$$

The width (*W*) and height (*H*) of the nominal contact area can be determined by the normal penetration depth (δ) along with the normal frame angle (β') and the ice edge angle (ϕ) as shown in Figure 1-4.

$$W = 2\ \delta\ \tan(\phi/2)/\cos(\ \beta') \tag{1.6}$$

$$H = \delta\ /(\sin(\beta')\cos(\beta')) \tag{1.7}$$

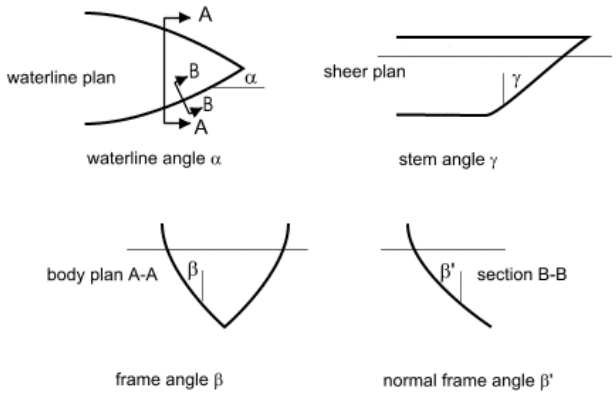

Figure 1-4: Definition of hull angles.

Thus, the area can be stated as;

$$A = \delta^2 \tan(\phi/2)/(\cos^2(\beta')\sin(\beta')) \quad \textbf{(1.8)}$$

The average pressure can be found using the pressure-area relationship;

$$P = Po \cdot A^{ex} \quad \textbf{(1.9)}$$

The normal force is;

$$F_n(\delta) = PA = Po \cdot A^{1+ex} \quad \textbf{(1.10)}$$

Substituting (1.8) into (1.10);

$$F_n(\delta) = Po\,(\delta^2 \tan(\phi/2)/(\cos^2(\beta')\sin(\beta')))^{1+ex} \quad \textbf{(1.11)}$$

$$= Po\, ka^{1+ex}\, \delta^{2+2ex} \quad \textbf{(1.12)}$$

Where, the angle factor ka is;

$$ka = \tan(\phi/2)/(\cos^2(\beta')\sin(\beta')) \quad \textbf{(1.13)}$$

The maximum penetration can be found by substituting (1.12) into (1.4);

$$\frac{1}{2} M_e \cdot V_n^2 = Po \cdot ka^{1+ex} \int_0^{\delta m} \delta^{2+2\cdot ex} \cdot d\delta \quad \textbf{(1.14)}$$

The maximum penetration is;

$$\delta_m = (\tfrac{1}{2}\, M_e\, V_n^2\, (3+2ex)/(Po\; ka^{1+ex}))^{1/(3+2ex)} \quad \textbf{(1.15)}$$

Force can be stated by substituting (1.15) into (1.12);

$$F_n = Po\ ka^{1+ex}\ (\tfrac{1}{2}\ M_e\ V_n^{\,2}\ (3+2ex)/(Po\ ka^{1+ex}))^{(2+2ex)/(3+2ex)} \qquad \textbf{(1.16)}$$

(1.16) can be simplified as;

$$F_n = Po^{\,1/(3+2ex)}\ ka^{(1+ex)/(3+2ex)}\ (\tfrac{1}{2}\ M_e\ V_n^{\,2}\ (3+2ex))^{(2+2ex)/(3+2ex)} \qquad \textbf{(1.17)}$$

Substituting for M_e and V_n,

$$F_n = Po^{\,1/(3+2ex)}\ ka^{(1+ex)/(3+2ex)}\ (l^2/(2\,Co))^{(2+2ex)/(3+2ex)}\ (M_{ship}\ V_{ship}^{\,2}\ (3+2ex))^{(2+2ex)/(3+2ex)} \qquad \textbf{(1.18)}$$

Collecting all shape related terms (comprising ka and the terms with Co and l) into a single term fa gives;

$$fa = (3+2\cdot ex)^{\frac{2+2\cdot ex}{3+2\cdot ex}} \cdot \left(\frac{\tan(\phi/2)}{\sin(\beta')\cdot\cos^2(\beta')}\right)^{\frac{1+ex}{3+2\cdot ex}} \cdot \left(\frac{1}{2\cdot Co}\cdot l^2\right)^{\frac{2+2\cdot ex}{3+2\cdot ex}} \qquad \textbf{(1.19)}$$

The force equation can be stated using the single term fa as below,

$$F_n = fa\cdot Po^{\frac{1}{3+2\cdot ex}}\cdot V_{ship}^{\frac{4+4ex}{3+2\cdot ex}}\cdot M_{ship}^{\frac{2+2\cdot ex}{3+2\cdot ex}} \qquad \textbf{(1.20)}$$

Which for $ex = -0.1$ gives

$$F_n = fa\cdot Po^{0.36}\cdot V_{ship}^{\,1.28}\cdot M_{ship}^{\,0.64} \qquad \textbf{(1.21)}$$

This value of *fa* collects all form related terms (and constants) into a single factor for crushing.

Equation (1.21) represents only the crushing force.

Thus, a comprehensive angle factor, accounting for crushing and flexural failure termed *fa*, is should be included in the defined force as below;

$$fa = lesser\_of\begin{cases}\left(0.097 - .68\cdot\left(\dfrac{x}{L} - .15\right)^2\right)\dfrac{\alpha}{\sqrt{\beta'}} \\ \dfrac{1.2\cdot CF_F}{\sin(\beta')\cdot CF_C\cdot\Delta^{.64}} \qquad \{\text{bow region}\} \\ 0.6 \end{cases} \qquad \textbf{(1.22)}$$

$$= 0.36 \qquad \{\text{other hull regions}\}$$

The next step is to find the ice load patch.

The ice load patch can be found using (1.20) and (1.10).

The nominal contact area is;

$$A = \left(\frac{F_n}{Po}\right)^{\frac{1}{1+ex}} \qquad \textbf{(1.23)}$$

Load patch shape can be changed from triangular to rectangular. It is assumed that the load patch is $H_{nom} \times W_{nom}$, with Area A (see Figure 1-5).

The aspect ratio AR (W_{nom}/H_{nom}) is;

$$\begin{aligned} AR &= 2\tan(\phi/2)\cdot\sin(\beta') \\ &= 7.46\cdot\sin(\beta') \ [\text{assumes } \phi = 150 \text{ deg.}] \end{aligned} \qquad \textbf{(1.24)}$$

Thus, the area is;

$$A = H_{nom}\cdot H_{nom}AR \qquad \textbf{(1.25)}$$

By using the nominal contact area, it can be written;

$$H_{nom} = \left(\frac{F_n}{Po \cdot AR^{1+ex}} \right)^{\frac{1}{2+2ex}} \quad \textbf{(1.26)}$$

$$W_{nom} = \left(\frac{F_n}{Po \cdot AR^{1+ex}} \right)^{\frac{1}{2+2ex}} \cdot AR \quad \textbf{(1.27)}$$

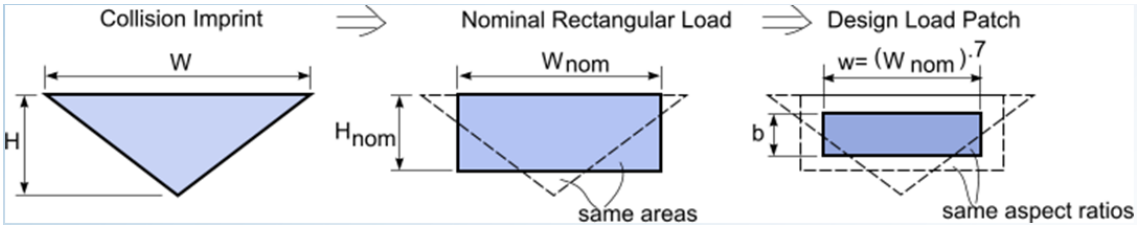

Figure 1-5: Load patch shape from triangular to rectangular

The next step is to reduce the load patch size (force is unchanged, so design pressure rises correspondingly) which is conservative and is done to account for the typical concentration of force that takes place as ice edges spall off (see Figure 1-6)

The rule patch length *w* can be stated as;

$$w = W_{nom}^{\ wex} = Fn^{wex/(2+2ex)} \cdot Po^{-wex/(2+2ex)} \cdot Ar^{wex/2} \quad \textbf{(1.28)}$$

Where, with $wex = 0.7$ and $ex = -0.1$;

$$w = Fn^{0.389} \cdot Po^{-0.389} \cdot Ar^{0.35} \quad \textbf{(1.29)}$$

The design load height is;

$$b = \frac{w}{AR} \quad \textbf{(1.30)}$$

Or

$$b = Fn^{0.389} \cdot Po^{-0.389} \cdot AR^{-0.65} \quad \textbf{(1.31)}$$

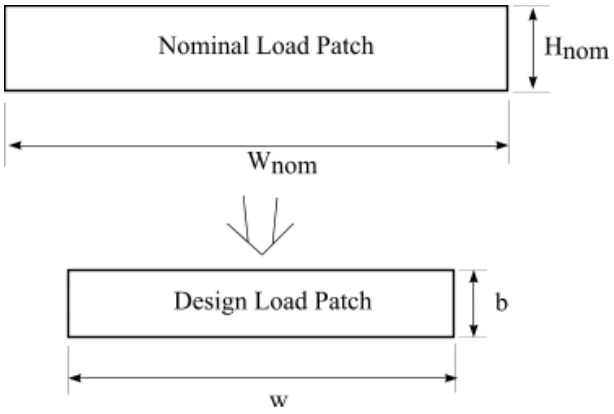

Figure 1-6: Nominal and design rectangular load patches

The nominal and design load patches have the same aspect ratio. The load quantities used in the scantling calculations include the line load;

$$Q = F_n / w \tag{1.32}$$

and the pressure,

$$p = Q/b \tag{1.33}$$

Q and p can be found by using (1.20) and equations above;

The line load;

$$Q = \frac{F_n^{1-\frac{wex}{2+2ex}} \cdot Po^{\frac{wex}{2+2ex}}}{AR^{wex/2}} \tag{1.34}$$

The pressure is;

$$p = \frac{F_n^{1-\frac{wex}{1+ex}} \cdot Po^{\frac{wex}{1+ex}}}{AR^{wex-1}} \tag{1.35}$$

Where $wex = 0.7$ and $ex = -0.1$.

The line load and pressure are;

$$Q = F_n^{0.611}\, Po^{.389}\, AR^{-0.35} \tag{1.36}$$

And

$$p = F_n^{0.222}\, Po^{.778}\, AR^{0.3} \tag{1.37}$$

Respectively.

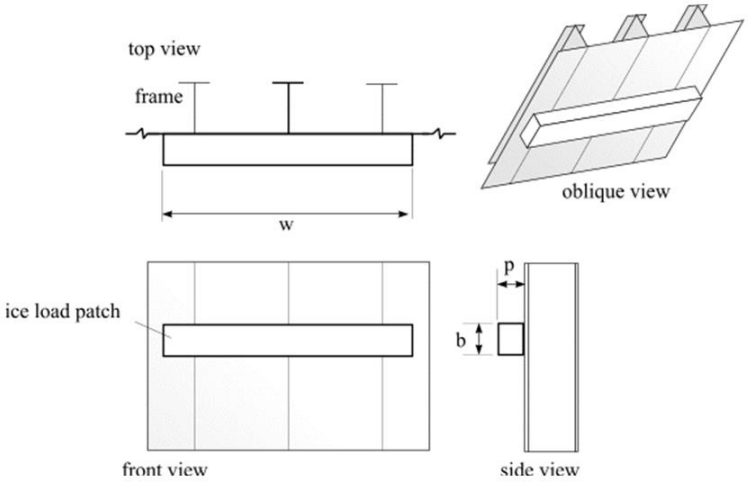

Figure 1-7: Ice load patch configuration

Peak pressure factors (PPF) in design formulae is used to consider that ice loads are quite peaked within the load patch. Figure 1-8 describes the effect of peak pressure factors is that smaller structural elements experience larger design pressures.

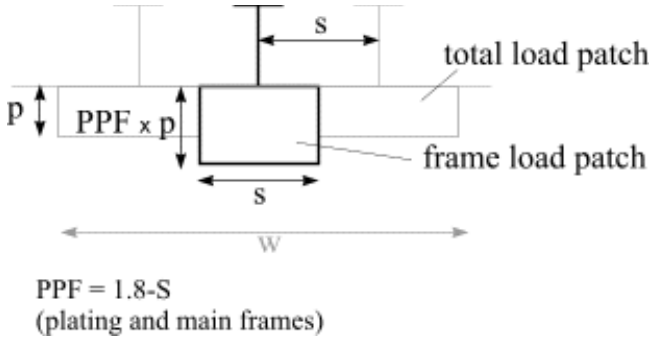

Figure 1-8: Peak Pressure Factor used to design individual elements.

1.4 Ice-Structure Interaction

Figure 1-9 illustrates various ice failure mechanisms during ice-structure interaction. There is a direct contact zone where the area is consistently changed by flaking of the ice edge and internal cracks. When the crushed ice rubble enters into trapped between the ice and the structure, the rubble can then cause high pressure. On the other hand, relatively low pressure will occur at the edge. Thus, high and low pressures occur within the contact region.

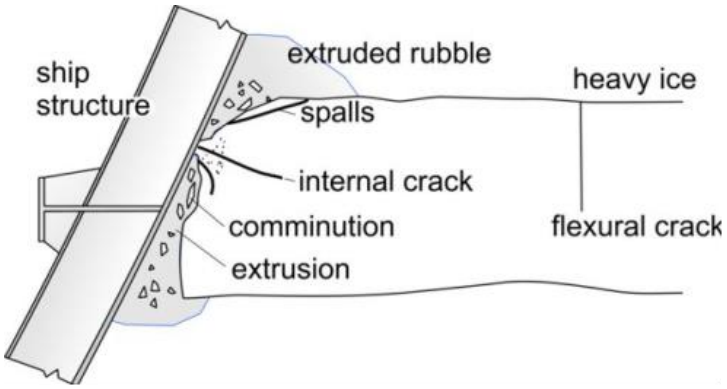

Figure 1-9: Sketch of ice contact with a ship structure (Daley, 2004)

Nominal, true and measured pressure measurements are illustrated in Figure 1-10. The first, 'nominal pressure', if there is an independently measured total force and overlap area (nominal area) of the area and structure, dividing one by the other will give the nominal pressure. This method is quite simple and easy method; however, gives no information on the local pressure distribution which would be much higher or lower than the nominal pressure. To observe the 'true pressure', it would be necessary to measure pressure contiguously over the entire surface with high spatial resolution. However, this type of data is not practically existent. The last sketch describes measured pressure which

has been measured on a rather coarse array, and may be subject to noise and other forms of error.

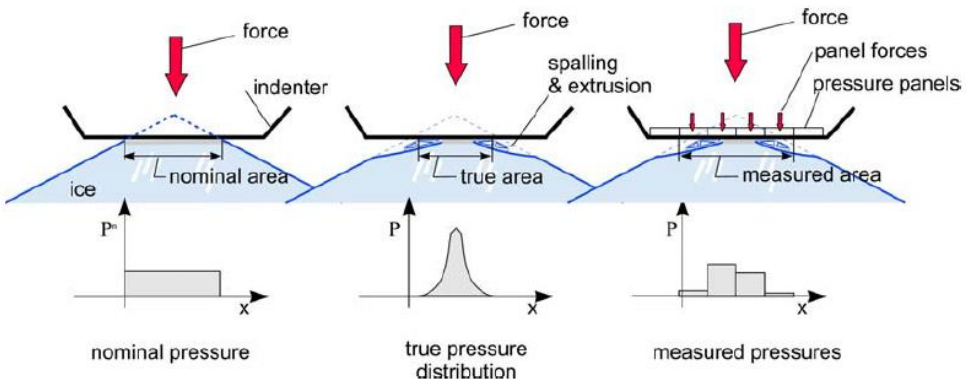

Figure 1-10: Types areas and pressures related to pressure-area data (Daley, 2004)

The spatial pressure-area distribution describes the distribution of pressure within contact area at an instant in time. The highest pressure occurs on a small area at the peak. The average pressure within larger areas will necessarily be smaller than the peak pressure. Thus, an inverse relationship between pressure and area is always shown in spatial pressure-area plots (see Figure 1-11).

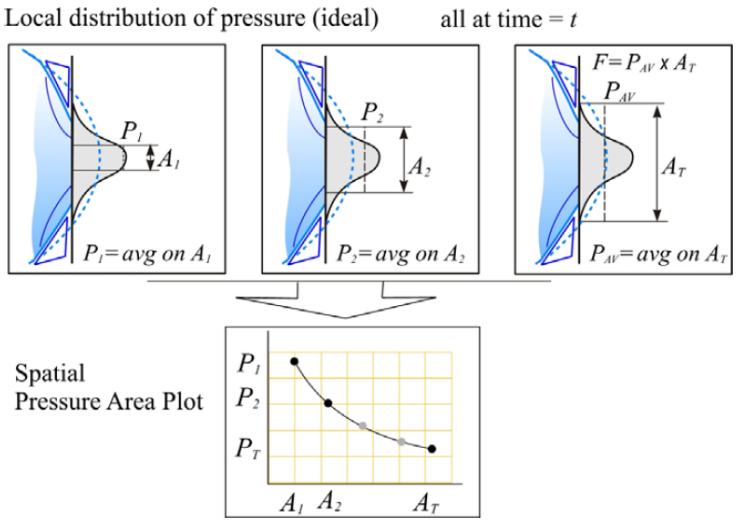

Figure 1-11: Sketch of ice pressure and the meaning of a spatial pressure-area plot (Daley, 2004)

In the process pressure-area distribution, the force and the area are determined during the whole interaction process and then the data can be used to obtain the change in pressure and area during ice loading event (see Figure 1-12).

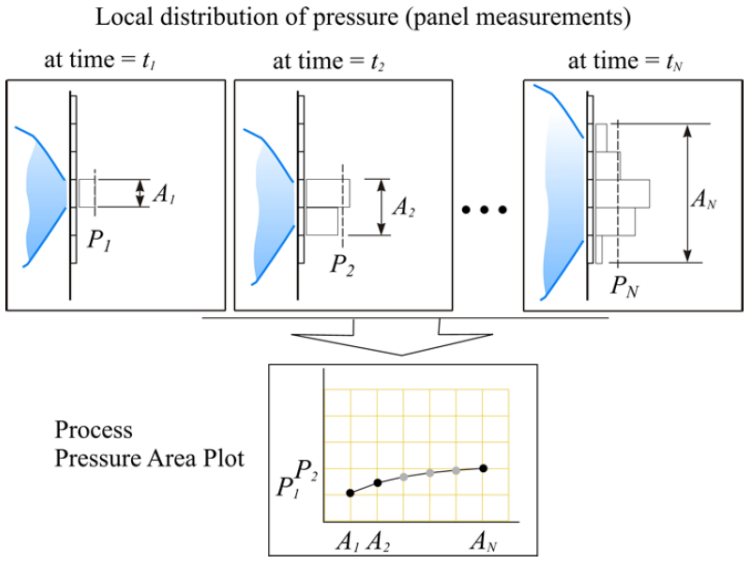

Figure 1-12: Sketch of measured ice pressure data and process pressure-area plots (Daley, 2004)

1.5 Framing Design Cases and Mechanisms

The framing design case and mechanics formulations were derived by Kendrick and Daley (2000) and repeated here. This procedure is later used to calculate the framing design of the grillage when checking for compliance with the IACS Polar Rules.

1.5.1 Assumptions

Some assumptions have been used in the framing design. It is assumed that frame members have uniform cross-sections along their length. All structures were considered that has the same material properties, e.g. yield strength is identical for plating and framing. It is also assumed that the position of the plastic neutral axis of a frame cannot move inside the attached plate, although the equal area axis (nominally the same thing) will frequently be within the plate.

1.5.2 Bending and Shear Interaction

The current new UR uses bending and shear interaction more rigorously than any existing rules or standards, considering actual section shape. The interaction can be described by equation (1.38), where M_o is section-dependent, greater than or equal to zero.

$$\left(\frac{M - M_o}{M_p - M_o}\right)^2 + \left(\frac{T}{T_{ult}}\right)^2 = 1 \qquad \textbf{(1.38)}$$

Bending moment (M) and Shear (T) have actual and ultimate values as shown in Figure 1-13. Reviewing the curve that can be used to represent this equation, it can be seen that at full shear any section with $M_o > 0$ will have some reserve bending moment capacity.

The full plastic section modulus Z_p is defined as the sum of contributions from the web Z_w and flange Z_f;

$$Z_p = Z_f + Z_w \qquad \textbf{(1.39)}$$

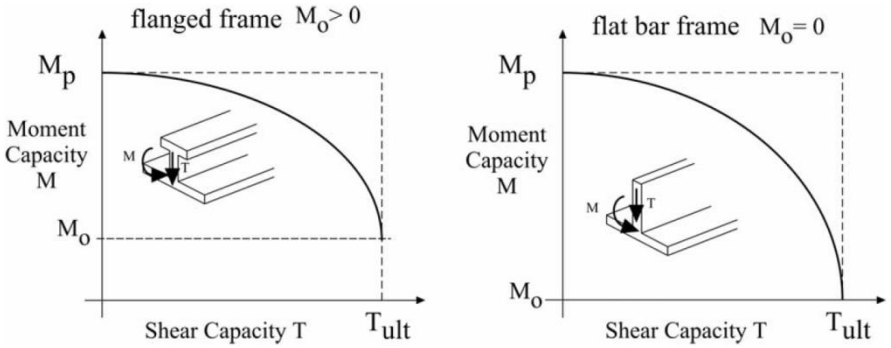

Figure 1-13: Bending/shear interaction diagrams

For any value of shear, there is a minimum web area A_o, that can just carry T. The actual web area A_w must be greater or equal to A_o. As shear increases, the bending contribution of the web is reduced, until at the maximum shear (T_{ult}) the contribution of the web is zero (as it is fully yielded in shear). Thus the moment M lies within the range M_o to M_p. Moments and shear forces are related to section properties with the usual relationships;

$$M_p = Z_p\,\sigma_{yield},\ M_o = Z_f\,\sigma_{yield},\ M = Z_{pr}\,\sigma_{yield}\ ,\ T = A_o\,\tau_{yield}\ ,\quad T_{ult} = A_w\,\tau_{yield} \qquad \textbf{(1.40)}$$

The 'reduced' modulus Z_{pr} will lie somewhere between the full and minimum values, depending on the level of shear;

$$Z_{pr} = Z_f + Z_w[1-(A_o/A_w)^2]^{0.5} \qquad \textbf{(1.41)}$$

Equation (1.41) is used for hinges that contain significant shear.

1.5.3 Limits States

The three primary limit states considered in the URs are illustrated in Figure 1-14. All three result in the formation of a collapse mechanism.

(a) shows a 3-hinge mechanism that will form under a centered load.

(b) shows an asymmetric shear collapse mechanism under an edge load.

Finally, 4(c) shows a web collapse under a central load.

Each of these mechanisms can be solved with energy methods (limit equilibrium). The dominant mechanism for any case has the lowest load capacity and this depends on section shape, load length and load intensity.

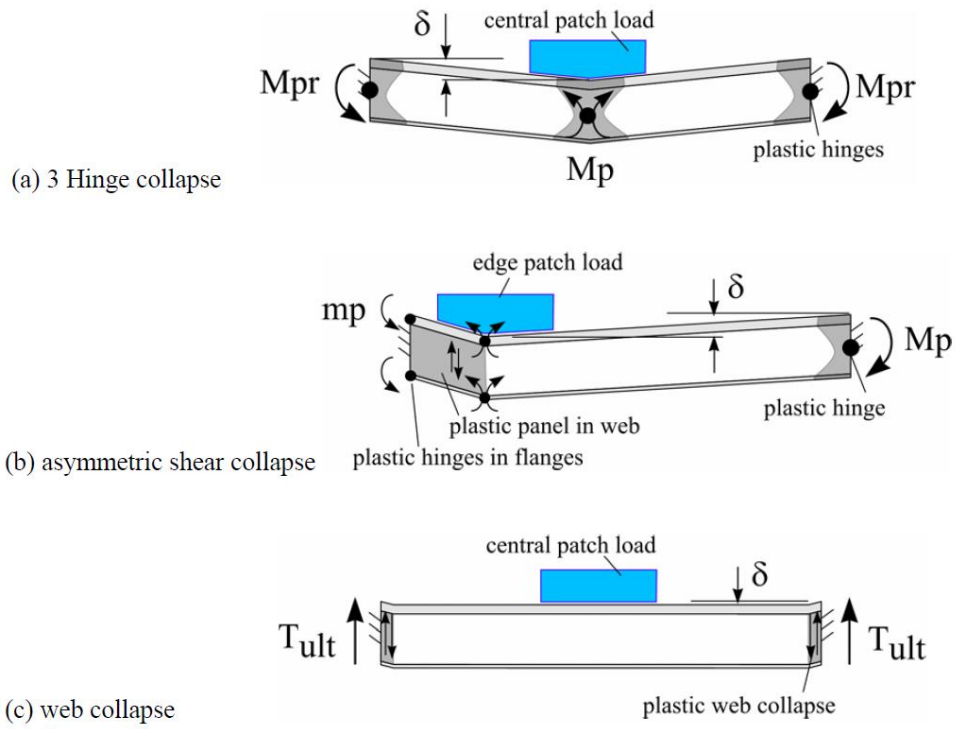

Figure 1-14: The 3 limit states considered for frames

1.5.4 Limit State Equations

1.5.4.1 Symmetric Loading Case

The full derivation of the UR formulae is provided by reference Kendrick and Daley (2000). All of the rule formulae are derived by equating internal and external work.

For the web collapse, the energy equation is;

$$P \cdot b \cdot S = 2 \cdot A \cdot \frac{\sigma_y}{\sqrt{3}} \qquad \textbf{(1.42)}$$

The minimum web area Ao required to carry the load in pure shear is;

$$Ao = \frac{1}{2} P \cdot b \cdot S \cdot \frac{\sqrt{3}}{\sigma_y} \qquad \textbf{(1.43)}$$

For the 3-hinge collapse case,

The energy balance equation for external and internal work is;

$$(P \cdot b \cdot S)\left(1 - \frac{b}{2 \cdot L}\right) = 4 \cdot \frac{\sigma_y}{L} \cdot \left(Zp + \frac{j}{2} \cdot Zpr\right) \qquad \textbf{(1.44)}$$

Where, the full plastic section modulus, *Zp*

The reduced section modulus, *Zpr*

the section shape dependency effect, kw

$$Zp = Af \cdot \left(\frac{tf}{2} + hw + \frac{tp}{2}\right) + Aw \cdot \left(\frac{hw}{2} + \frac{tp}{2}\right) \qquad \textbf{(1.45)}$$

$$Zpr = Zp \cdot \left[1 - kw \cdot \left[1 - \sqrt{1 - \left(\frac{Ao}{Aw}\right)^2}\right]\right] \qquad \textbf{(1.46)}$$

$$kw = \frac{1}{1 + 2 \cdot \frac{Af}{Aw}}$$

Where, **(1.47)**

Equation (1.44) can be re-arranged to give the capacity for 3-hinge collapse;

$$P = \frac{\left[j + 2 - kw \cdot j + kw \cdot j \cdot \sqrt{1 + 3 \cdot (j+2) \cdot Zpns \cdot (-j + 2kw \cdot j - 2)} \right]}{6 \cdot Zpns \cdot kw^2 \cdot j^2 + 2} \cdot \sigma_y \cdot Zp \cdot \frac{4}{(L \cdot S \cdot L) \cdot \left(1 - \frac{b}{2 \cdot L}\right)} \quad \textbf{(1.48)}$$

$$Zpns = \left[\frac{Zp}{Aw \cdot L \cdot \left(1 - \frac{b}{2 \cdot L}\right)} \right]^2$$

Where, **(1.49)**

Equation (1.48) can be used directly in comparisons with finite element model results or experiments. Equation (1.48) shows a frame capacity that is just below the 'knuckle' in the response curve over a wide range of frame configurations. This equates to plastic strains of fractions of a percent and to very small residual deflections. These are all desired characteristics for the design point, and thus this capacity equation is considered to offer a valid basis for the required UR formulations.

The rule requirement for section modulus is also found from equations (1.45), (1.46), and (1.47);

$$Zp = \frac{P \cdot b \cdot S \cdot L}{4 \cdot \sigma_y} \cdot \left(1 - \frac{b}{2 \cdot L}\right) \cdot \frac{1}{2 + kw \cdot \left[\sqrt{1 - \left(\frac{Ao}{Aw} \right)^2} - 1 \right]} \quad \textbf{(1.50)}$$

Equation (1.50) shows that the required section modulus and shear area are interdependent, as would be expected from the discussion above. This approach is more rigorous and consistent with actual structural behaviour than those of any current system.

1.5.4.2 Asymmetric Loading case

For the asymmetric shear collapse case,

The energy balance equation is:

$$(P \cdot b \cdot S)\left(1-\frac{b}{2 \cdot L}\right)=\sigma_y \cdot\left[\frac{Aw}{\sqrt{3}}+\frac{Zp}{L} \cdot fz\right] \qquad \textbf{(1.51)}$$

Where, *fz* can be approximated as:

$$fz = 1.1+5.75 \cdot kz^{.7} \qquad \textbf{(1.52)}$$

and *kz* is the ratio of the combined flange moduli to the total section modulus:

$$kz=\frac{zp}{Zp} \qquad \textbf{(1.53)}$$

Equation (1.51) can be re-arranged to give the capacity for asymmetric shear collapse;

$$P_{asym}=\frac{\sigma_y}{b \cdot S\left(1-\frac{b}{2 \cdot L}\right)} \cdot\left[\frac{Aw}{\sqrt{3}}+\frac{Zp}{L} \cdot (1.1+5.75 \cdot kz^{.7})\right] \qquad \textbf{(1.54)}$$

The rule requirement for section modulus is also found from equation (1.51);

$$Zp=\frac{P \cdot b \cdot S}{\sigma_y \cdot (1.1+5.75 \cdot kw^{7})} \cdot\left(1-\frac{b}{2 \cdot L}\right) \cdot L \cdot\left[1-\frac{Aw}{2 \cdot Ao \cdot\left(1-\frac{b}{2 \cdot L}\right)}\right] \qquad \textbf{(1.55)}$$

Where, Ao is given in (1.43).

Equations (1.55) and (1.50) govern the asymmetrical and symmetrical load capacities respectively. Both show that shear area and section modulus are interdependent, and require iteration to yield an optimal design. A satisfactory frame must satisfy equations (1.43), (1.50), and (1.55). The derivations presented above are provided in more detail in Kendrick and Daley (2000).

1.6 Previous Physical Grillage Experiments

Significant research efforts have been carried out to investigate the plastic behavior of grillage structures. However, most cases used a steel plate or rigid indenter rather than real ice. The tests therefore showed certain structural response behavior that may occur differently if subjected to ice loads.

One of the largest scale physical experiments was conducted by Bond and Kennedy (1998). The authors used simple icebreaking ship structures (panels) to investigate the post-yield region. The large-scale panels used in the test were representative of a mid-body hull structure along the ice belt of a Canadian Arctic Class vessel. The test was able to capture the post-yield stability behavior of typical icebreaker hull panels from load deformation characteristics and progression of failure from plastic hinge formation and tripping of the framing system to rupture of the plating. A FE model was developed and validated with the experiment results. The research found that the non-linear finite element analyses can be confidently used to explore the post-yield strength and stability response of icebreaking ship structure. However, the experiments were loaded using three 500-ton jacks and two 200-ton jacks with rigid indenters rather than real ice.

Daley and Hermanski conducted an experimental study in order to validate the limit state equation in the IACS Polar Rules (Daley & Hermanski, 2008a; 2008b). Eight single frames and two large grillage tests were performed to investigate frames subject to intense local loads such as ice loads. A rigid steel indenter (102 x 102 mm) was used to load a structural grillage up to 1,470 kN causing punching shear in the 10 mm shell plate. The research found that the large grillage tests typically required much higher load levels

than a single frame tests and both the initial and post yield capacity for the grillage is considerably higher than that for the single frame.

Also a number of researchers have developed and explored simulation models based on these tests to represent notable results. Abraham (2009) developed a regression equation using DOE (Design of Experiment) techniques for predicting capacity of frames with different stiffener forms. The capacity of a large grillage is more than the single frame in most cases up to about 35 %. Quinton (2009) studied effect of moving ice loads on the plastic capacity of a ship's structure. The research found that the structures capacity to withstand moving loads causing progressive damage was generally less than its capacity to withstand static loads.

However, while the results of previous experiments and simulations well present post-yield behavior of the grillage with rigid indenter, there was no insight in terms of the interaction between ice and ship structures.

In this study, ice specimens were produced in the laboratory and those ice specimens were used for the grillage tests. This allowed for investigation into structural deformation considering the failure of ice.

1.7 Non-linear Finite Element Method

In linear simulation, the displacements $\{D\}$ are proportional to the loads $\{F\}$ and the stiffness $[K]$ of the structure is independent on the value of the load level shown in Equation (1.56). It is applicable only if the deformation is not significant, stresses remain below the material yield strength, no boundary conditions change and the stress-strain is linear which are described by Hook's law. It implies that the principle of superposition is applicable and the solution is independent of loading history (see Figure 1-15).

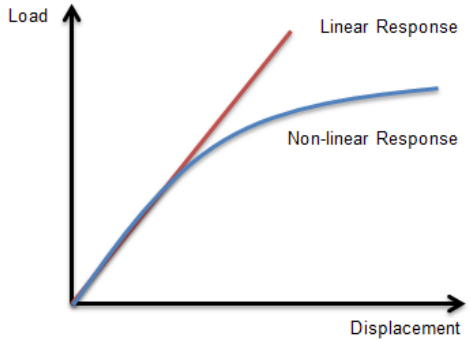

Figure 1-15: Difference between linear and non-linear response

$$[K]\{D\} = \{F\} \qquad \textbf{(1.56)}$$

Where, $\{F\}$: Nodal force

$\{D\}$: Nodal displacement

$[K]$: Stiffness matrix

On the other hand, the nonlinear behavior occurs as both the structural stiffness matrix $[K]$ and the load vector $\{R\}$ become functions of the displacement $\{D\}$ shown in Equation (1.57). It implies that the principle of superposition is not applicable and the solution may depend on loading history.

$$[K]\{D\}=\{R\} \qquad \textbf{(1.57)}$$

Thus, it is unable to solve the equation because the stiffness and the load is not known.

Structural nonlinearities can be specified as geometric, material and boundary nonlinearities. Geometric nonlinearity is due to large deformation of structures. When the deformation of structure is significant, the stiffness matrix will be changed. When the stress-strain relation is not linear and not following Hooke's law, material nonlinearity is shown. Material nonlinearity is associated with changes in material properties such as plasticity. When displacement boundary conditions depend on the deformation, boundary nonlinearity is to be considered. The most significant application of boundary nonlinearity is the contact problem.

1.7.1 Solutions for Nonlinearities

When stiffness matrix is not constant, the displacement cannot be obtained by a linear equation. Therefore, an iterative numerical scheme in divided load steps is applied to solve the non-linear problem. The solution can be obtained by finding equilibrium between stiffness and external force for each divided load step. Some numerical methods performing the numerical iteration are explained as below.

In the Newton-Raphson method, the tangential stiffness matrix is formed and decomposed at each iteration. If the residual force is smaller than a criterion, then the sub-step will be converged but if not, equilibrium iteration is initiated. The iterations will be repeated until the convergence criterion is satisfied. Therefore, it takes quite a long time for a large model to converge because the tangential stiffness is formed and decomposed at each iteration (see Figure 1-16).

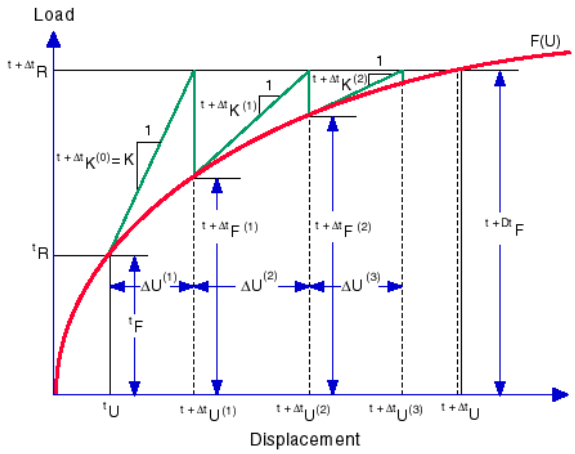

Figure 1-16: Newton-Raphson method (SolidWorks)

In contrast to the Newton-Raphson method, the tangential stiffness matrix is formed and decomposed at the beginning of each step and used throughout the iterations in the Modified Newton-Raphson method (see Figure 1-17).

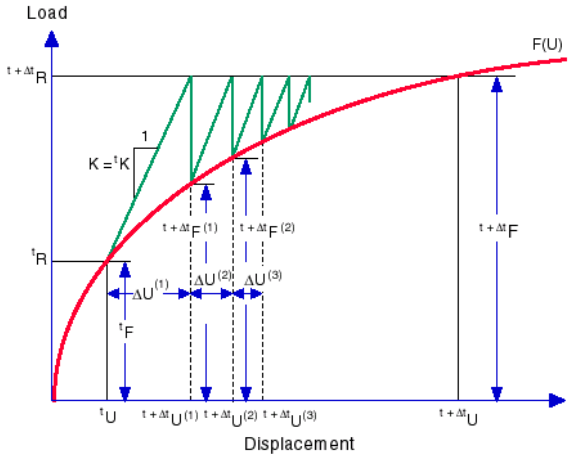

Figure 1-17: Modified Newton-Raphson method (SolidWorks)

The arc-length method is applicable for the tracing of a complex path in the load-displacement response into the buckling/post buckling regimes through controlling displacement and load increments simultaneously. The arc length method is used for the so called ‘snap-back’ problem as shown in Figure 1-18.

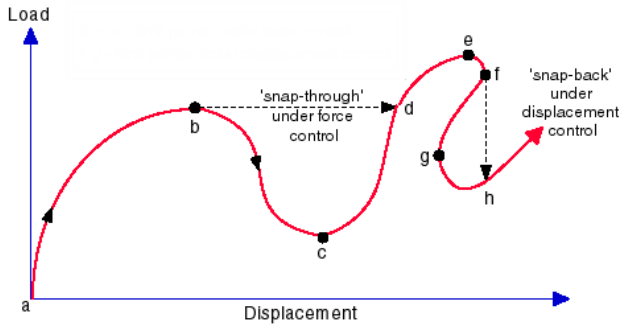

Figure 1-18: Application example of the arc length method (SolidWorks)

1.7.2 Hardening Rules

There are two typical hardening rules to prescribe the strain hardening. Kozarski (2005) well describes the importance of strain hardening in plastic response. In this study, the isotropic hardening was used to consider large deformation.

When a stress continues to push a yield surface, the yield surface will expand its size with the same axis of the yield surface. It means that magnitude of the tensile yield strength and the compressive yield strength are same. Isotropic hardening is often used for large strain but is not applicable for cyclic loading cases. The yield surface expands uniformly in all directions with plastic flow (see Figure 1-19).

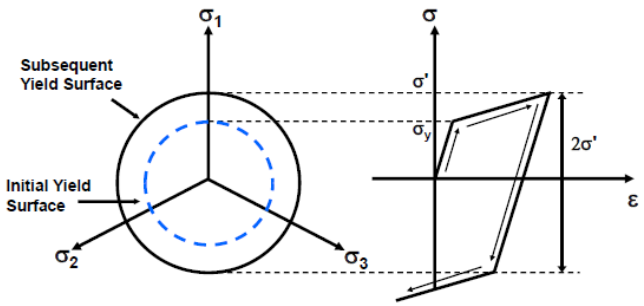

Figure 1-19: Stress-strain behavior for isotropic hardening (ANSYS)

When a stress continues to push a yield surface, the yield surface will change its location with same size of the yield surface. The difference between the tensile yield strength and the compressive yield strength is constant as $2\sigma_Y$. The yield surface remains constant in size and translates in the direction of yielding. Kinematic hardening is generally used for small strain and cyclic loading applications (see Figure 1-20).

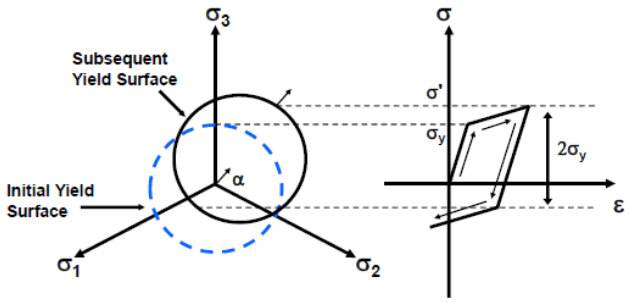

Figure 1-20: Stress-strain behavior for linear kinematic hardening (ANSYS)

2 LARGE GRILLAGE EXPERIMENTS

2.1 Introduction

Previous experiments designed and carried out by Daley and Hermanski (2008a; 2008b) used a rigid steel indenter to load a structural grillage into the plastic regime. In the current experiments, the same test apparatus (red grillage support frame) and grillage design were adopted; however, ice samples were used to load the structure rather than rigid indenters. This allowed for investigation into structural deformation considering the failure of ice. Two large grillages were prepared and tested. The first grillage tests were intended to study the ultimate load-carrying capacity when subjected to central and symmetric loading. The second grillage was tested to study the influence of variable ice loading positions along a single frame.

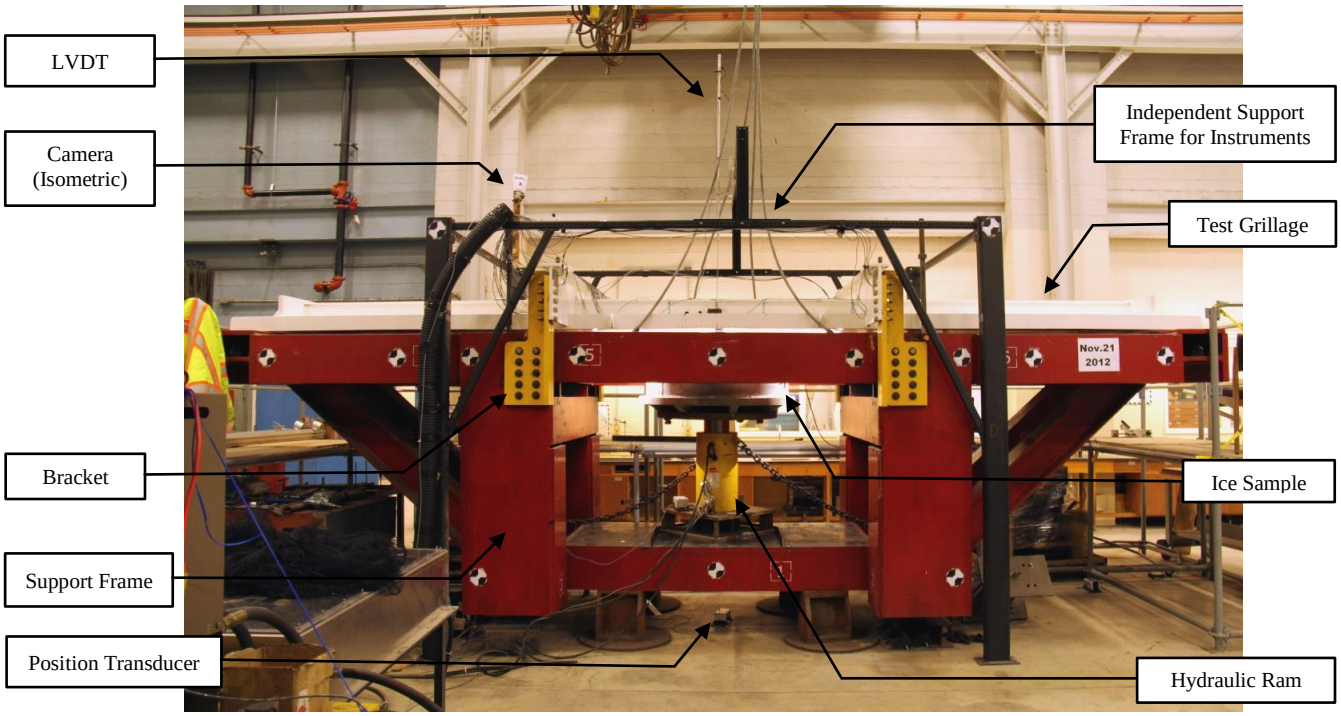

Figure 2-1: Grillage test apparatus

This section describes the experimental preparation and procedures. The test apparatus, shown in Figure 2-1, mainly consists of the grillage support frame (red), 700,000 lbs-capacity and 450 mm stroke length hydraulic ram (yellow), the test grillage (white) and the support frame for instruments (black).

2.2 Geometry

The structure of a ship's hull typically consists of shell plating with attached stiffeners and supporting frames. The combination of the plating and the stiffeners is a stiffened panel. The stiffened panel with the supporting frames (e.g. web frames and/or stringers) compose a large grillage. Stiffeners in a grillage can be arranged longitudinally or transversely, which are termed longitudinal and transverse frames, respectively.

The geometry of the large grillage (in fact, two identical grillages named #1 and #2) is shown in Figure 2-2. The scantlings are a full-scale representation of a transversely framed 10,000 ton Ice Class PC 6 midbody ice belt arrangement. The grillage consists of a plate (6.756 m long and 1.460 m wide), three continuous stiffeners (200 x 8 / 75 x 10), two supporting stringers (325 x 18 / 120 x 18) and two heavy side bars (100 x 30). The stringer's spacing is 2 m and the stiffener's spacing is 350 mm. The stiffeners run through the stringers and their web plates are attached on a single side to the stringer.

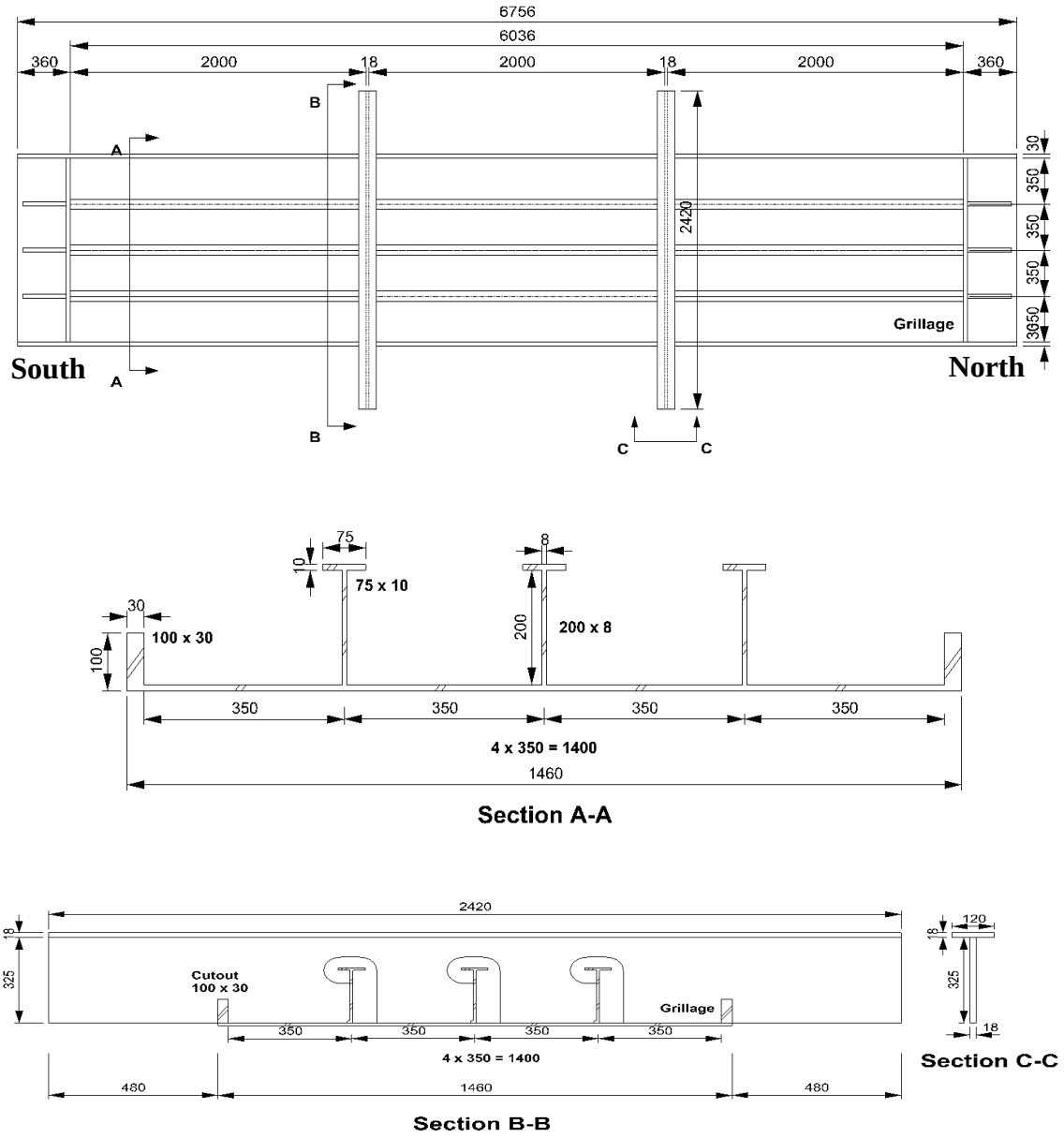

Figure 2-2: Geometry of the large grillage

2.3 Test Preparation

This section describes each element of preparation for the tests. These elements, highlighted in Figure 2-3, include ice specimen preparation, marking the grillages, setting instrumentations and data acquisition system, recording and display systems and handling and positioning ice samples prior to the tests.

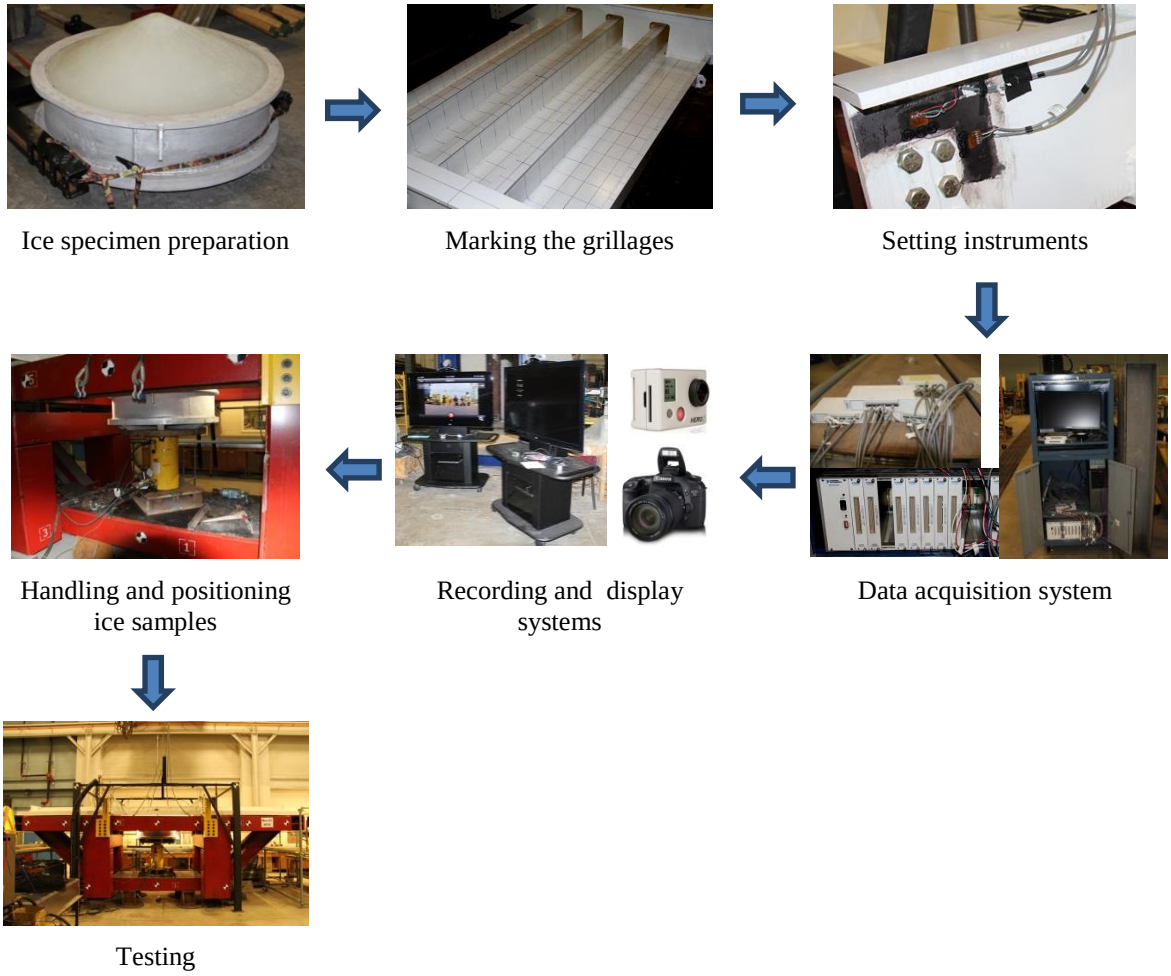

Figure 2-3: Test preparation

2.3.1 Ice Specimen Preparation

Reddy (2012) describes a detailed process of preparing ice samples for laboratory experiments. There are two different procedures of producing ice samples depending on the size. Small ice samples (259 mm in diameter) are made of deionized, degassed and purified freshwater mixed with ice chips to control grain size and crystal structure. They are typically used for small scale laboratory indentation tests (Bruneau et al., 2013) at various temperatures (cold room test) and in small scale impact tests (Clarke, 2012) carried out in a double pendulum apparatus. Large ice samples (1 m diameter), used for larger scale tests, such as these grillage tests and large double pendulum impact tests (Alam et al., 2012) are produced in the laboratory from tap water and ice chips in an aluminum ice holder. It takes three to four days to completely freeze a large ice sample in a cold room at about -10 ℃. When an ice sample is ready (see Figure 2-4), shaping the sample is conducted according to the designed degree using a shaping device (see Figure 2-5). In this study all ice samples were shaped to 30 degree ice cones. This provides a typical ice impact that starts with a small contact area and increases with penetration. Thus, the radius and cone height of ice samples are 500 mm and 289 mm, respectively (see Table 2-1).

Table 2-1: Ice sample parameters

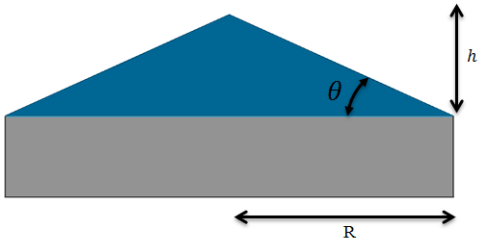

Item	Units	Value
radius, R	mm	500
cone angle, θ	degree	30
cone height, h	mm	289
temperature, T	℃	-10

Figure 2-4: Ice sample ready for shaping

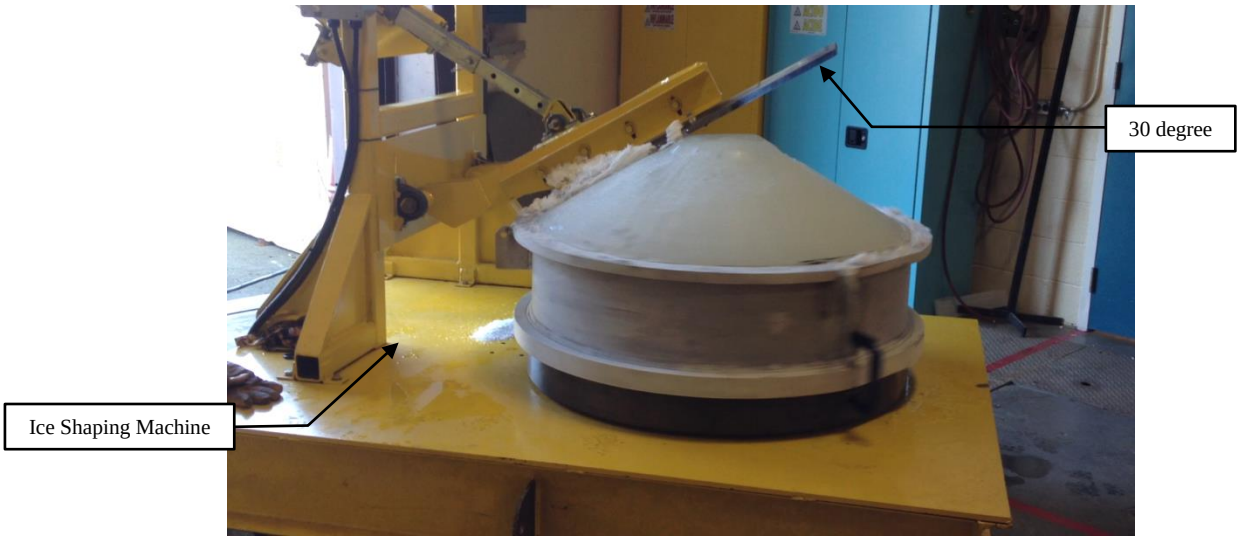

Figure 2-5: Shaping the ice sample

2.3.2 Marking the Grillages

The grillages were marked with lines in the longitudinal and transverse directions in order to provide guidance for the installation of instruments and measurements of deformation (using the MicroScribe®) during and after the experiments. Without these marking lines, it would be impossible to obtain an accurate shape of deformation.

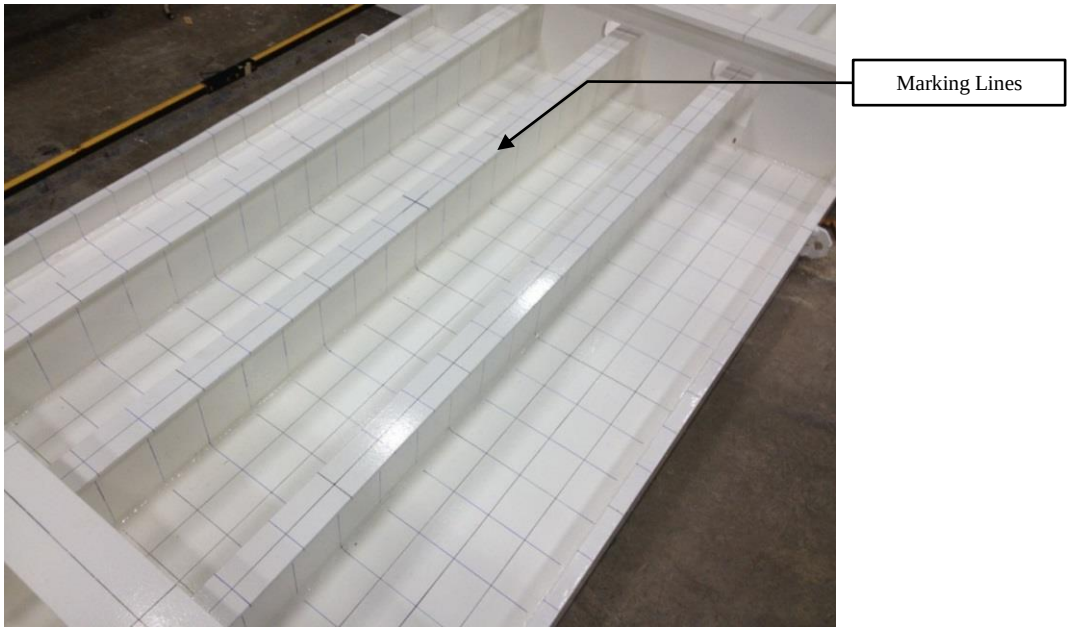

Figure 2-6: Marking lines on the grillage

2.3.3 Data Acquisition System

Strain gauges, a linear variable differential transformer (LVDT) and position transducers ('yo-yo' pots) were used to measure strains, deflections on the grillage and the grillage support frame during tests. Force was measured from a pressure transducer connected to the hydraulic ram. Data from the strain gauges, LVDT, pressure and position transducers were captured by National Instruments LabView™ software with multiple channels as shown in Figure 2-8.

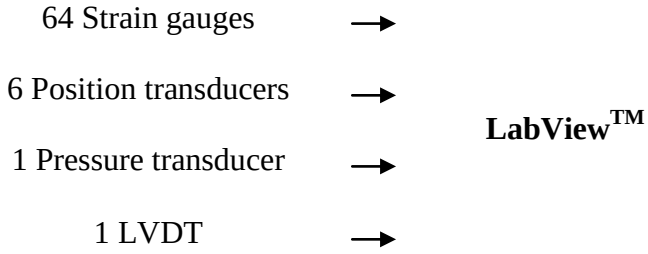

Figure 2-7: Data acquisition system

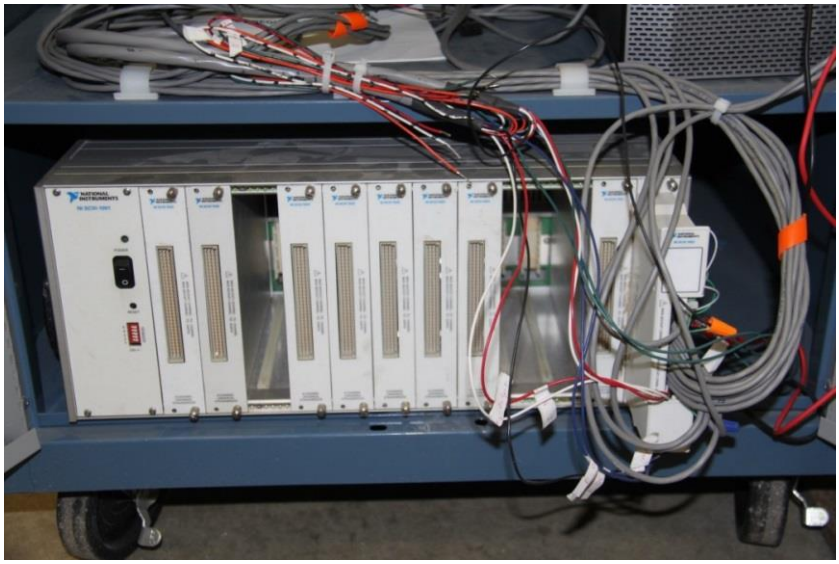

Figure 2-8: National Instruments® data acquisition devices

2.3.4 Strain Gauges and LVDT

In total, 64 strain gauges were mounted on the grillage in order to measure strains of the grillage during tests. Figure 2-9 shows the arrangement of the strain gauges. One LVDT was located above the loading position to measure the vertical deflection of the grillage. The LVDT was mounted on a separate supporting frame which stands on the laboratory floor in order to maintain position during loadings without the influence of the grillage deformation (see Figure 2-11).

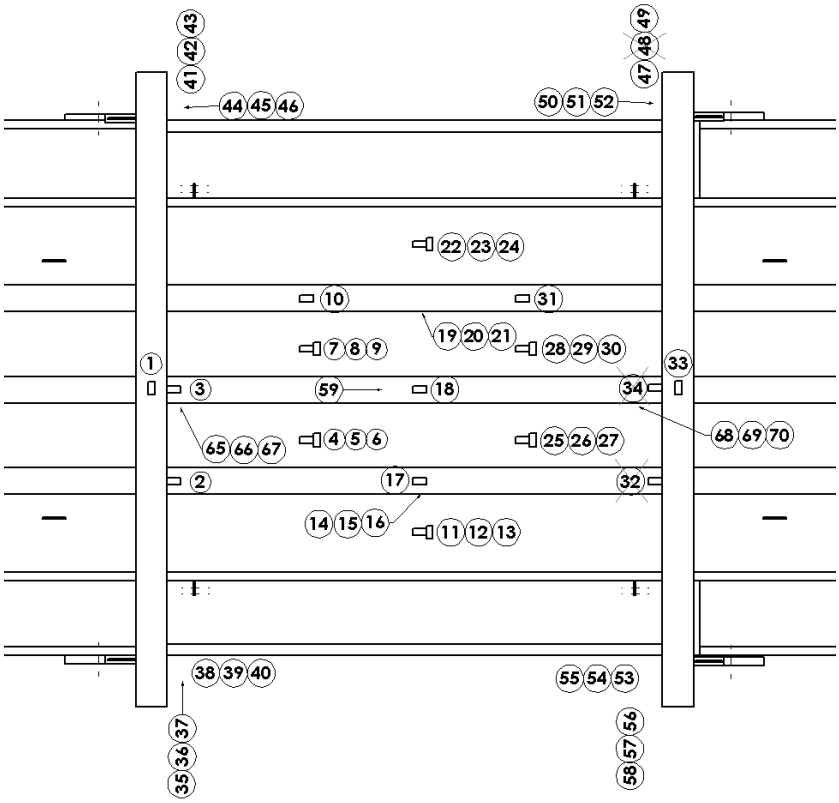

Figure 2-9: Arrangement of strain gauges and LVDT

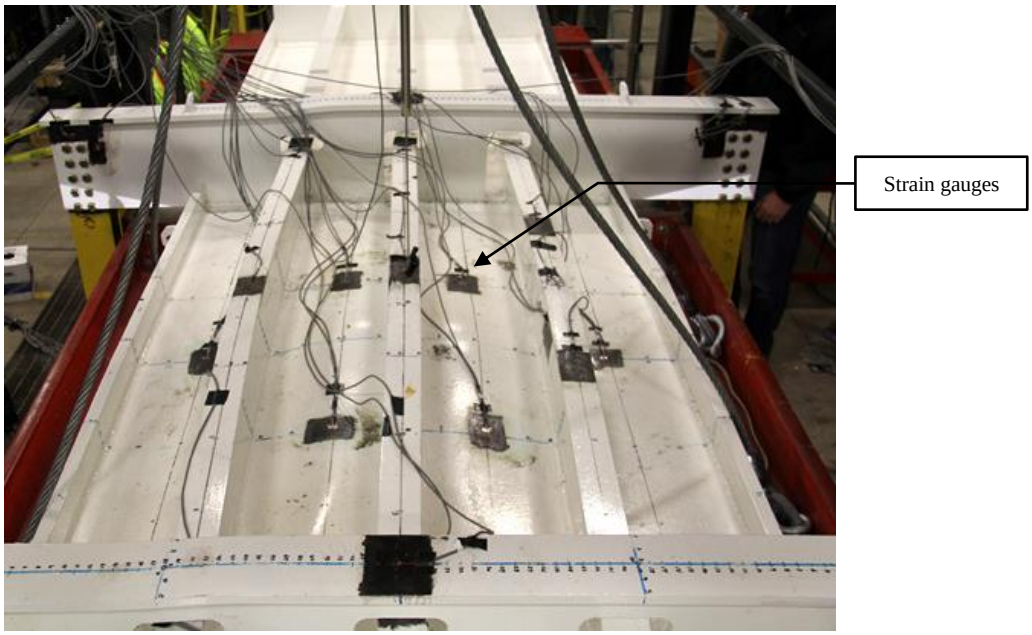

Figure 2-10: Strain gauges on the grillage

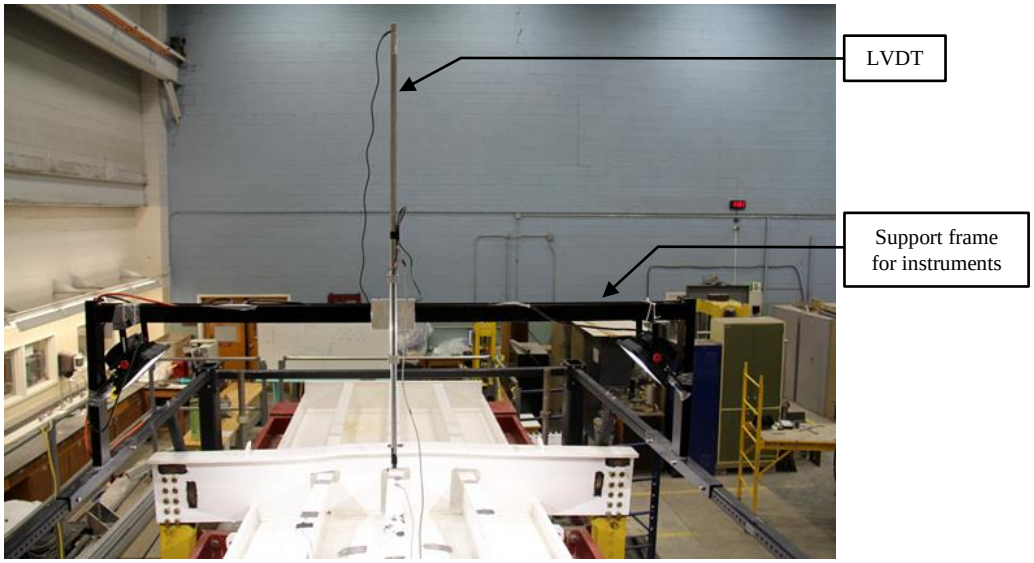

Figure 2-11: LVDT mounted on the instrument frame

2.3.5 Position Transducers ('yo-yo' pots) and Pressure Transducer

Figure 2-12 illustrates the arrangement of position transducers. Five position transducers were used to measure the deformation of the grillage support frame. Although the grillage support frame was designed as rigid as possible, the large deformation of the grillage may cause some elastic or plastic deformation of the supporting frame during the tests. Thus, the vertical deformation of the grillage support frame needs to be considered.

Table 2-2: Description of the position transducers

No.	Measurement
60, 61, 62, 94	Deformation of the grillage support frame
63	Deformation of the base of the grillage support frame
64	Hydraulic ram's extension

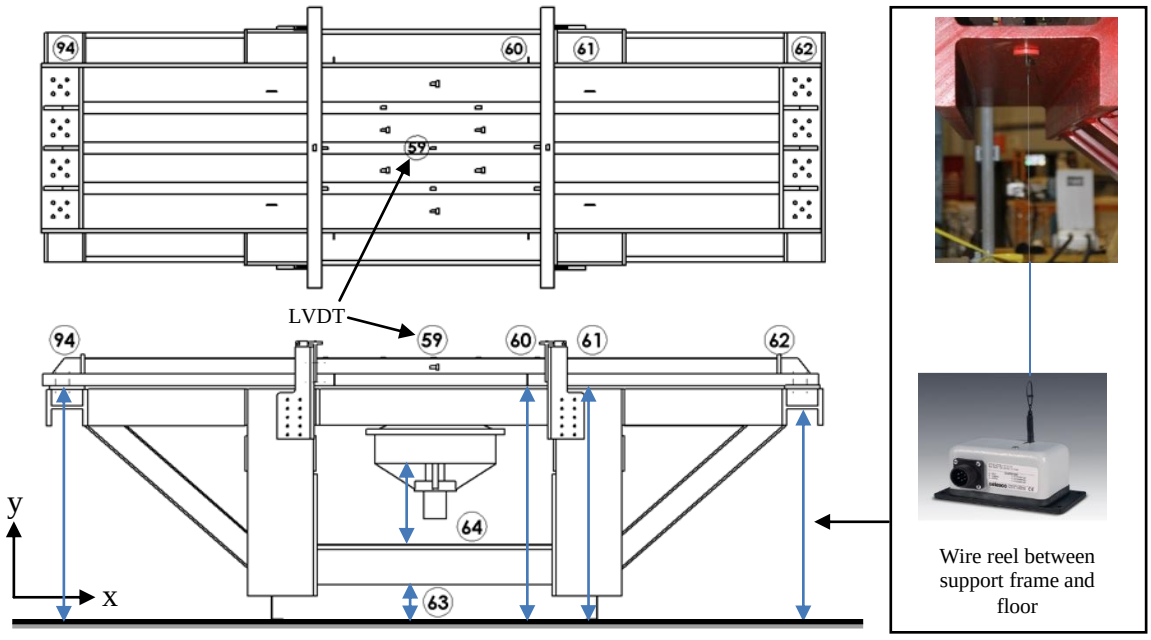

Figure 2-12: Arrangement of position transducers

Also, the hydraulic ram was instrumented with a pressure transducer and a position transducer. The pressure transducer was calibrated to report the reaction force of the grillage in pound-force (lbf) and the position transducer was placed to obtain the hydraulic ram's extension during tests as shown in Figure 2-13.

Figure 2-13: The hydraulic ram outfitted with the pressure transducer and position transducer

2.3.6 Recording and Display Systems

Figure 2-14 shows the arrangement of the video recording and display systems. Two Go-pro® cameras were mounted inside the grillage support frame in order to record videos of ice crushing into the plate. During the tests, the video streams were provided to display screens via Wi-Fi connection. Isometric and side views were obtained by two other Go-pro® cameras installed outside of the grillage support frame. All Go-pro® cameras recorded at 60 ~ 120 frames per second to capture maximum resolution. Moreover, five-second interval time lapse photos of general view were captured by a digital single-lens reflex (DSLR) camera.

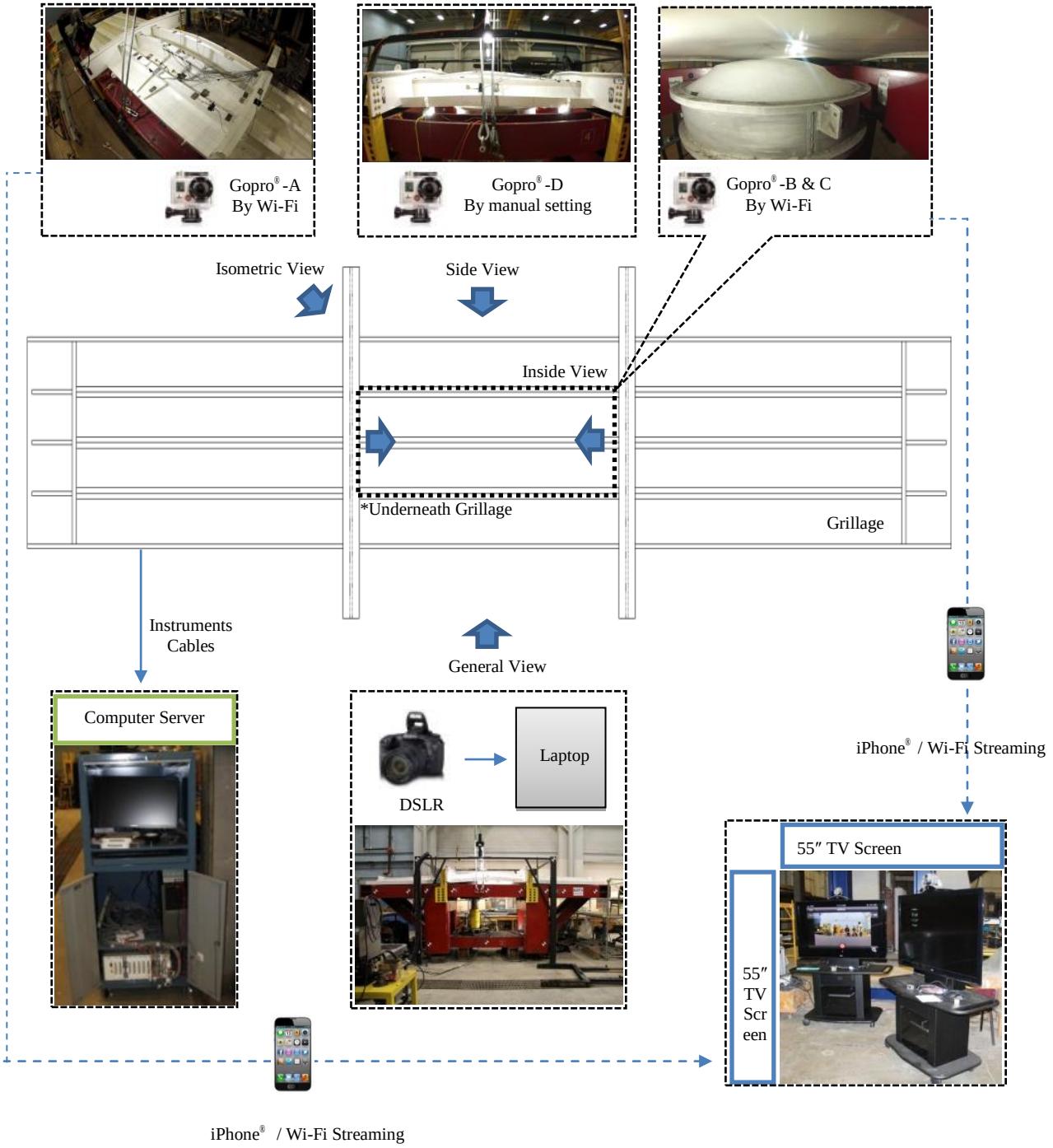

Figure 2-14: Schematic arrangement of the recording and display systems

2.3.7 Handling and Positioning Ice Samples

A large ice sample was mounted on the hydraulic ram by an overhead crane and a forklift. An ice sample can melt at room temperature which can influence the ice properties and affect the test results. Therefore, efficient and careful handling of the ice sample and positioning for the tests was critical.

Figure 2-15: Ice sample fitted into the forklift's fork extension

Figure 2-16: Handling an ice sample using a forklift and overhead crane

2.3.8 Digitizing Deformation using the MicroScribe® 3D Digitizer

A device called the MicroScribe® captures the physical properties of three-dimensional objects and accurately translates them into complete 3D models. In this study, the digitizer was used to translate the deformed shape and deflection of the grillages into a commercial surface modeling software, Rhinoceros® 4.0. These data were subsequently compared with finite element analysis results of the tests shown in chapter 4.

Figure 2-17: MicroScribe® (Solution Technologies Inc.)

Figure 2-18: Scanning deformation using the MicroScribe®

2.4 Boundary Conditions

Most ice class rules and structural standards, including the IACS Unified Requirements for Polar Class Ships (Polar Rules) are based on a single frame in isolation. However, a single stiffener in a ship or an offshore structure is typically connected with neighboring frames along the side shell plate. The boundary condition of a single frame cannot provide the realistic condition of a ship. In this study, grillages are studied as the main component to maintain ship strength.

The grillages were attached to the grillage support frame as rigidly as possible. The longitudinal end of the grillage was bolted to the grillage support frame as shown in Figure 2-19.

The boundary condition for the central frame was designed to provide a realistic condition of a ship's side structure. There are neighboring frames on either side and heavy side bars were added to provide additional restraint at the plates outer edges. The stringers of the grillage were bolted to the grillage support frame using the brackets (see Figure 2-20). The bracket allows stringers to behave as a more realistic boundary condition. The boundary conditions can be considered to restrain all six degree of freedom (All DOF).

Figure 2-19: Boundary conditions at the longitudinal ends

Figure 2-20: Boundary conditions at the stringer ends

2.5 Loading Scenarios

2.5.1 G1T1 & G1T2 (Centre Loading Case)

The tests on Grillage #1 were loaded at the midspan of the central stiffener as shown in Figure 2-21. The first test of Grillage #1 (G1T1) was loaded until the maximum stroke of the ram was reached. Several thick steel plates were then placed under the ram to increase its stroke and perform the second test of Grillage #1(G1T2). The main purpose of these tests was to investigate the ultimate load-carrying capacity of the grillage beyond the design point.

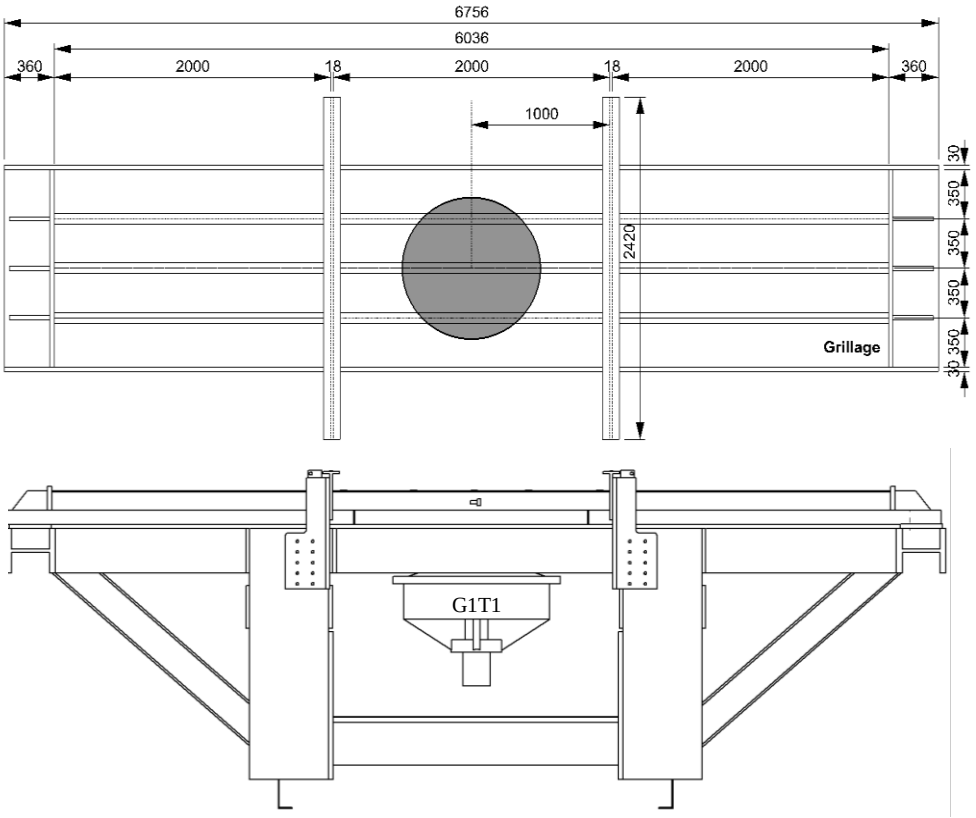

Figure 2-21: G1T1 & G1T2 center loading setup

2.5.2 G2T1, G2T2, and G2T3 (Off-Centre and Centre Loading Cases)

The tests on Grillage #2 were conducted at different loading positions along the length of the central stiffener; right off-centre, centre and left off-centre. Figures 2-22 to 2-24 show the test setup for G2T1, G2T2, and G2T3, respectively. The main purpose of these tests was to investigate the influence of loading nearby the frame supports and prior deformations on the capacity of the grillage. The loading position was 330 mm away from the midspan in G2T1. G2T2 test was conducted consecutively with structural deformation in the previous test using a fresh ice sample. There is a certain influence of the previous damage on the capacity of the grillage. G2T3 test was performed consecutively with structural deformation in the previous two tests using another fresh ice sample.

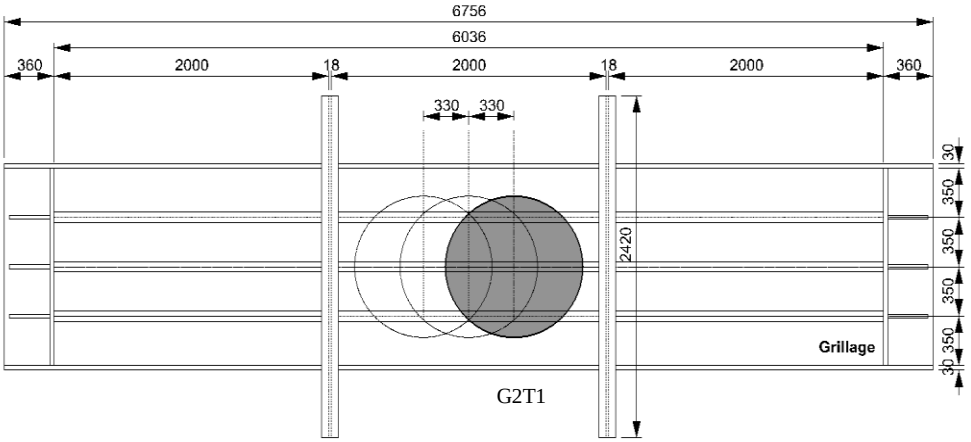

Figure 2-22: The first test of Grillage #2 (G2T1) - right off-centre loading case

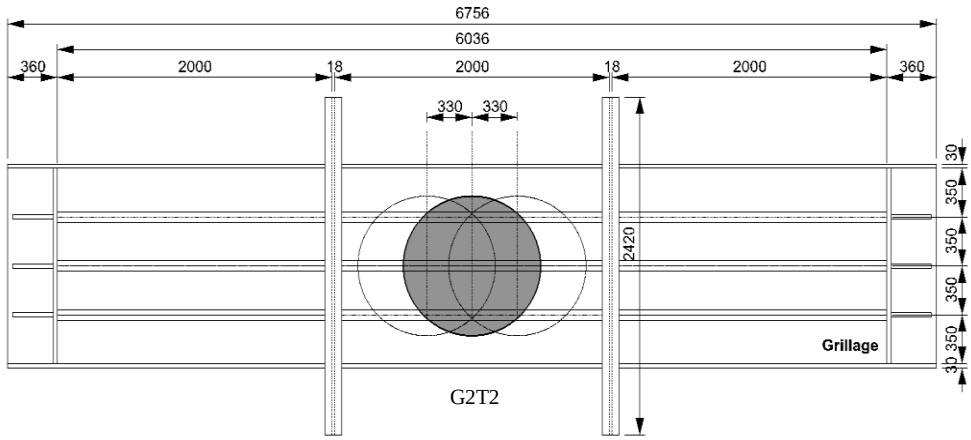

Figure 2-23: The second test of Grillage #2 (G2T2) - centre loading case

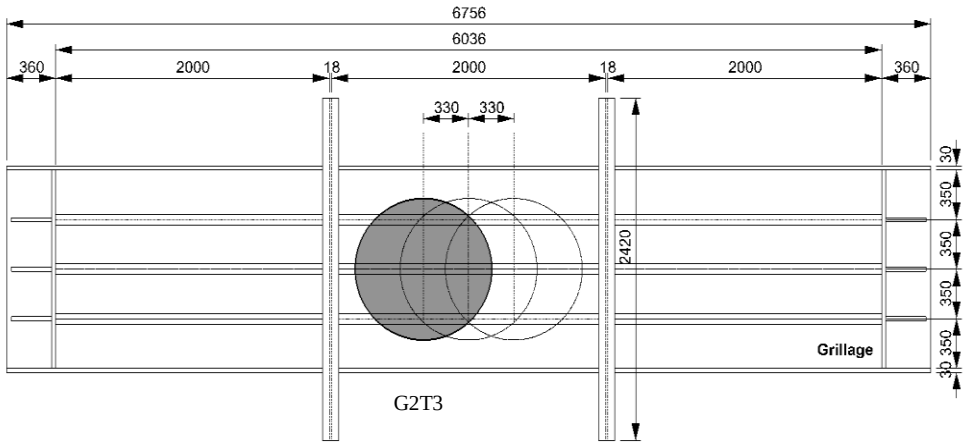

Figure 2-24: The third test of Grillage #2 (G2T3) - left off-centre loading case

2.6 Summary of Experiments

Four laboratory large ice samples were produced and shaped for tests. Instruments were mounted on grillages and the grillage support frame. A 700,000 lbs hydraulic ram was placed below the loading positions prior to each test. The ram was then actuated with 0.5 mm/s ram speed (quasi-static condition).

The tests on Grillage #1 were performed by the identical loading position until the ram stroke reached to its maximum. Grillage #2 tests were carried out by different loading positions; right off-centre, centre and left off-centre.

Table 2-3 shows the schedule of the tests conducted. A total of five tests were successfully performed using two large grillages. The results of the tests will be discussed in the following chapters.

Table 2-3: List of the large grillage tests

Test Name	Load Position	Test Date	Ice Sample
G1T1	Centre	Nov.21,2012	#1
G1T2	Centre	Nov.29,2012	#1
G2T1	Right Off-Centre	Feb.25,2013	# 2
G2T2	Centre	Mar.08,2013	# 3
G2T3	Left Off-Centre	Mar.19,2013	# 4

3 ANALYSIS OF EXPERIMENTAL RESULTS

3.1 Introduction

This chapter presents a detailed analysis of data gathered from the large grillage experiments. First the scantlings of the grillage are checked against the requirements of Ice Class PC6 for a transversely framed configuration and the structural limit states are calculated for the offered dimensions. Load-deflection plots were developed by combining the calibrated forces from the pressure transducer of the hydraulic ram with the deflection from the LVDT attached to the flange of the frame just above the loading position. Shapes of grillage deformation were obtained by the MicroScribe® after each test. Detailed section views are provided and illustrated with dimensions. The isometric, side, inside and general views of the tests are also presented.

The deformation of the grillage support frame was measured from position transducers. This was necessary to check the rigidity of the grillage support frame during the test. Three different methods were used to calculate a contact area between the ice and grillage shell plate in order to study the pressure-area relationships during the crushing process. Finally, uniaxial material tensile tests were conducted to determine the material properties of the steel used to build the grillage.

This chapter presents several plots of data obtained from the experiments and uses photos to support the discussion of the results.

3.2 Framing Design in the Unified Requirements

This section describes a basic check for compliance with the Polar Class Unified Requirements and a sample calculation of the limit states for the offered dimensions as shown in Table 3-1. The calculation procedure is described for obtaining design limit loads for a transversely framed 10,000 ton Ice Class PC6 midbody ice belt arrangement. Two load cases, symmetric and asymmetric are considered.

Ice load parameters are derived taking into account the ice class, ship displacement and class dependant factors defined in the IACS Polar Rules. The average pressure and ice load patch size obtained are 2.69 MPa and 2.24 m x 0.62 m, respectively. Considering the structure as a midbody icebelt arrangement, the average pressure is reduced by a hull area factor, AF = 0.45. In order to check the framing requirements a peak pressure factor, PPF = 1.45, is included. The minimum required shear area and section modulus can be then found by UR equations [I2-22] and [I2-23], with values of 9.4 cm^2 and 238.8 cm^3, respectively. Since the shear area and section modulus are interdependent, the minimum numbers cannot be used directly to create a unique set of scantlings for a given overall configuration consisting of frame span and spacing, load patch dimensions and pressure. Thus, iterations are generally required to find an optimum design considering weight or cost.

The scantlings of the grillage used in the experiments are known. Therefore, the shear area and modulus were calculated and then compared with the required values from the UR equations above in order to check compliance of the requirements.

The offered limit load of the frame of the test grillage can be found using expressions which form the background behind the minimum requirements in the UR [see Equations

(1.43), (1.50), and (1.55)]. Two limit states are considered; the pressure from a central load causing three-hinge collapse and the pressure from an asymmetric load causing combined shear and bending collapse. These limit pressures are 2.30 MPa and 2.29 MPa, respectively. Forces are then derived by multiplying the pressures causing collapse with the area consisting of the spacing (s) between frames and the height (b) of the ice load patch. Those forces, 503 kN and 500 kN respectively, are compared with the experimental results in the load-deflection curves to highlight the overload capacity of the grillage.

Table 3-1: Sample calculations for limit loads

Transversely Framed, 10kT, Mid, PC6						
PC Class	Class		6			
Displacement	Disp	kt	10			
Displacement Class Factor	Cfdis		22			
Crushing Failure Class Factor	CFc		1.8			
Flexural Failure Class Factor	CFf		4.06			
Load Patch Dimensions Class Factor	CFd		1.11			
Load Parameters						
Force	F	MN	3.77			
Aspect Ratio	AR		3.60			
Line Load	Q	MN/m	1.68			
Pressure	P	MPa	2.69			
Ice Load Patch Width	w	m	2.24			
Ice Load Patch Height	b	m	0.62			
Average Patch Pressure	Pavg	MPa	2.69			
Hull Area Factor	AF		0.45			
Corrosion and Abrasion Allowance	t_wear	mm	2.00			
Preak pressure factor	PPF		1.45			
Pressure = Pavg * AF * PPF	P	MPa	1.76			
Framing parameters			**Required by the IACS**		**Offered by the frame**	**Check?**
Structural stability			805.00	>	471	OK
Shell plate thickness (net)	tp	mm	9.60	<	10	OK
Minimum shear area (net)	A0	cm2	9.40	<	16.8	OK
Section modulus (net)	Zp	cm3	238.80	<	325.5	OK
Frame spacing	s	mm			350	
Web height	hw	mm			200	
Web thickness (net)	tw	mm			8	
Flange width	wf	mm			75	
Flange thickness (net)	tf	mm			10	
Span	a	mm			2000	
Material yield strength	σy	MPa			355	
Limit Loads						
Pressure causing asymmetric shear collapse	Ps	MPa			2.29	
Pressure causing 3-hinge collapse	P3h	MPa			2.30	
Force = Ps* s * b	Fs	KN			**499.26**	
Force = P3h * s * b	F3h	KN			**502.87**	

3.3 Grillage #1

3.3.1 G1T1 Result

The tests on Grillage #1 were performed by identical loading position for studying the ultimate load-carrying capacity of the grillage. The first test of Grillage #1 (G1T1) had been performed until the ram stroke reached its maximum.

The deformed shape was obtained using the MicroScribe® (see Figure 3-1). The cross section view of the deformed grillage and ice is illustrated in Figure 3-2. This view indicates that the three longitudinal stiffeners show no buckling behavior at the webs. The central stiffener was still upright and both side stiffeners were slightly inclined towards the outside 6.5 ~ 7.6°. The deflection of the heavy side bars was approximately 22 ~ 25 mm. The contact face between the ice and the grillage was measured to be about 500 mm and was used to calculate an average pressure for non-linear finite element analysis.

The load-deflection curve shows that the maximum vertical deflection was 120 mm at the peak loading of 2.1 MN and about 97 mm of plastic deflection was observed after unloading. The stiffness of the elastic portions of the load-deflection curve, 48.3 kN/mm, was found by dividing the force by the deflection in the elastic range (see Figure 3-3).

The plastic deformation of the grillage support frame, measured by the position transducers was less than a few millimeters, which is negligible considering the large deformations of the grillage (see Figure 3-4).

The isometric, side, inside and general views of the test at the peak loading of 2.1 MN are illustrated in Figures 3-5 to 3-8, respectively. A surface crack in the welds was observed in the grillage as shown in Figure 3-10. Distortion of the longitudinal stiffener occurred in intersection of the stringers (see Figure 3-14).

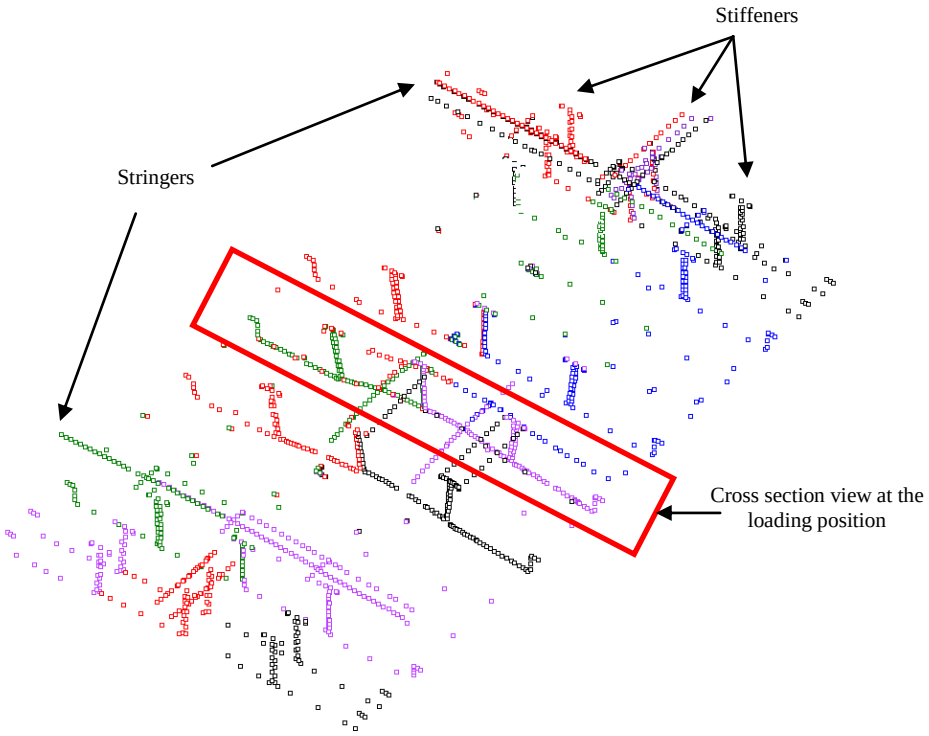

Figure 3-1: Deformed shape of G1T1 using the MicroScribe®

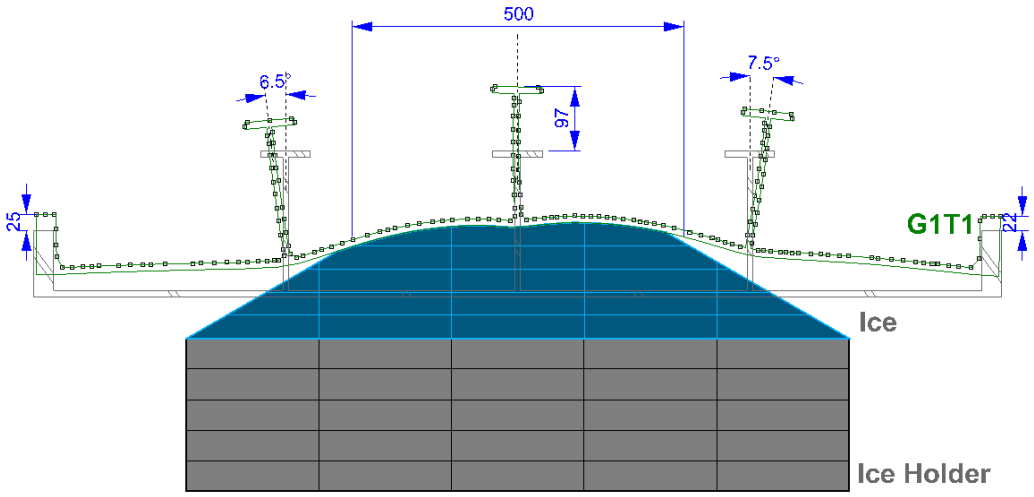

Figure 3-2: Cross section view of G1T1

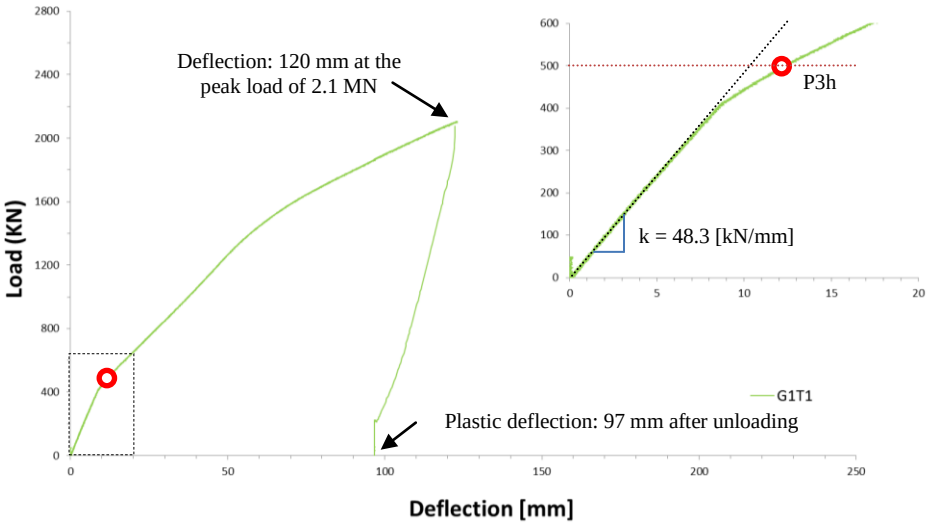

Figure 3-3: Load-deflection curve of G1T1

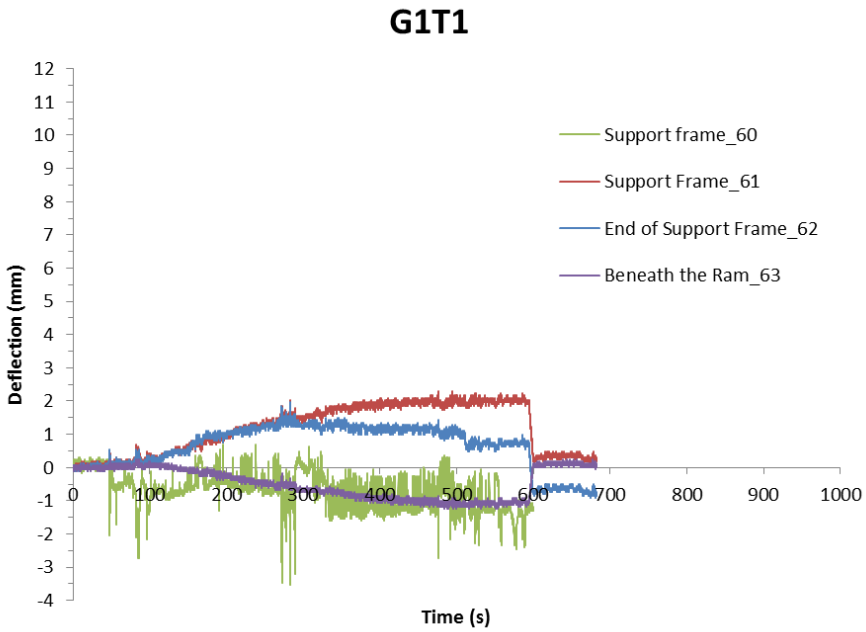

Figure 3-4: Deformation of the grillage support frame of G1T1

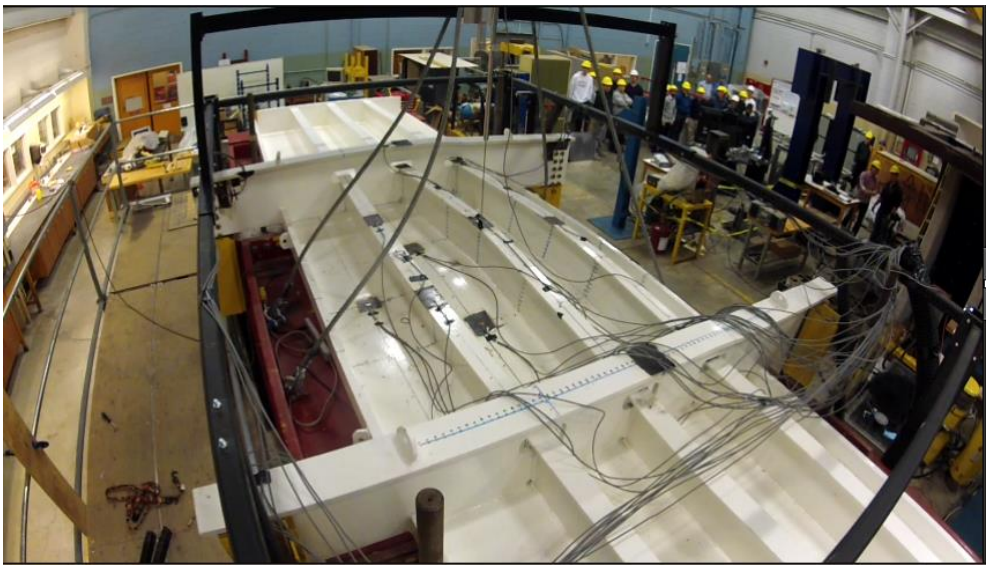

Figure 3-5: Isometric view of G1T1 at 2.1 MN

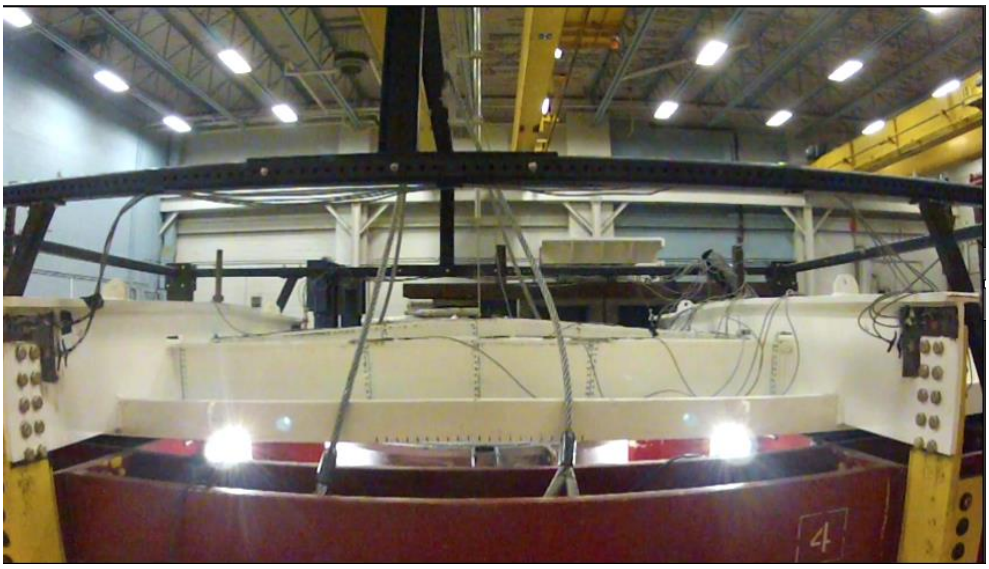

Figure 3-6: Side view of G1T1 at 2.1 MN

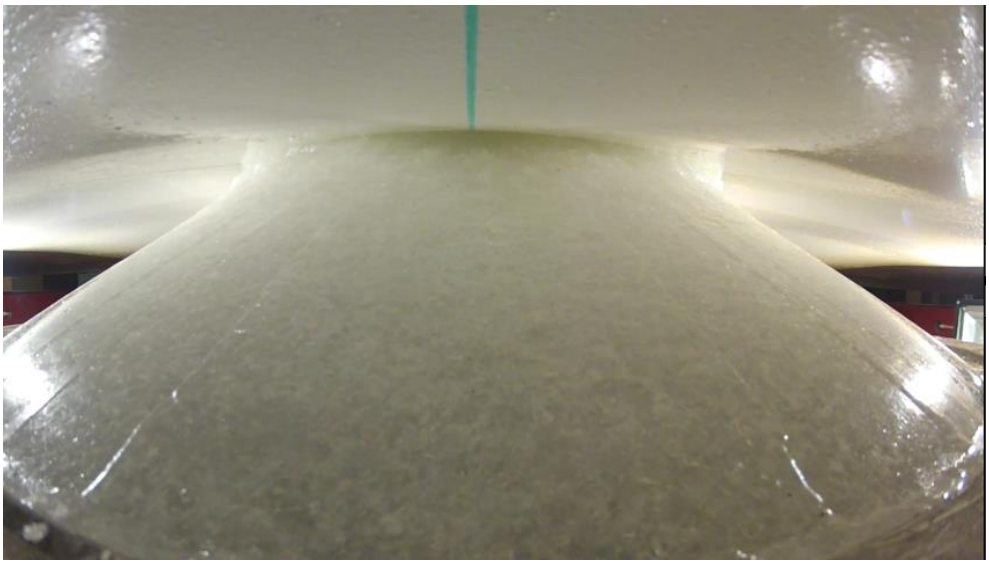

Figure 3-7: Inside view of G1T1 at 2.1 MN

Figure 3-8: General view of G1T1 at 2.1 MN

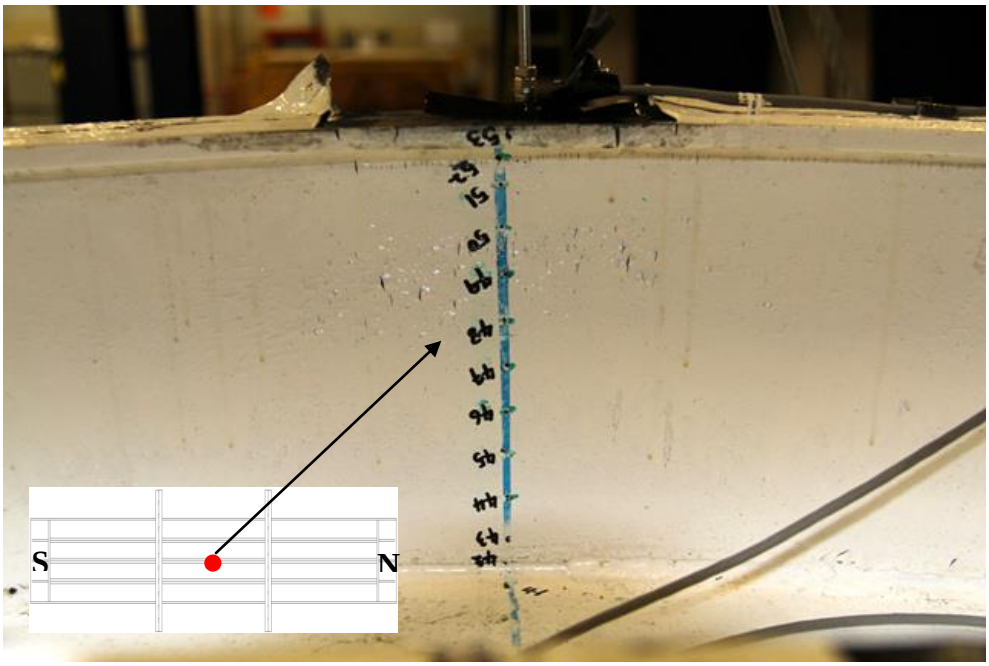

Figure 3-9: Central longitudinal stiffener web

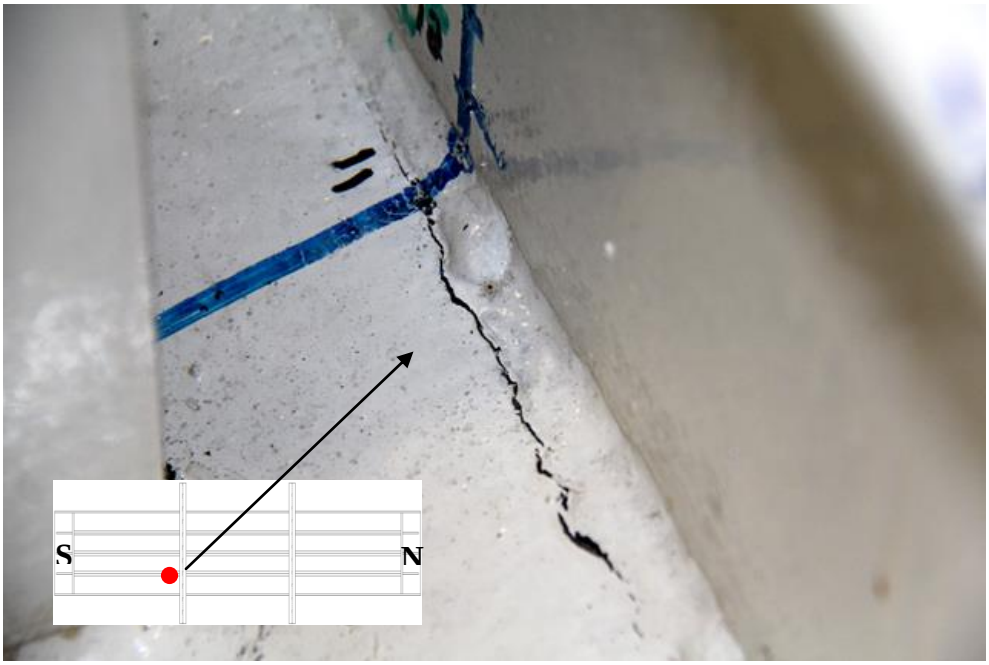

Figure 3-10: Surface crack in the weld

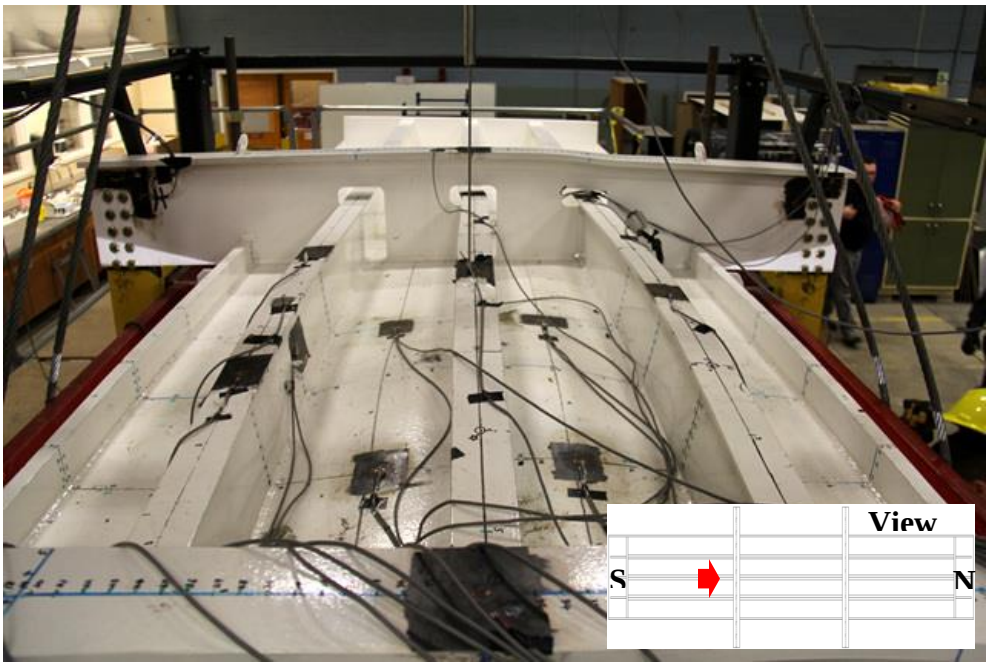

Figure 3-11: Deformation of G1T1

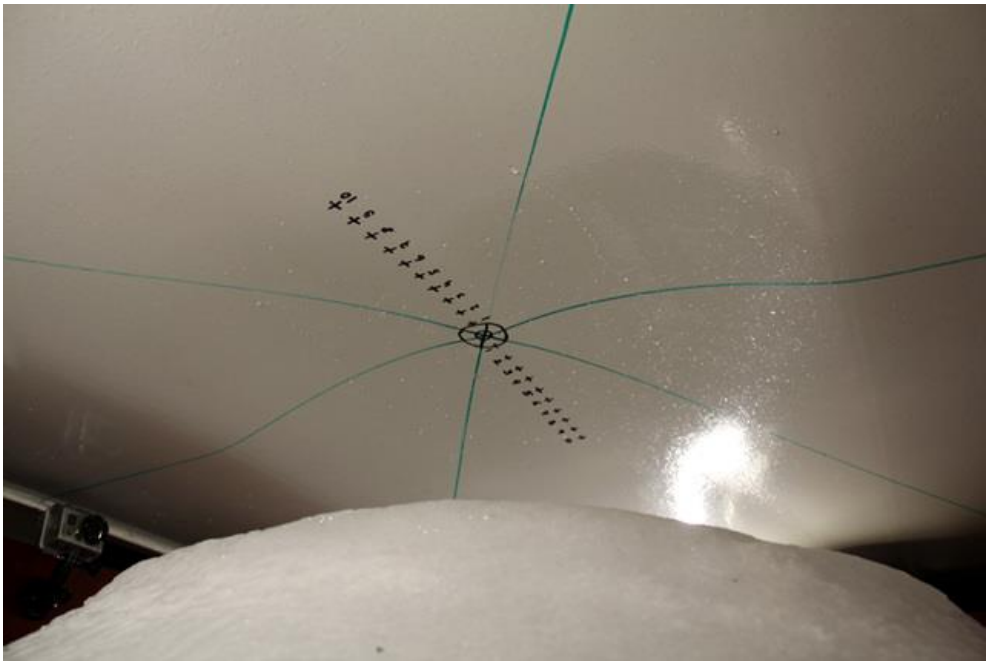

Figure 3-12: Inside view of the grillage support frame after unloading

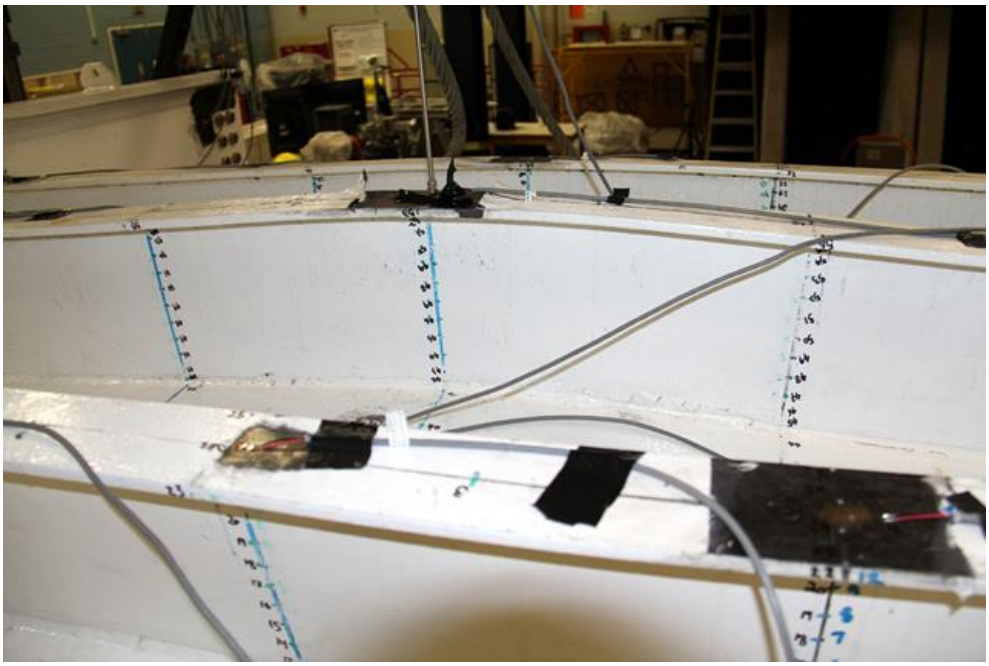

Figure 3-13: Longitudinal stiffeners of G1T1

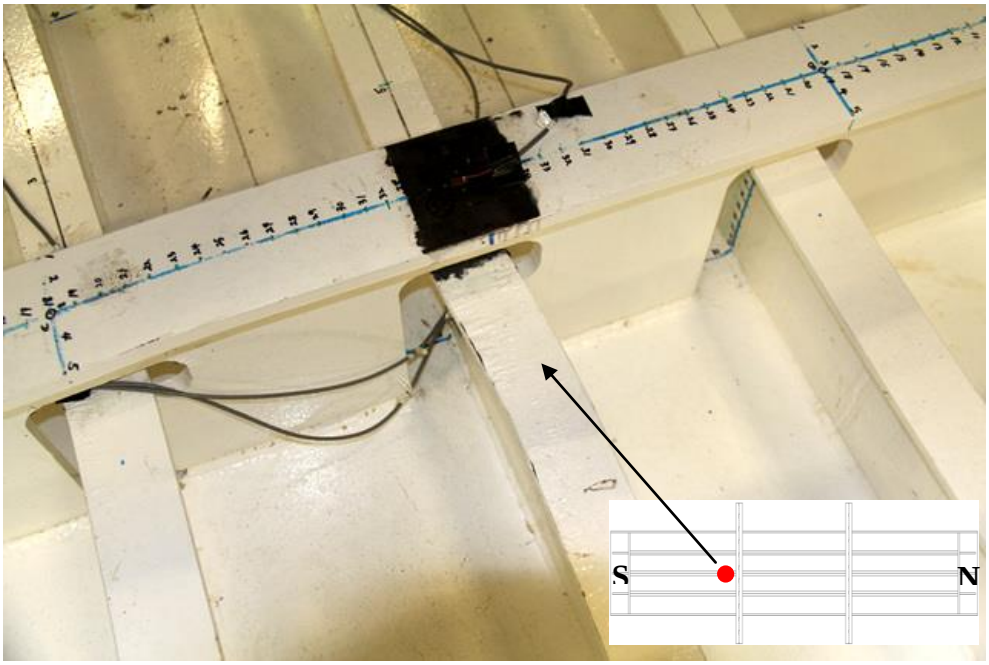

Figure 3-14: Distortion of longitudinal stiffeners near the stringer

3.3.2 G1T2 Result

After completion of G1T1, several thick steel plates were then placed under the ram to increase its stroke (see Figure 3-22). The second test of Grillage #1 (G1T2) was continued using the crushed ice sample in the prior test in order to investigate ultimate load-carrying capacity of the grillage.

The cross section view of the deformed shape of G1T2 is shown in Figure 3-16. It was observed that the central longitudinal stiffener started to fold over when the load reached approximately 2.4 MN and deflection of about 170 mm. The stiffener was folded over about 75° and both side stiffeners were also inclined towards the outside 40 ~ 55°. Approximately 60 mm of maximum vertical deflection was observed at the heavy side bars of the grillage. The contact area between ice and the grillage was 715 mm in diameter.

The deflection was about 215 mm at the peak loading of 2.8 MN and about 170 mm of plastic deflection was observed after unloading. The stiffness of the elastic portions of the load-deflection curves was approximately 83.6 kN/mm (see Figure 3-17).

The deformation on the grillage support frame was observed during the test. Although approximately 11 mm of the elastic deformation in the peak loading and about 4 mm of plastic deflection were occurred in the longitudinal end of the grillage support frame, which is negligible considering the large deformations of the grillage (see Figure 3-18).

The isometric, side, inside and general views of the test are illustrated in Figures 3-19 to 3-22, respectively.

New surface cracks were detected at both ends of the central stiffener, but there were no tears or through-thickness cracks (see Figures 3-23 and 3-24). The crack was observed in

the prior test disappeared during the second test. It seemed that the large deformation of the grillage caused the gap to close.

The longitudinal stiffeners also showed distortion near the cut-out of the stringer (see Figure 3-25). Large deformations were observed in a cut-out of the stringer which is the major supporting member for the stiffeners (see Figure 3-27).

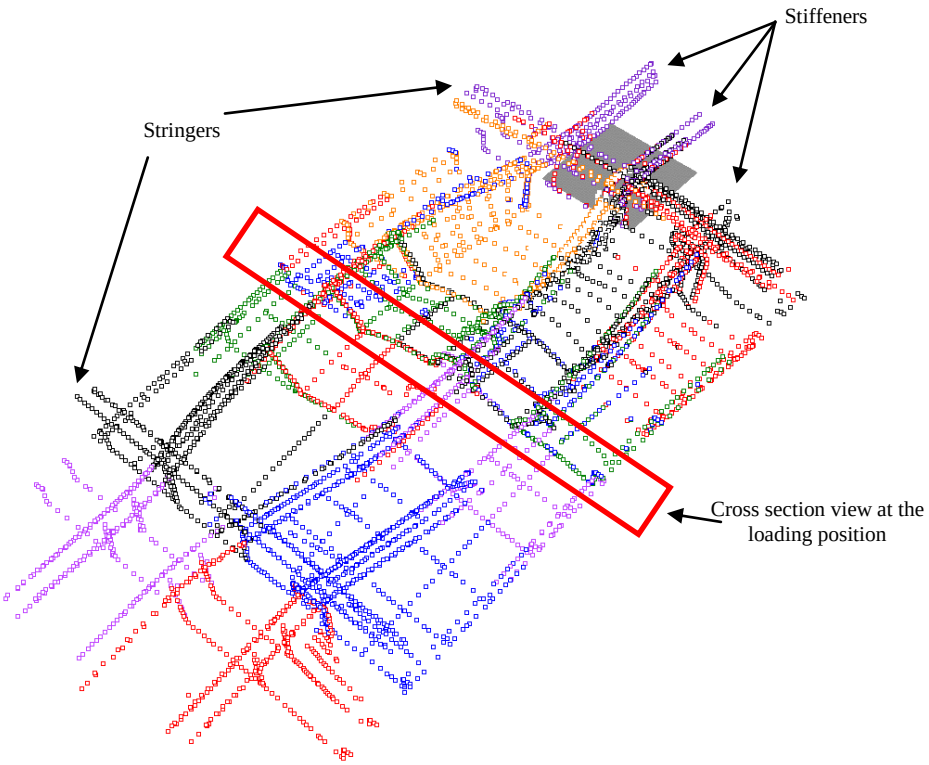

Figure 3-15: Deformed shape of G1T2 using the MicroScribe®

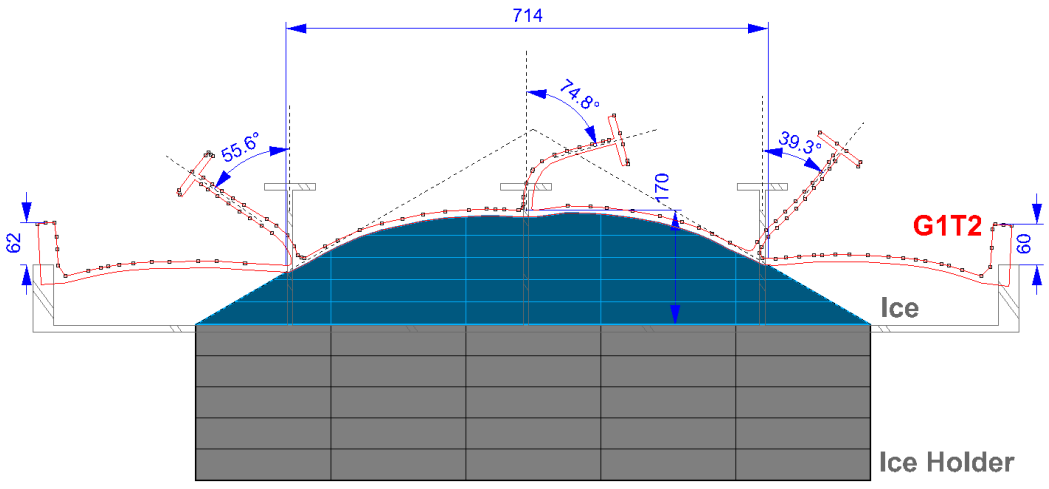

Figure 3-16: Cross section view of G1T2

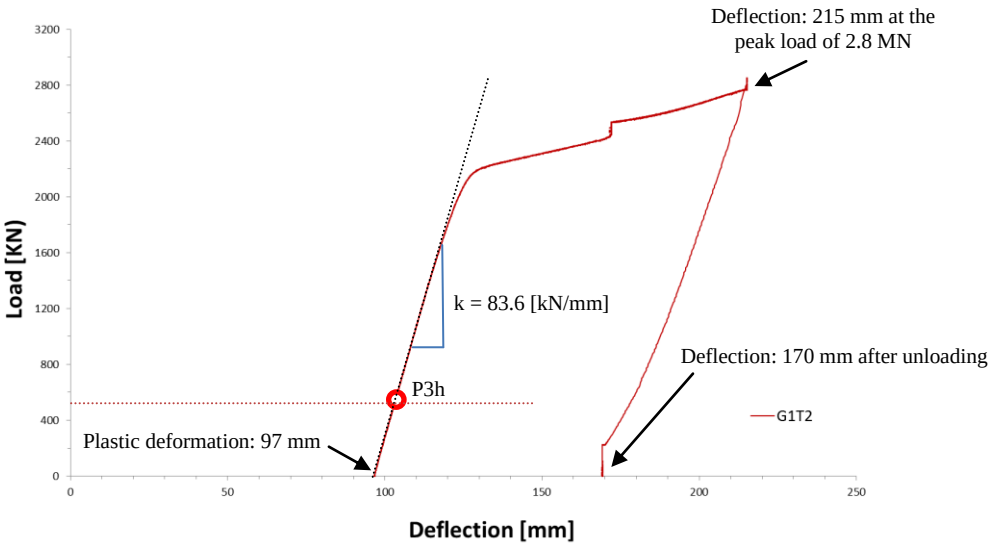

Figure 3-17: Load-deflection curve of G1T2

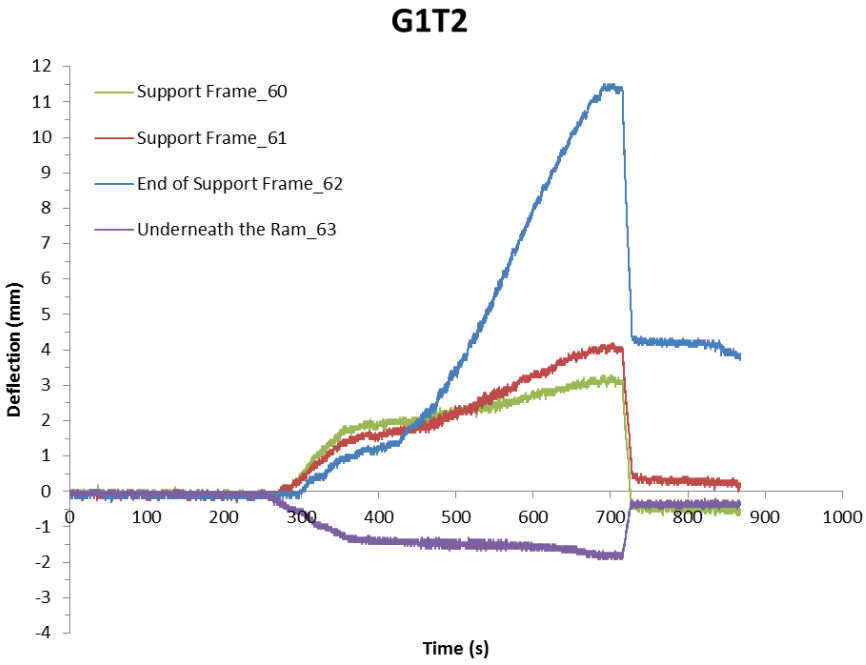

Figure 3-18: Deformation of the grillage support frame of G1T2

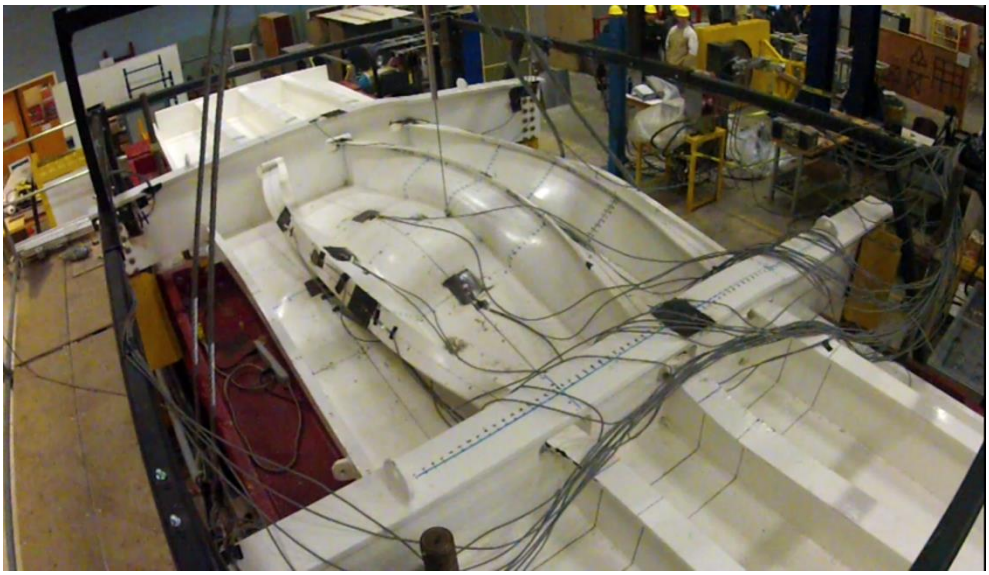

Figure 3-19: Isometric view of G1T2 at 2.8 MN

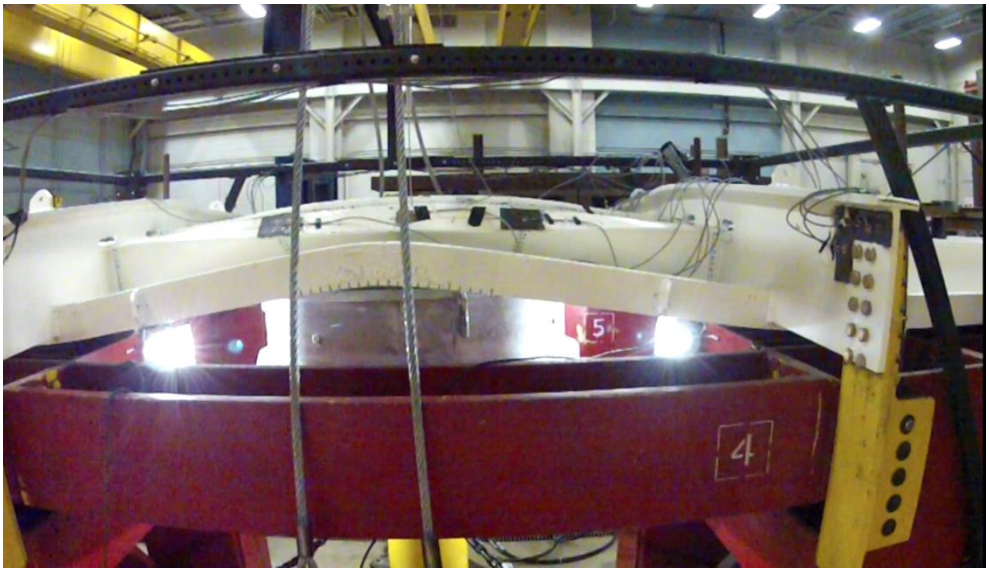

Figure 3-20: Side view of G1T2 at 2.8 MN

Figure 3-21: Inside view of G1T1 at 2.8 MN

Figure 3-22: General view of G1T2 at 2.8 MN

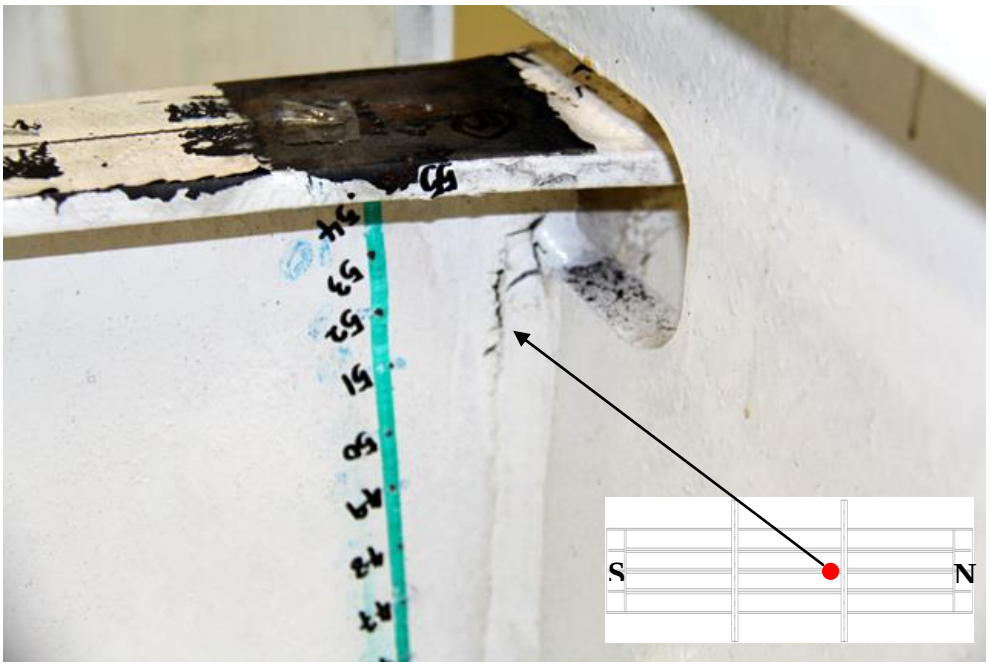

Figure 3-23: Surface crack in the end of the central longitudinal frame

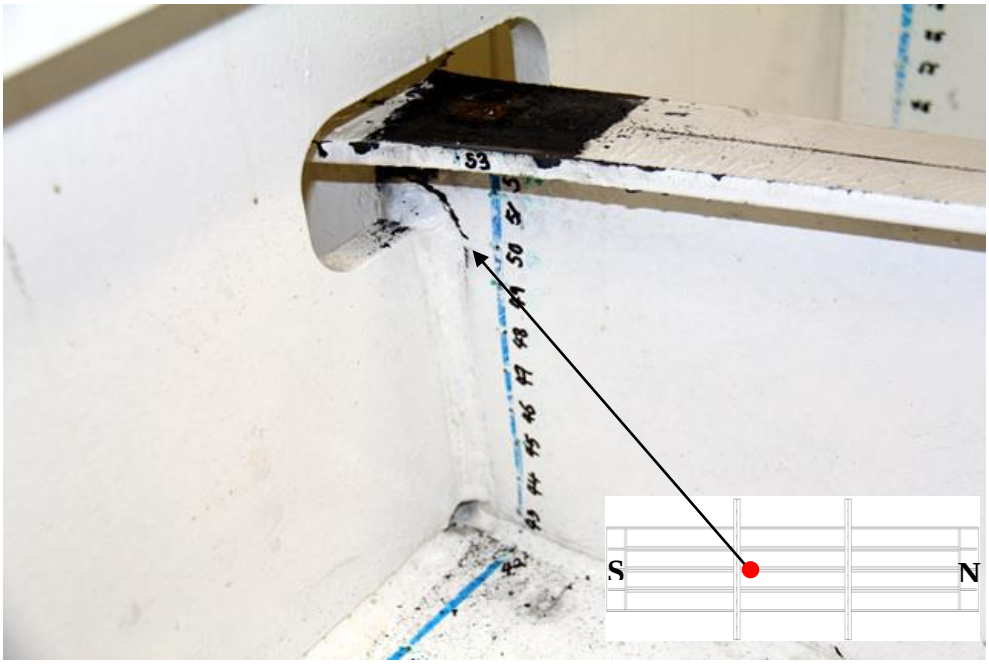

Figure 3-24: Surface crack in the end of the central longitudinal frame

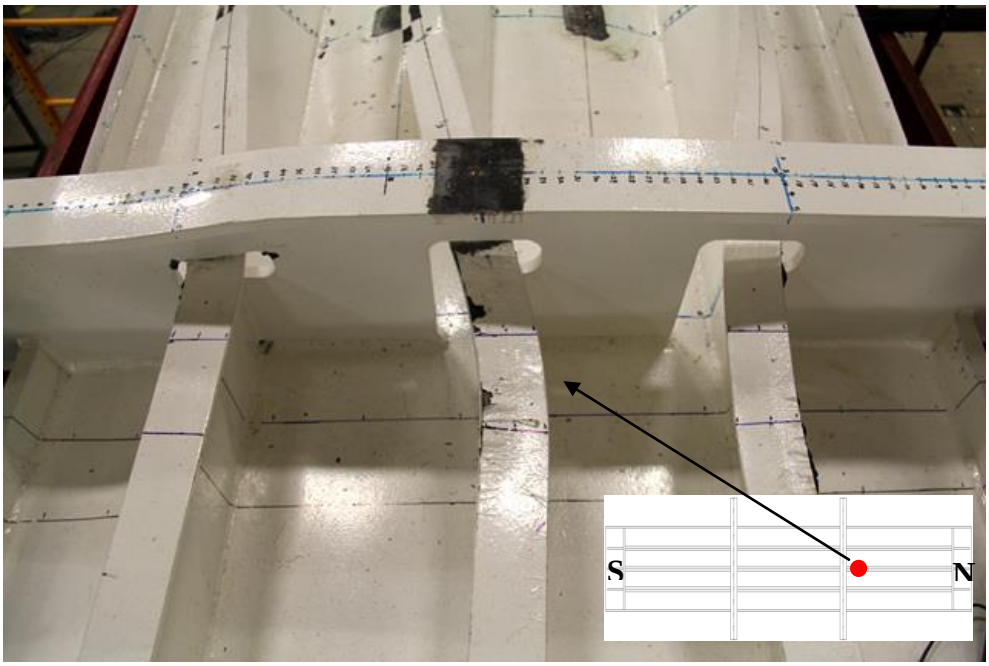

Figure 3-25: Distortion at the end of the longitudinal stiffeners

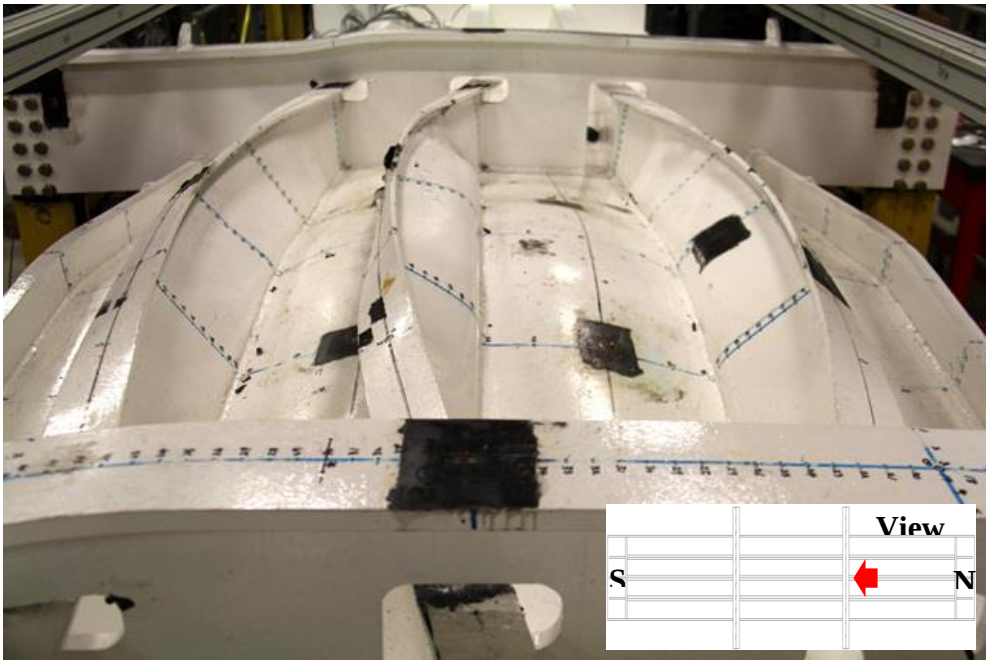

Figure 3-26: Deformation of the longitudinal stiffeners

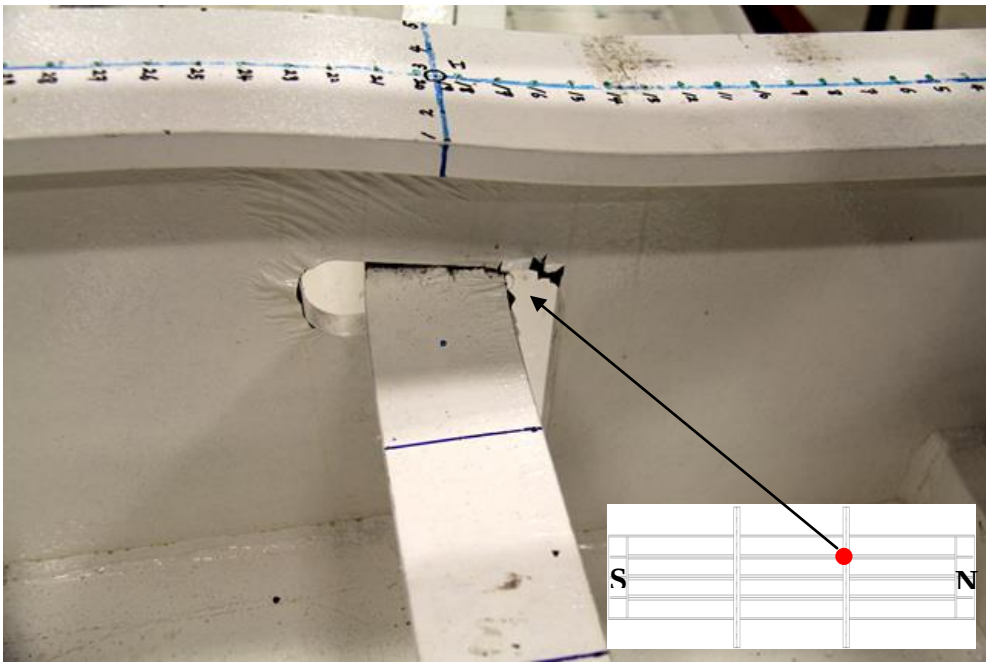

Figure 3-27: Deformation of the cut-out of the stringer

3.3.3 Discussion of Grillage #1

Grillage #1 tests demonstrated significant overload capacity of the grillage when subject to ice loads, with deflections up to 215 mm at the peak loading condition, despite surface cracks that initiated at the ends of the central stiffener. The limit load according to the IACS Polar Rules for this particular structure is approximately 503 kN, and the load-deflection curve shows that the overload capacity of the grillage is much greater than the required rule. The maximum load applied was 2.8 MN which is greater than 5 times the design load (see Figure 3-28).

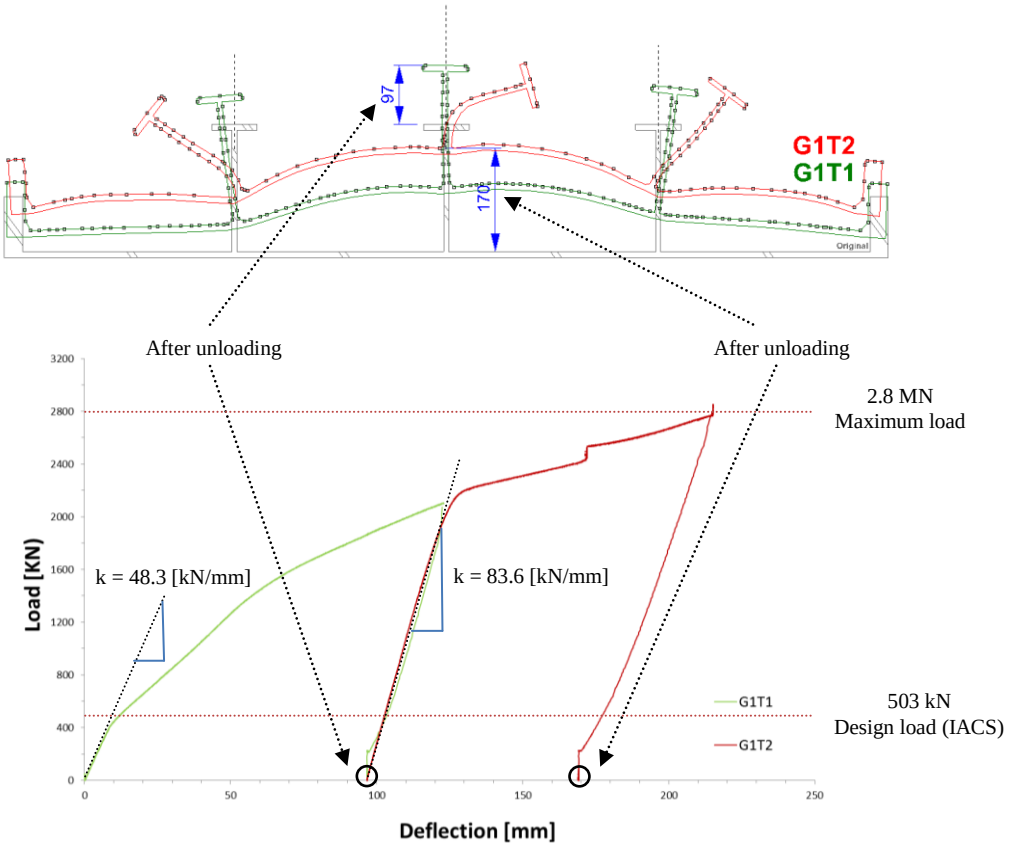

Figure 3-28: Load-deflection curves of Grillage #1 tests

The design load in the IACS Polar Rules is based on a single frame in isolation. These results indicate that a frame surrounded by adjacent frames can sustain higher loads beyond its design point while ice is pushing against them at extremely slow speeds (0.5 mm/s). There was no buckling behavior observed in the web at the 2.1 MN load level but eventually folding over occurred when the load reached about 2.4 MN. Also the stiffness of the elastic portions of the load-deflection curves in the second test (83.6 kN/mm) was about 73 % higher than the first test (48.3 kN/mm). The slope in load-deflection curve implies resisting capacity against deformation. Thus, it can be inferred that prior deformation of the frame leads to greater resisting capacity against further plastic deformation.

Large deformation was observed in a cut-out of the stringer which is the major supporting member for the stiffeners (see Figure 3-27). The IACS Polar Rules do not explicitly provide criteria for stringers and other major supporting members (e.g. web frame). Each classification society's rules are expected to provide criteria for these members; however, further studies on their capacity and the influence of stiffeners and other secondary members are necessary to complete the Unified Requirements.

The intention of the experiment was to study the ultimate load-carrying capacity of the grillage; however, given the limit of the hydraulic ram stroke it was not able to reach the maximum load before tearing or rupture. The deformation of ice may contribute to this lack of steel rupture since the load becomes more distributed. These experimental results suggest that the local deformations (up to 11 % of the frame span) do not necessarily compromise the overall strength of the large grillage. In fact the grillage actually gains stiffness and exhibits higher load-carrying capacity when there is prior deformation.

3.4 Grillage #2

3.4.1 G2T1 Result

The loading position of the first test of Grillage #2 (G2T1) was 330 mm away from the midspan of the central stiffener. The cross section view of the deformed shape and ice was illustrated in Figure 3-30. Three longitudinal stiffeners show no buckling behavior at the webs. The central stiffener was still upright but slightly inclined about 5.6°. The both side stiffeners were inclined towards outside about 5 and 12°. The deflection of the heavy side bars were 18 mm and 33 mm, respectively. The contact face between ice and the grillage was about 650 mm.

The load-deflection curve shows that the maximum vertical deflection was 150 mm at the peak loading of 2.3 MN and about 120 mm of plastic deflection was observed after unloading. The stiffness of the elastic portions of the load-deflection curves was approximately 52 kN/mm.

Larger deformation was observed on the grillage support frame during G2T1 test compared with G1T1 test (similar load levels). Approximately 11 mm of maximum deflection was measured at the peak load and about 4 mm of plastic deflection occurred at the both longitudinal ends of the grillage support frame (see Figure 3-32). It is possible that the grillage support frame became slightly loosened after experiencing extreme loading in the prior tests (G1T2), up to 2.8 MN. However, relative to the large plastic deformation of the grillage, it can be assumed that the deformation of the grillage support frame is negligible. The side and general views of the test at the peak loading of 2.3 MN are illustrated in Figures 3-33 and 3-34, respectively. No cracks or distortion of the longitudinal stiffeners were observed (see Figure 3-35).

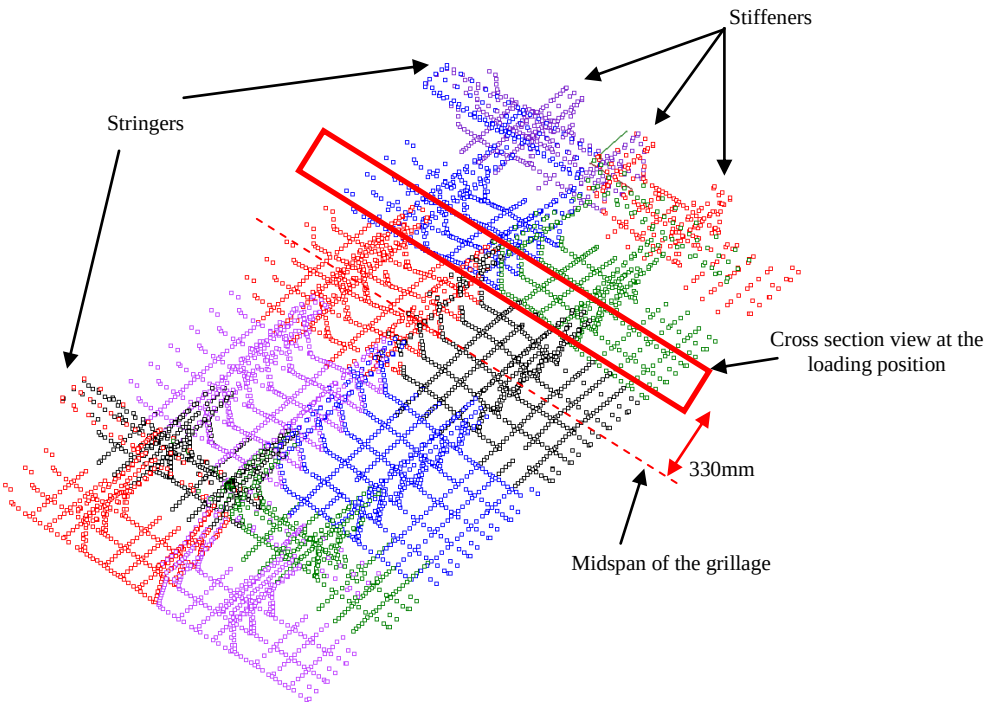

Figure 3-29: Deformed shape of G2T1 using the MicroScribe®

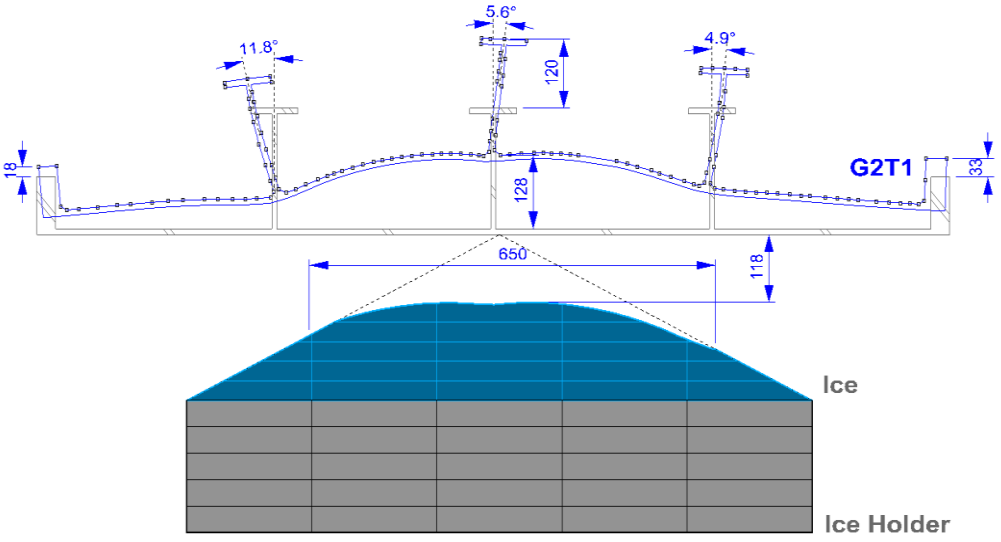

Figure 3-30: Cross section view of G2T1

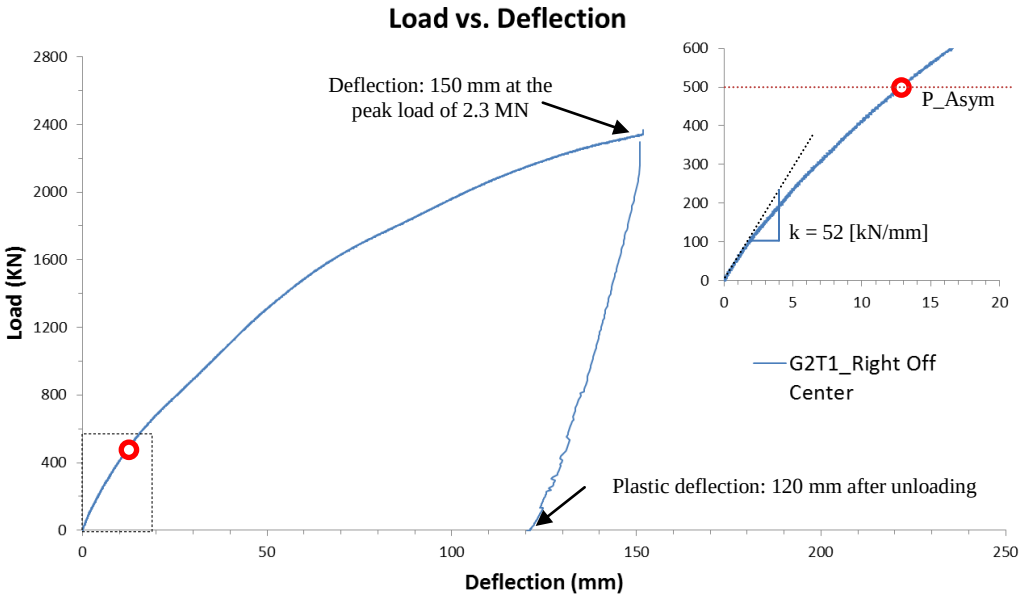

Figure 3-31: Load-deflection curve of G2T1

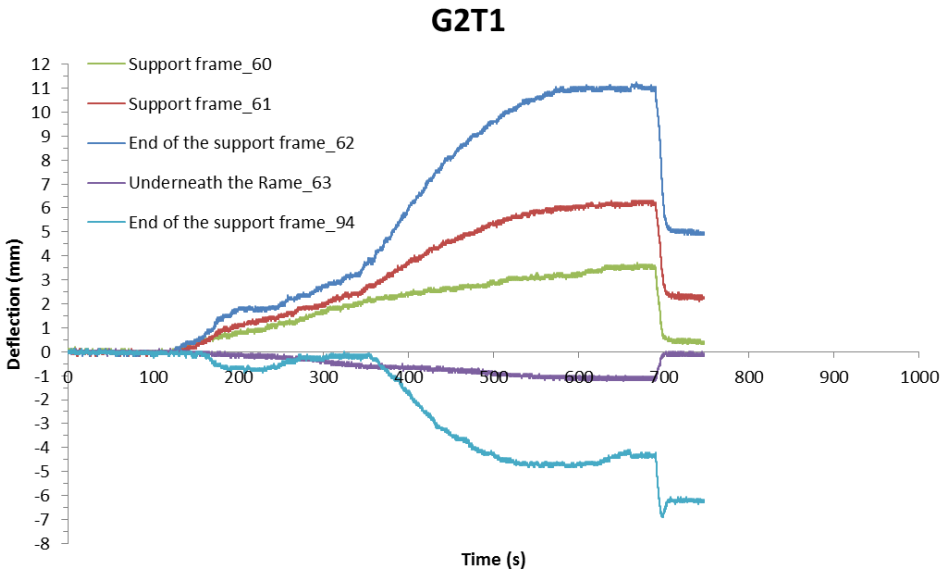

Figure 3-32: Deformation of the grillage support frame of G2T1

Figure 3-33: Side view of G2T1 at 2.3 MN

Figure 3-34: General view of G2T1 at 2.3 MN

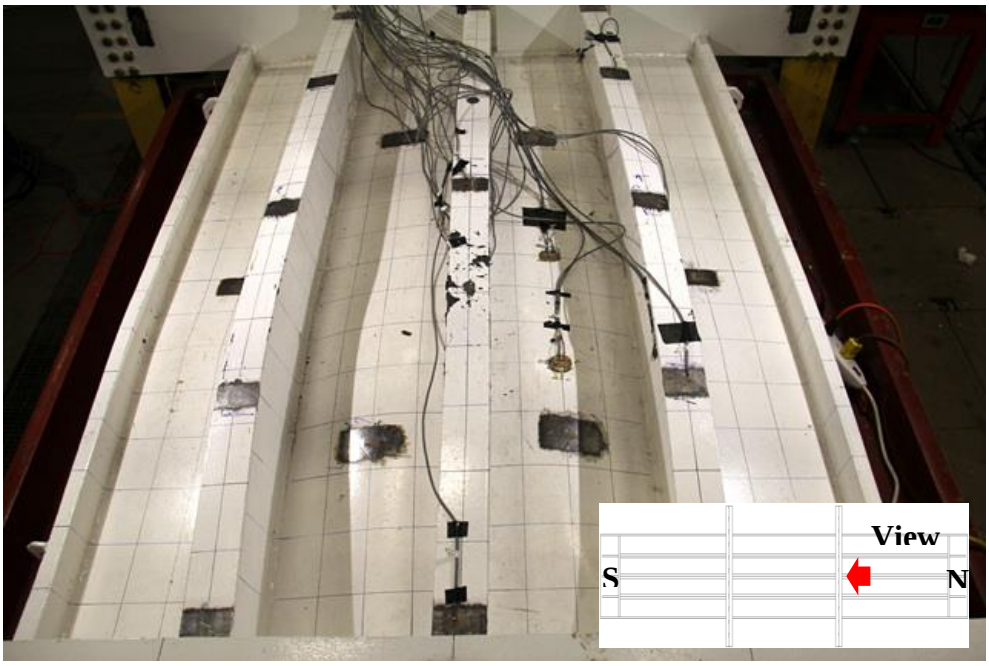

Figure 3-35: Deformation of G2T1

3.4.2 G2T2 Result

The loading position of the second test of Grillage #2 (G2T2) was at the midspan of the central stiffener. It should be noted that this test was conducted consecutively with structural deformation in the previous test using a fresh ice sample. The cross section view of the deformed shape and ice is then shown in Figure 3-37. There was no buckling behavior observed at the webs of three longitudinal stiffeners. The stiffeners were slightly inclined toward outside about 10 ~ 12°. The deflection of the heavy side bars were about 33 ~ 36 mm. The contact face between ice and the grillage was measured to be about 520 mm.

The load-deflection curve shows that the maximum vertical deflection was 140 mm at peak loading of 2.1 kN and about 120 mm of deflection was observed after unloading. The stiffness of the elastic portions of the load-deflection curves was approximately 68 kN/mm (see Figure 3-38).

Deformation of the grillage support frame was observed during the test. Approximately 7 mm of the elastic deformation in the peak loading and about 2 mm of plastic deflection was occurred in the both longitudinal ends of the grillage support frame (see Figure 3-39). The isometric, side, inside and general views of the test at the peak loading of 2.1 MN are illustrated in Figures 3-40 to 3-43, respectively.

No cracks or distortion of the longitudinal stiffeners were observed (see Figure 3-44).

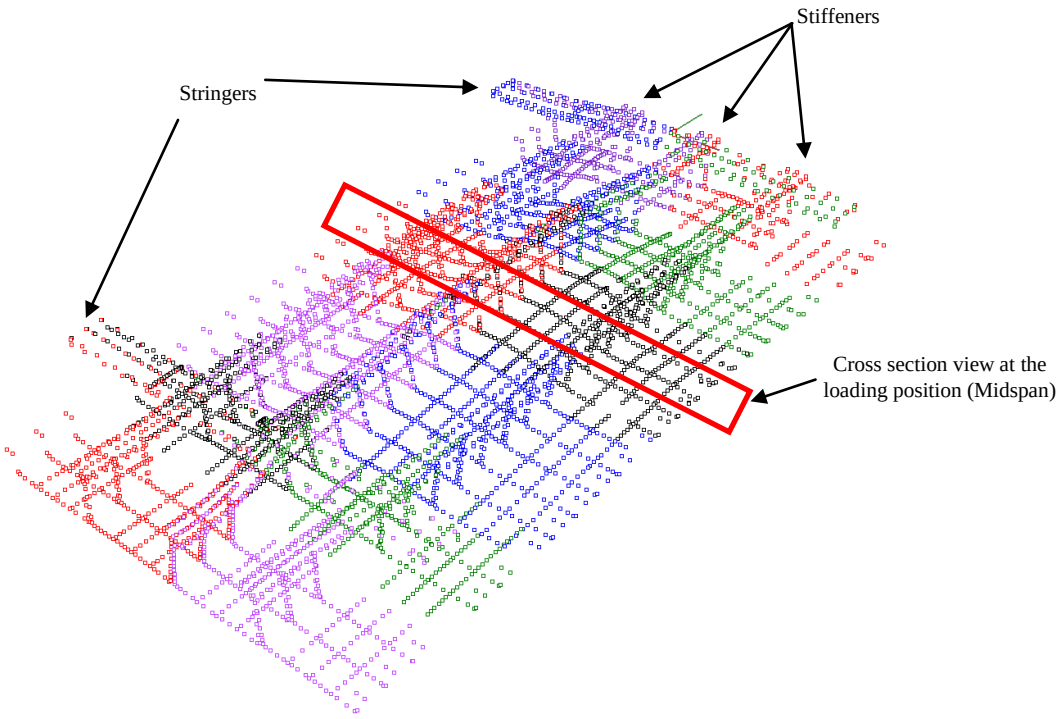

Figure 3-36: Deformed shape of G2T2 using the MicroScribe®

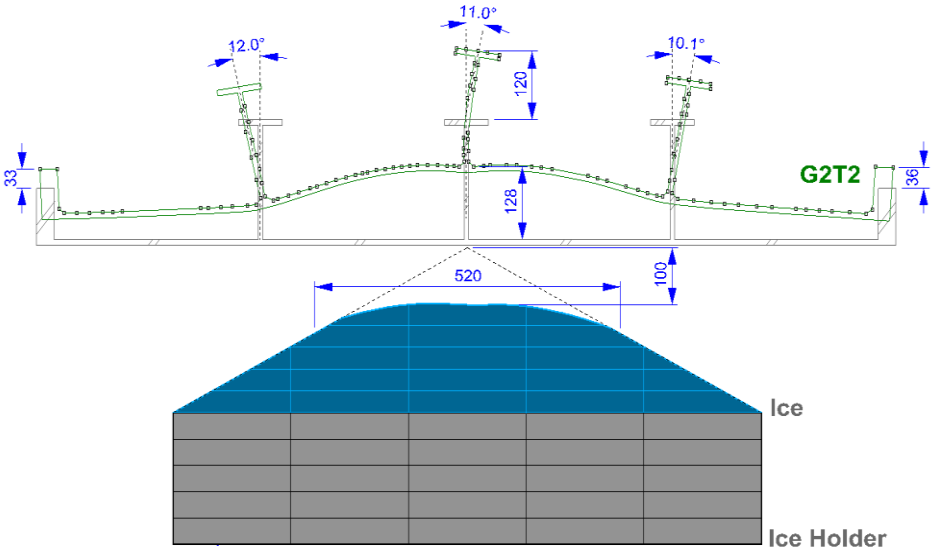

Figure 3-37: Cross section view of G2T2

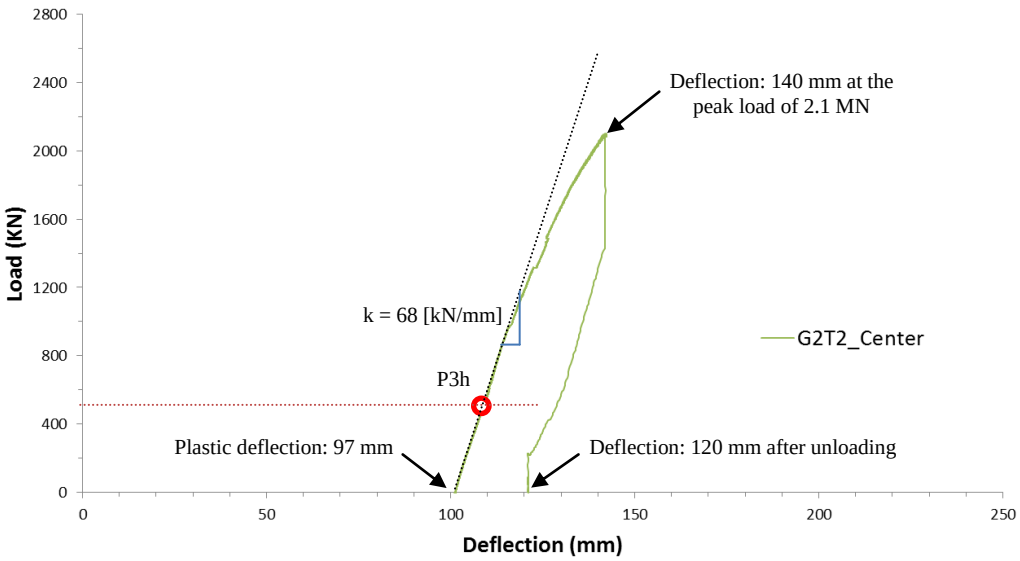

Figure 3-38: Load-deflection curve of G2T2

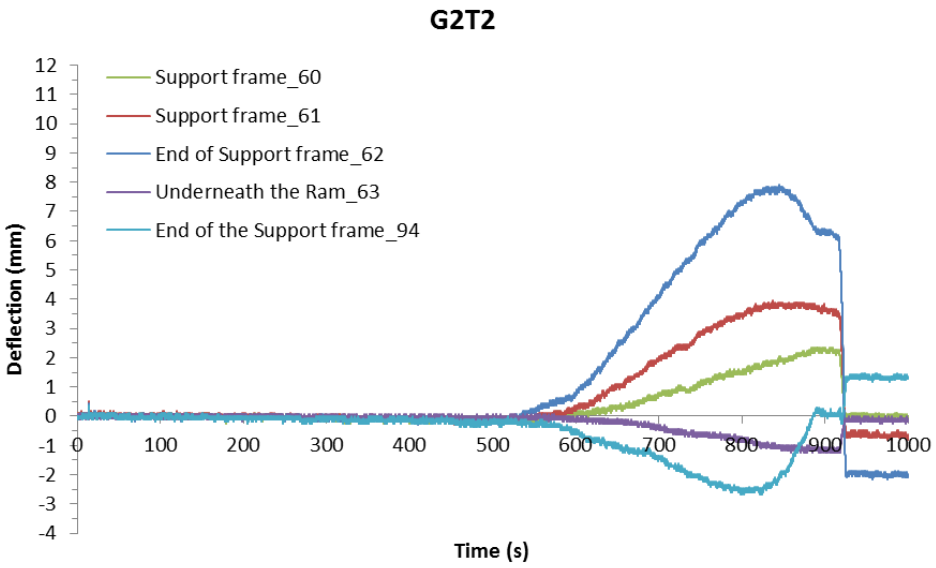

Figure 3-39: Deformation of the grillage support frame of G2T2

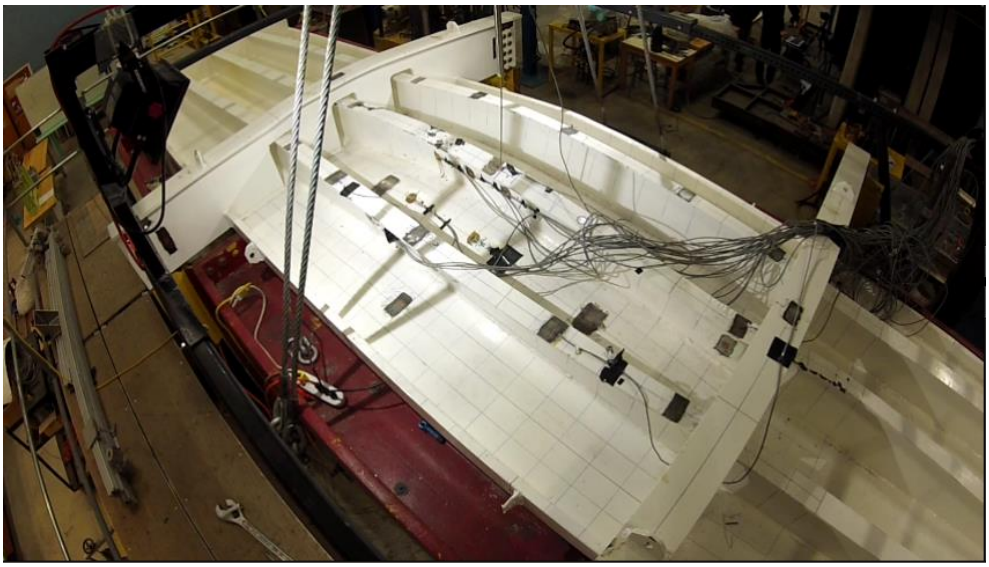

Figure 3-40: Isometric view of G2T2 at 2.1 MN

Figure 3-41: Side view of G2T2 at 2.1 MN

Figure 3-42: Inside view of G2T2 at 2.1 MN

Figure 3-43: General view of G2T2 at 2.1 MN

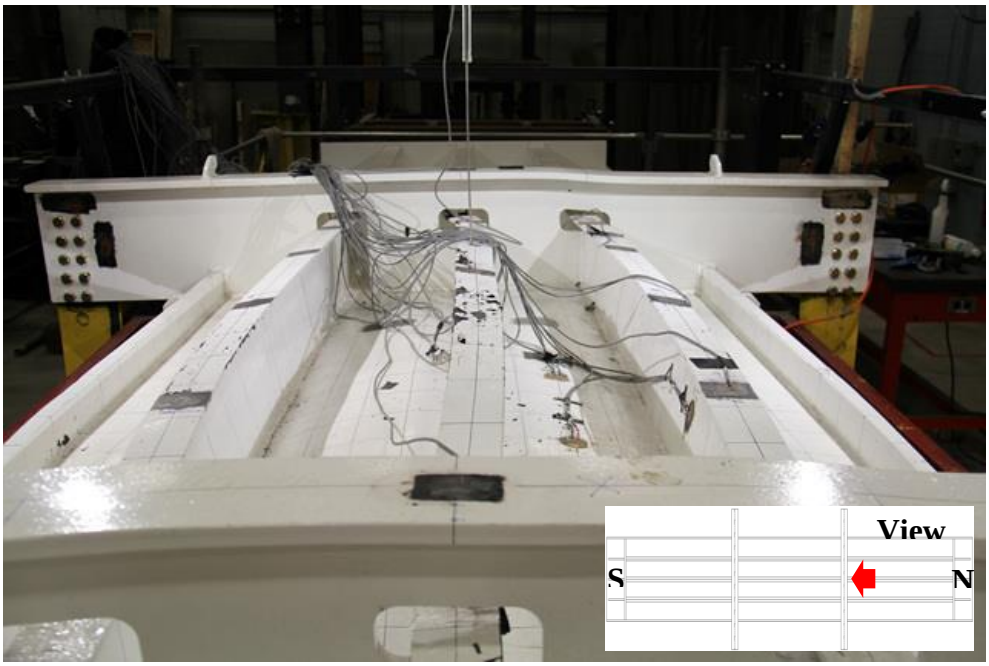

Figure 3-44: Deformation of G2T2

3.4.3 G2T3 Result

The loading position of the third test of Grillage #2 (G2T3) was 330 mm away from the midspan of the central stiffener. It should be noted that this test was conducted consecutively with structural deformation in the previous two tests using a new ice sample. The cross section view of the deformed shape and ice is shown in Figure 3-46. Three longitudinal stiffeners show no buckling behavior at the webs. The stiffeners were slightly inclined towards outside about 9.5 ~ 12.3°. The deflection of the heavy side bars were about 30 ~ 32 mm. The contact face between ice and the grillage was measured was about 570 mm.

The load-deflection curve shows that the maximum vertical deflection was 150 mm at peak loading of 2.3 MN and about 123 mm of plastic deflection was observed after unloading. The stiffness of the elastic portions of the load-deflection curves was approximately 71 kN/mm (see Figure 3-47).

The deformation of the grillage support frame can be negligible considering the large plastic deformation of the grillage (see Figure 3-48).

The isometric, side, inside and general views of the test at the peak loading of 2.3 MN are illustrated in Figures 3-49 to 3-52, respectively.

There was no evidence of surface cracks or distortion of the longitudinal stiffeners observed during the test.

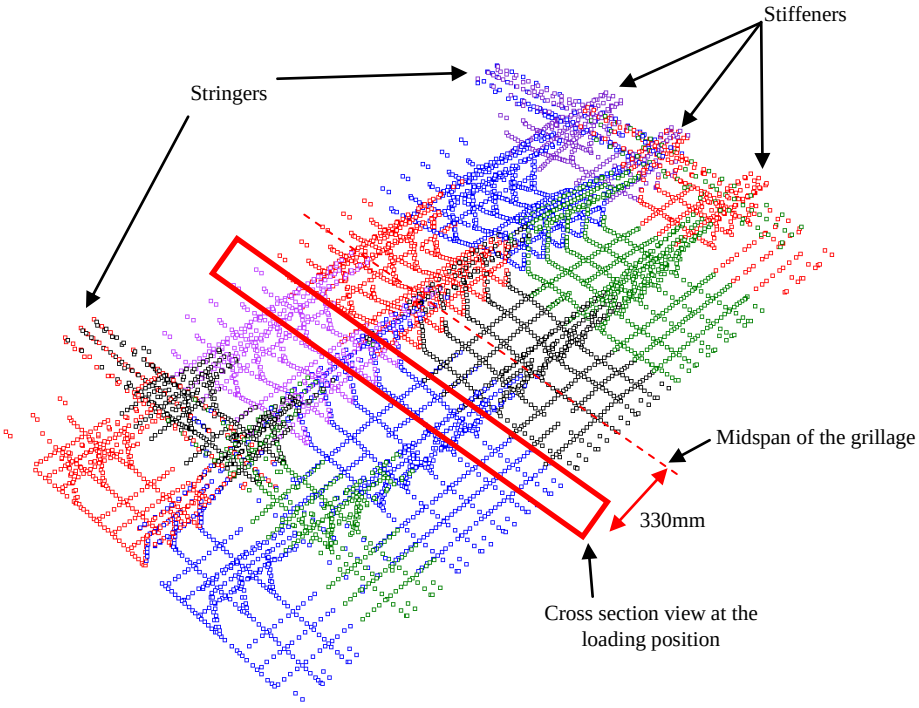

Figure 3-45: MicroScribe® points of the deformed shape of G2T3

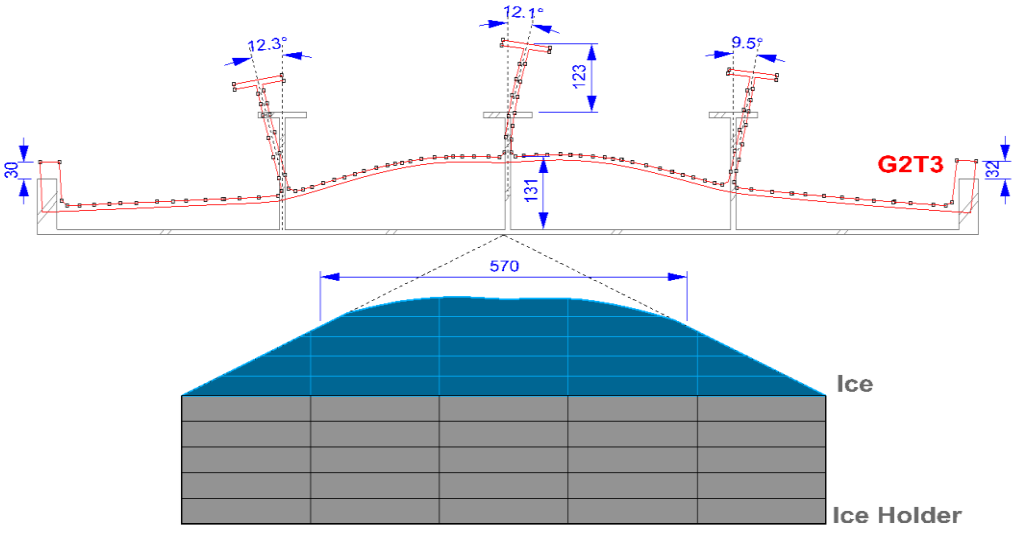

Figure 3-46: Cross section view of G2T3

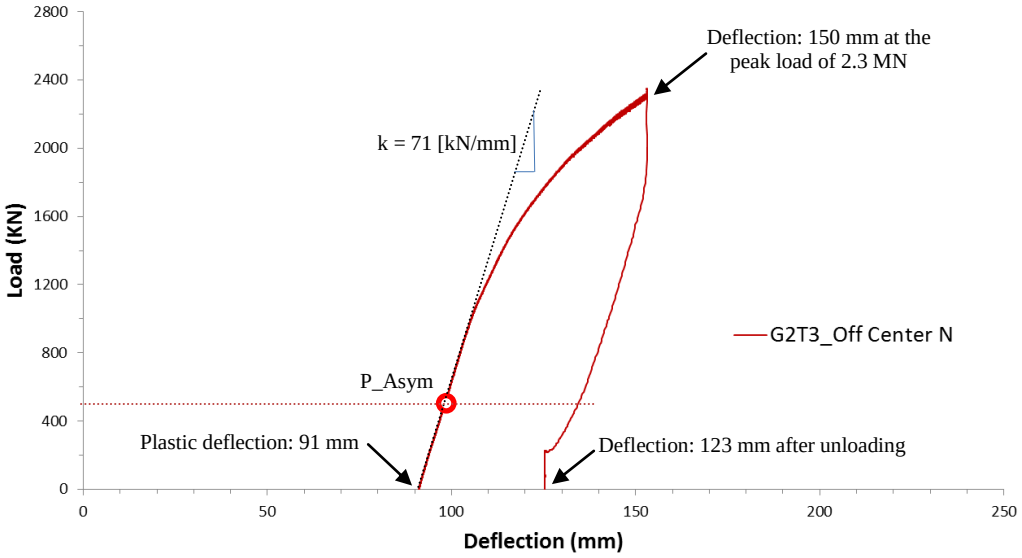

Figure 3-47: Load-deflection curve of G2T3

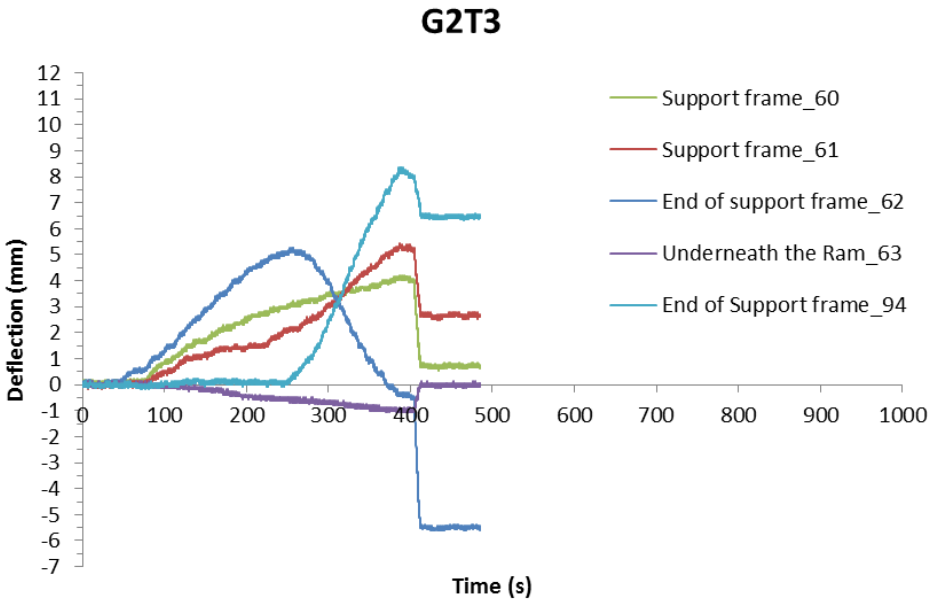

Figure 3-48: Deformation of the grillage support frame of G2T3

Figure 3-49: Isometric view of G2T3 at 2.3 MN

Figure 3-50: Side view of G2T3 at 2.3 MN

Figure 3-51: Inside view of G2T3 at 2.3 MN

Figure 3-52: General view of G2T3 at 2.3 MN

3.4.4 Discussions of Grillage #2

Grillage #2 load cases were carried out sequentially with fresh ice samples applied to the deformed grillage from the previous cases. It was observed that the stiffness of the elastic portions of the load-deflection curves in the second and third tests were higher than the first test (see Figure 3-53). The slope in load-deflection curve implies the resisting capacity against deformation. Thus, these experiments suggest that prior plastic deformations at nearby locations do not necessarily compromise the overall strength of the grillage.

The limit load for asymmetric load based on the IACS Polar Class rules for this structure is approximately 500 kN, and the load-deflection curve shows that the overload capacity of the grillage is much greater than the required rule. The maximum load applied was 2.3 MN which is greater than 4 times the design load.

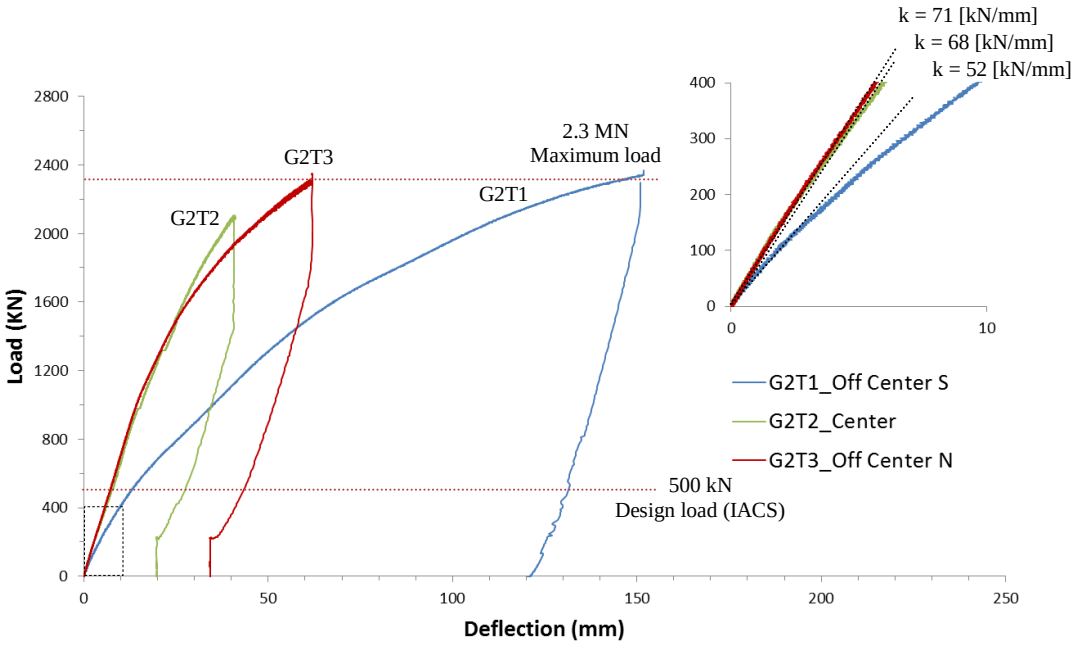

Figure 3-53: Load-deflection curves of Grillage #2 Tests

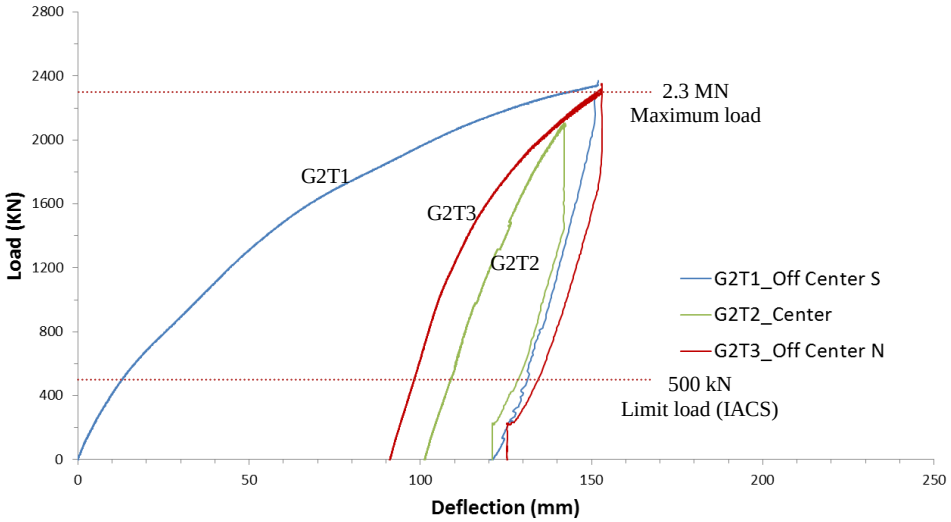

Figure 3-54: Load-deflection curves of Grillage #2 Tests (G2T2 and G2T3 considers prior test deformation)

Cross section views are shown for three positions along the span of the grillage and deformation shapes are overlaid for each test (see Figures 3-55 to 3-57). Deformation slowly progressed during repeated loading but there were no rapid drops of strength observed for the grillage. These experiments suggest that prior plastic damages at nearby locations do not necessarily compromise the overall strength of the grillage.

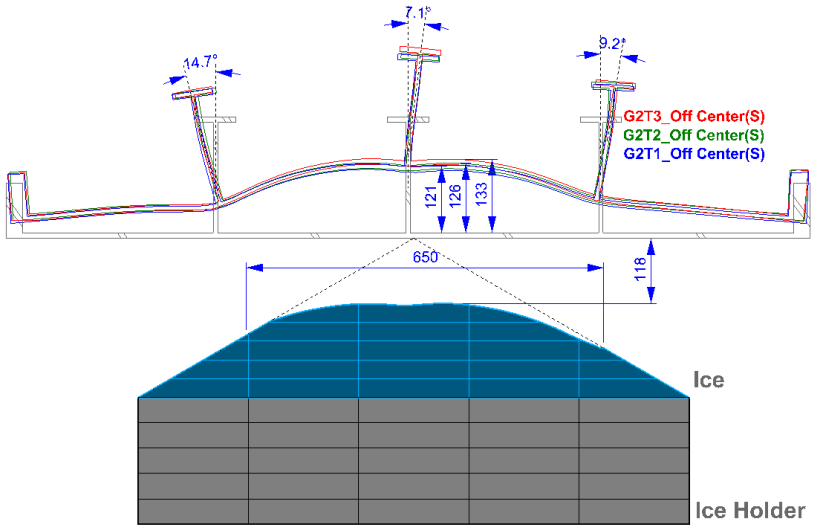

Figure 3-55: Consecutive section views at the right off-centre position

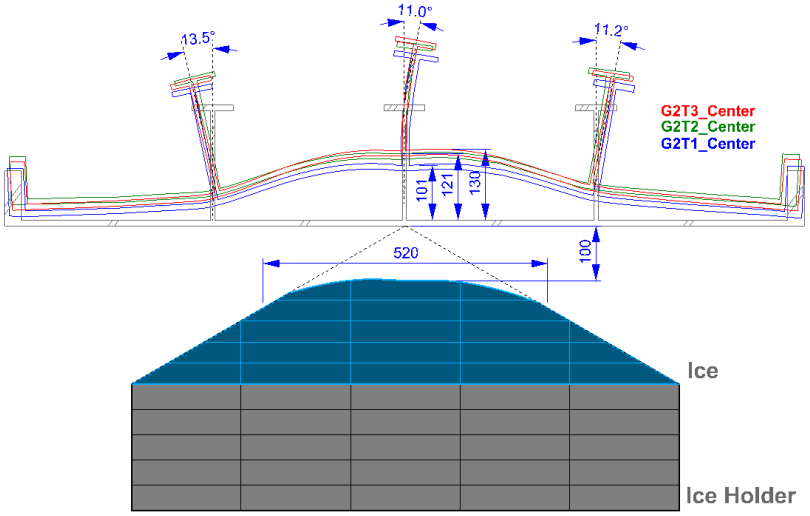

Figure 3-56: Consecutive section views at the midspan

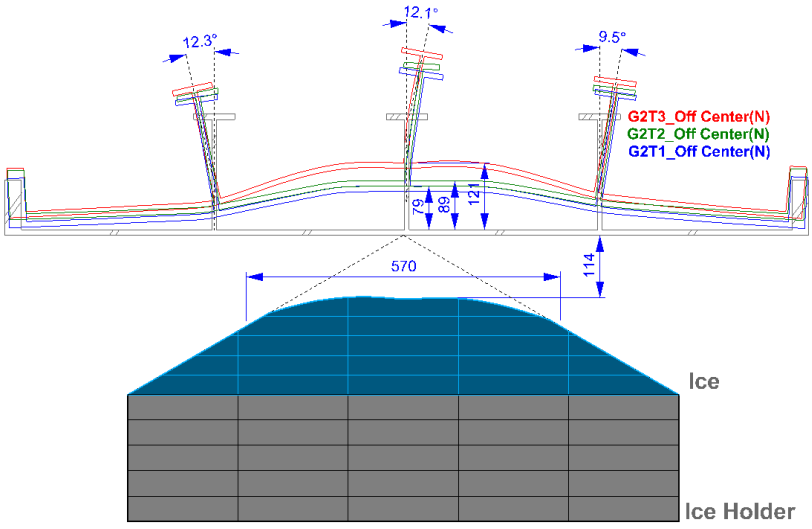

Figure 3-57: Consecutive section views at the left off-centre position

3.5 Discussions of Grillage #1 and #2

3.5.1 G1T1 and G2T1 (Comparison of different initial loading positions)

Figure 3-58 shows the comparison between G1T1 and G2T1. According to the IACS Polar Rules, the symmetric and asymmetric limit loads of the stiffener are 503 kN and 500 kN, respectively. Both curves exceed the limit state without any instability behavior or noticeable permanent set.

The load-deflection curve of G2T1 is slightly stiffer than that of G1T1 as shown in the elastic portion in Figure 3-58 (52.0 kN/mm compared with 48.3 kN/mm). This can be attributed to the loading position. G2T1 loading position was slightly off centre and closer to the stringer than G1T1. The nearby restraint and shear-bending interaction is likely the reason for this difference. Unfortunately, the loading location was limited by the test apparatus and therefore the end-load case could not be fully investigated.

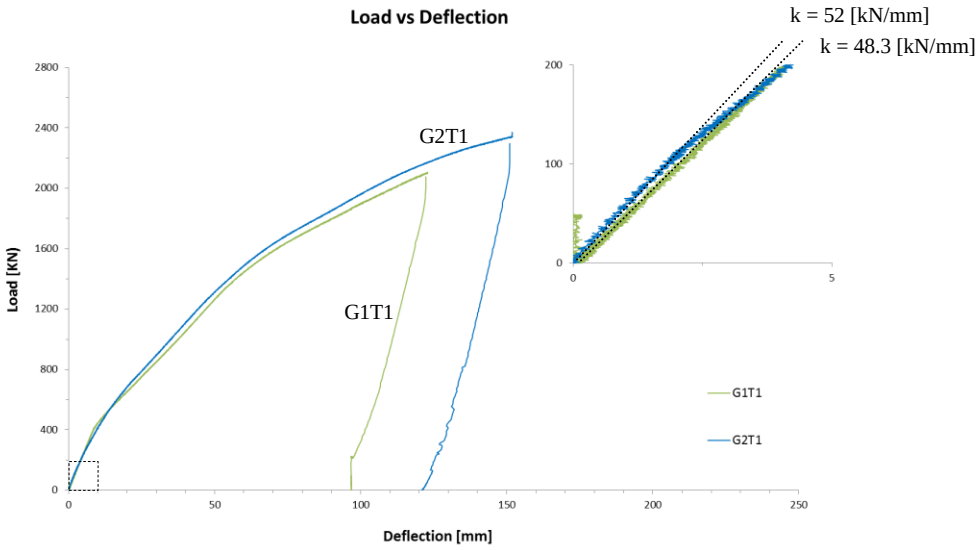

Figure 3-58: G2T1 in comparison with G1T1

3.5.2 G1T2 and G2T2 (Comparison of different prior loading positions)

Figure 3-59 describes load-deflection curves between G1T2 and G2T2. Both cases were the midspan loading cases but the prior loading positions were varied. The stiffness of the elastic portion of G1T2 (83.6 kN/mm) was greater than that of G2T2 (68 kN/mm). Although the position of loading did not show substantial differences on the stiffness during the previous tests (as described in the previous section), there was a dependence on prior loading position on the beneficial effect of strain hardening (added resistance to plastic deformation). The residual damage in the stiffener leads to further resistance to the deformation.

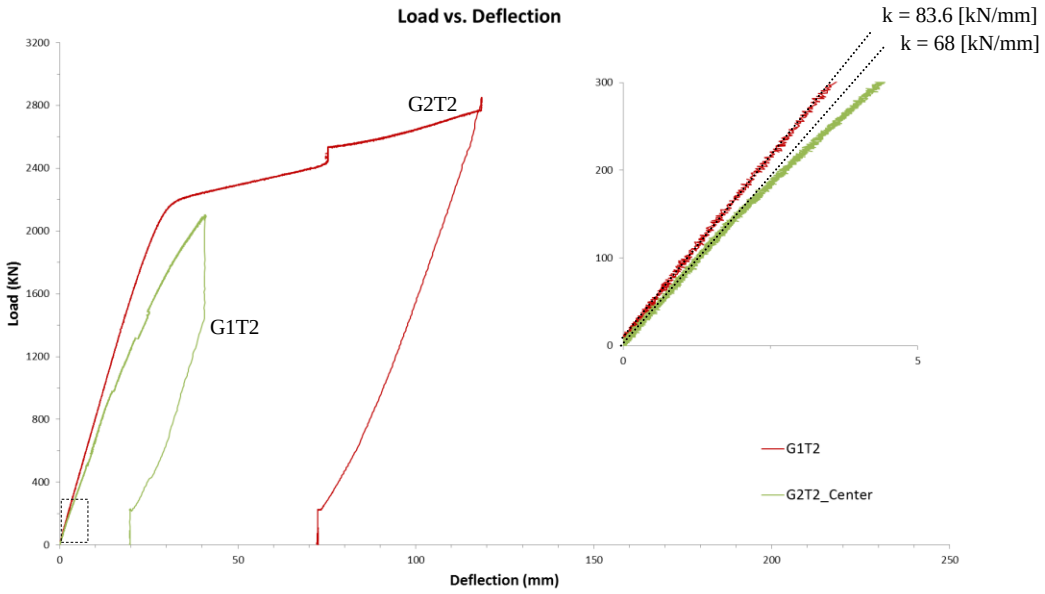

Figure 3-59: G1T2 in comparison with G2T2

3.5.3 G2T1 and G2T3 (Comparison of symmetric loading positions)

The position of loading of G2T3 is symmetric with the loading of G2T1 from the midspan of the grillage. The overall load of G2T1 against the grillage was approximately 2.3 MN at a deflection 120 mm. The load of G2T3 against the grillage with prior two damages was approximately 2.3 MN at a deflection 120 mm; however, the stiffness of the elastic portions of G2T3 (71 kN/mm) was 36 % greater than that of G2T1 (52 kN/mm). It can be referred that the residual stress from the previous damages in G2T3 leads to greater resistance to the deformation than G2T1.

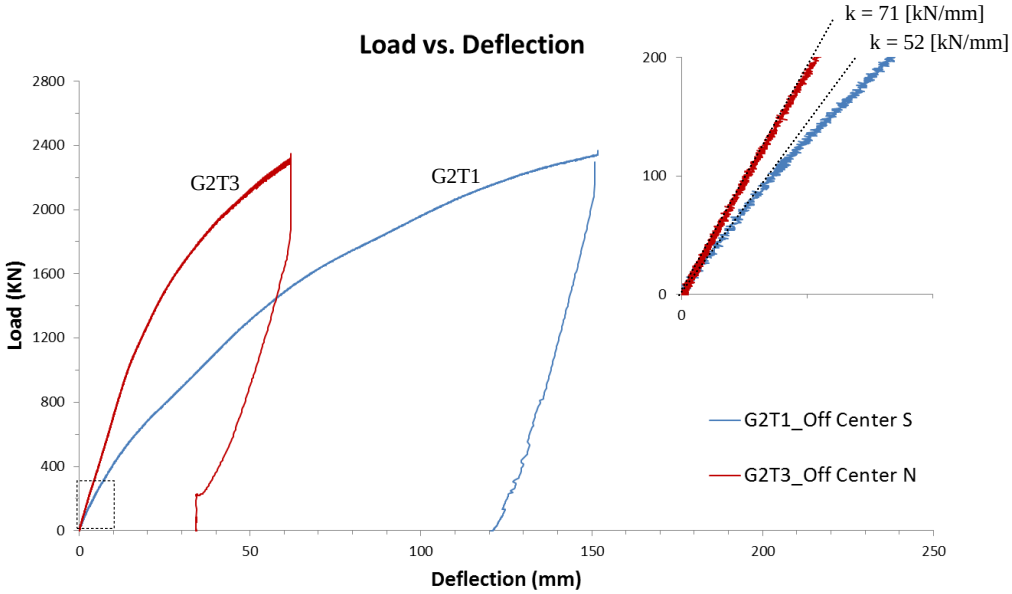

Figure 3-60: G2T1 in comparison with G2T3

3.6 Pressure-area Curves with Varying Calculation Methods for Contact Area

3.6.1 Pressure-area Interaction

Three methods were used to measure area and study the pressure-area relationships during the physical experiments.

1) Nominal contact area
2) Nominal contact area considering structural deformation
3) Direct measurement of the contact face

These areas were used to calculate the average pressure and characterize the process pressure-area distribution. The test apparatus was not instrumented to effectively measure the spatial pressure-area distribution during the experiments.

Figure 3-61 describes the ice crushing event of G1T1. The photos were taken by the inside camera. The first crack in the ice occurred at approximately 225 kN of loading. As the ice pushed into the structure, the overlap area between the ice and structure was increased. Both the ice and grillage were deformed together during the crushing event. The hydraulic ram speed was 0.5 mm/s which results in extremely slow strain rates typical of quasi-static loading. Therefore, no rapid spalling or fracturing events were observed throughout the experiments.

133 kN (30 kips)

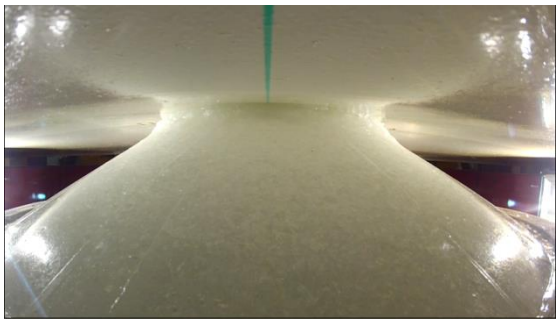

1,112 kN (250 kips)

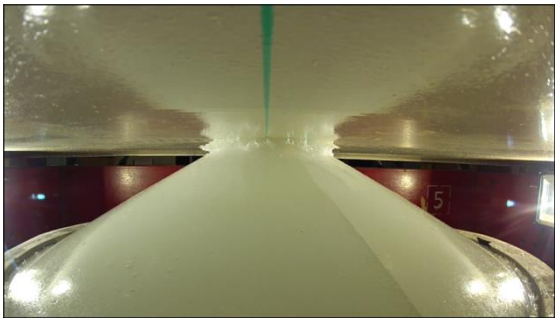

222 kN (50 kips): first crack in the ice

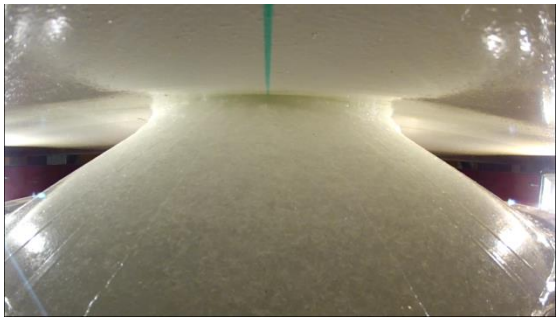

1,334 kN (300 kips)

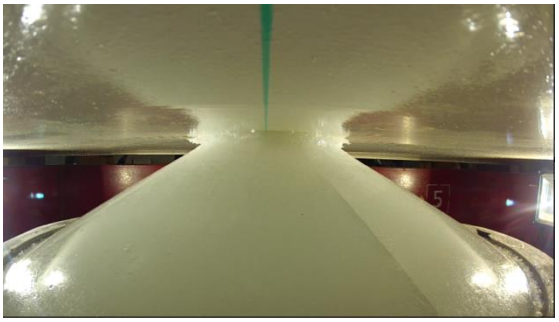

445 kN (100 kips)

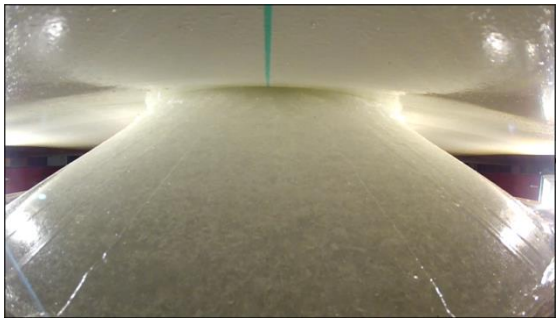

1,557 kN (350 kips)

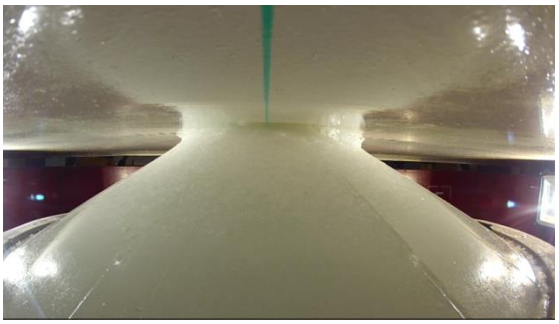

667 kN (150 kips)

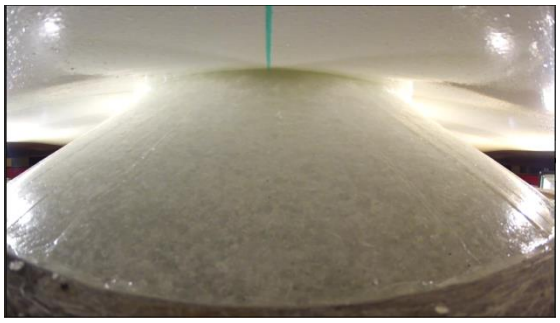

1,780 kN (400 kips)

Figure 3-61: Ice and structure interaction of G1T1

3.6.2 Nominal Area Calculation

The first method to define the process pressure-area relationships is based on the nominal area calculation. It is assumed that ice force will depend only on indentation depth. The maximum force occurs at the time of maximum penetration. The nominal contact area can be found from the ice/structure overlap geometry and the indentation (see Figure 3-62).

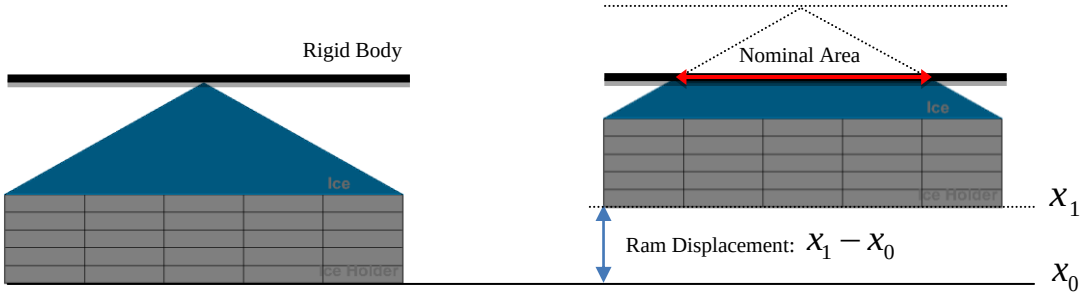

Figure 3-62: Schematic of the calculation method based on the nominal area

The ice sample angle is $\theta = 30°$

Initial position of the ram is x_0 and final position of the ram is x_1

Depth:

$$d = x_1 - x_0 \tag{3.1}$$

Radius at the depth:

$$r = \frac{d}{\tan(\theta)} \tag{3.2}$$

Nominal Area:

$$A_{nom,t} = \pi \left(\frac{d}{\tan(\theta)} \right)^2 \tag{3.3}$$

Therefore,

$$P_{avg,t} = \frac{F_t}{A_{nom,t}} \tag{3.4}$$

Figure 3-63 presents the pressure-area relationships for Grillage #1 based on the nominal contact area method. The results show a decreasing trend of pressure as the nominal contact area increases. The highest calculated pressures are approximate 10.5 MPa for Grillage #1 tests. It should be noted that these peak pressures are calculated over extremely small areas and are associated with low force measurements. They do not necessarily imply an extreme load.

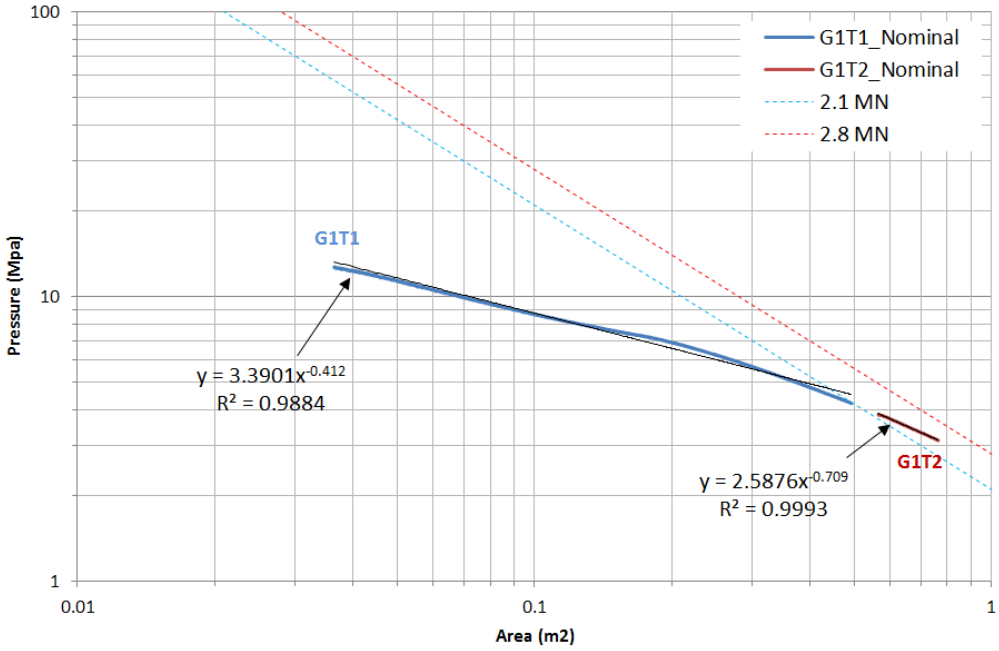

Figure 3-63: Nominal pressure-area curves of Grillage #1

Figure 3-64 presents the nominal pressure-area relationships for Grillage #2. The results show a decreasing trend of pressure as the nominal contact area increases in G2T1 and G2T3; however, an increasing trend was observed in G2T2. This is likely an effect of the over simplified nominal contact area calculation. The highest calculated pressures are approximate 10 ~ 11 MPa in both G2T2 and G2T3. Extremely small areas and low force measurements were filtered and not included in the curve. Exponential trendlines are fitted to the pressure-area data along with equations in the form of common pressure-area relationships [$P = P_o \cdot A^{ex}$]. The data are summarized in Table 3-2.

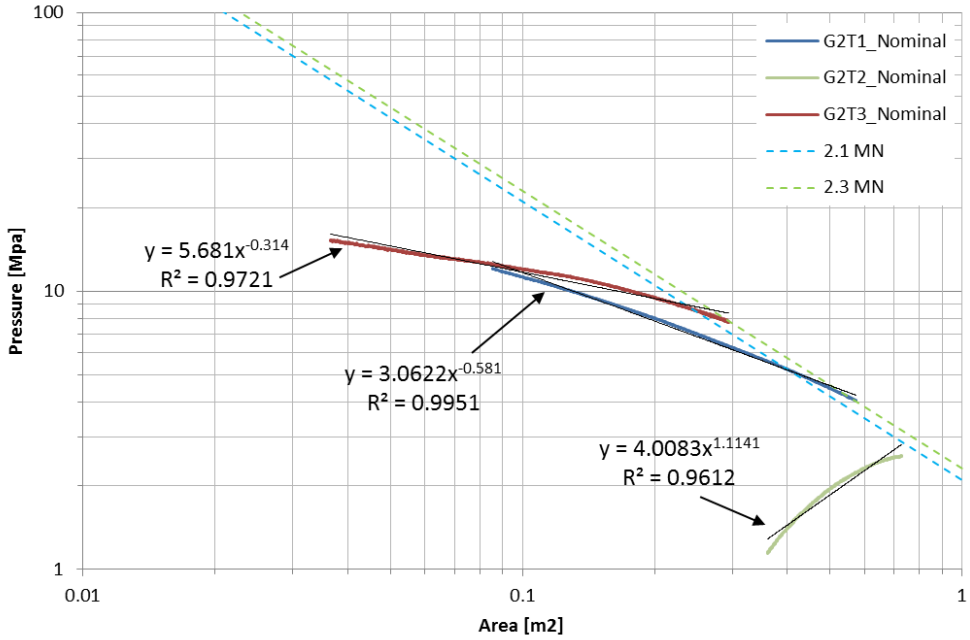

Figure 3-64: Nominal pressure-area curves of Grillage #2

3.6.3 Nominal Area Calculation Considering Structural Deformation

When a structure is not a perfectly rigid body, structural deformation should be considered to calculate the nominal area by deducting the structural deformation from the indentation depth since the nominal area is based on the penetration depth. Related equations are provided in this section to explain the nominal area considering structural deformation method (see Figure 3-65).

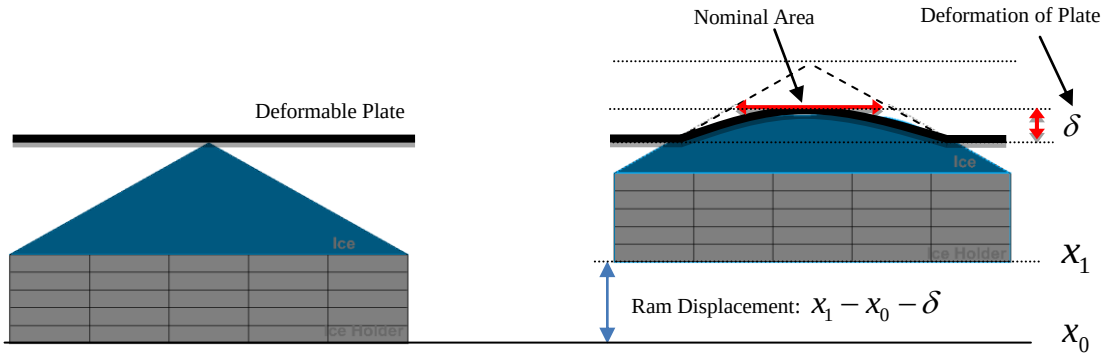

Figure 3-65: Schematic of nominal area considering structural deformation

The ice sample angle is $\theta = 30°$

Initial position of the ram is x_0 and final position of the ram is x_1

The structural deformation is δ

Penetration depth can be found by deducting the δ from the ram displacement.

$$d = x_1 - x_0 - \delta \tag{3.5}$$

Where, $\delta =$ Deformation of the plate from LVDT

Radius at the depth:

$$r = \frac{d}{\tan(\theta)} \tag{3.6}$$

Nominal Area:

$$A_{nom,t} = \pi \left(\frac{d}{\tan(\theta)} \right)^2 \tag{3.7}$$

Therefore,

$$P_{avg,t} = \frac{F_t}{A_{nom,t}} \tag{3.8}$$

The relationship between the ram displacement and the structural deformation from the LVDT are described in Figure 3-66. Using the nominal area considering structural deformation, the process pressure-area relationship can be found.

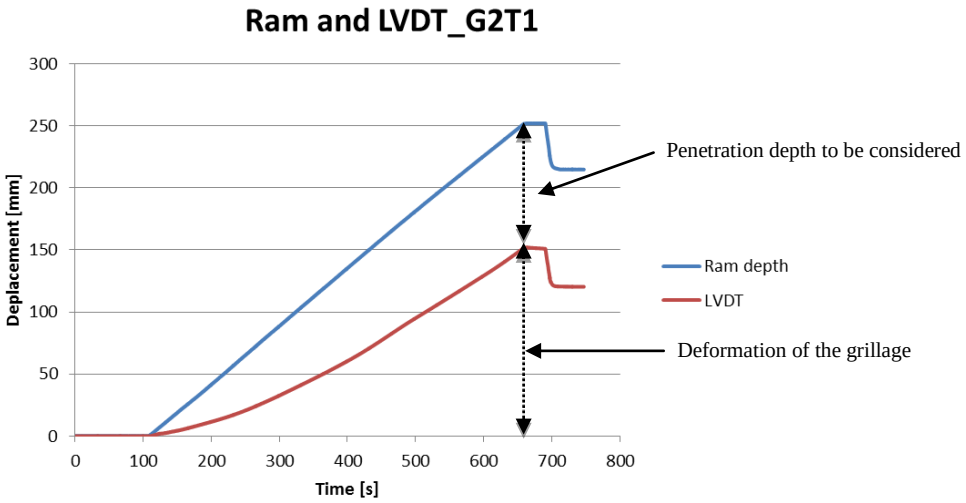

Figure 3-66: Ram stroke displacement and structural deformation of G2T1

Figure 3-67 presents the nominal pressure-area relationship considering the structural deformation of Grillage #1. The results show relatively constant trend of pressure as the nominal contact area increases. The calculated pressures are approximately 11 MPa in the all area region. The range of the area was reduced since the overlap area is necessarily less than the nominal area in the rigid body.

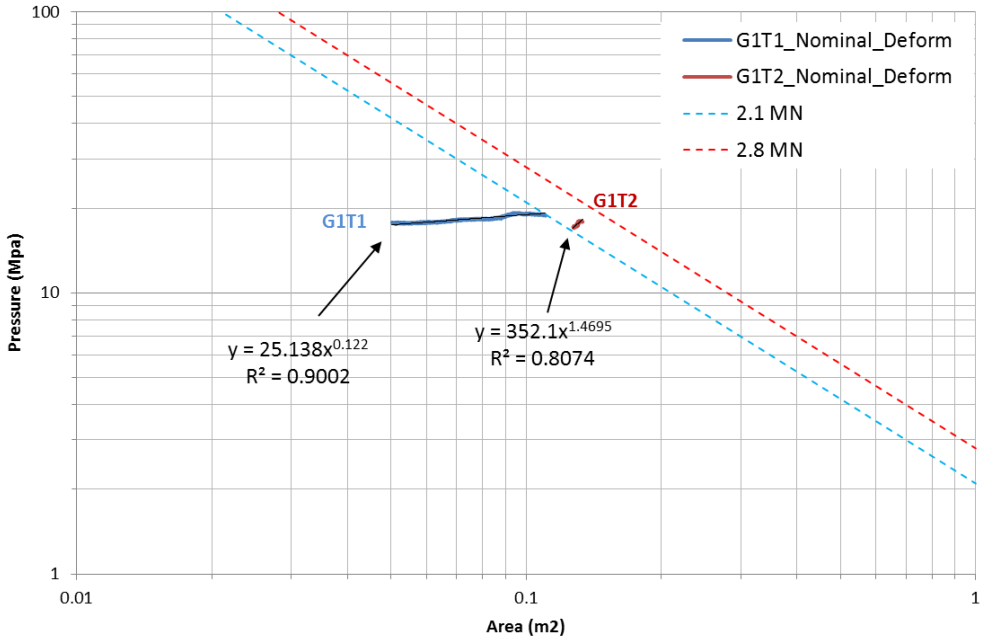

Figure 3-67: Nominal pressure-area curves considering deformation of Grillage #1

Figure 3-68 presents the pressure-area relationship for Grillage #2. The results show diverse trends in which pressure decreases, remains constant or increases as the nominal contact area increases in the three tests. The pressure in G2T1 and G2T3 are relatively constant between 10 ~ 12 MPa in the entire area ranges. On the other hand, the pressure in G2T2 was also observed an increasing trend as the previous trend in Figure 3-64. Exponential trendlines are fitted to the pressure-area data along with equations in the form of common pressure-area relationships [$P = P_o \cdot A^{ex}$]. The data are summarized in Table 3-2.

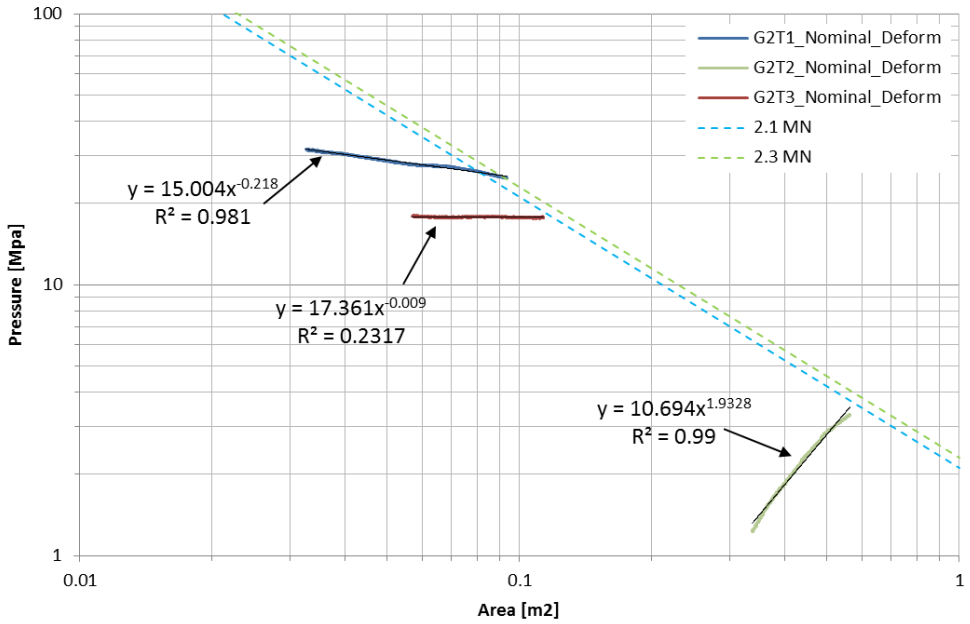

Figure 3-68: Nominal pressure-area curves considering deformation of Grillage #2

3.6.4 Direct Measurement of the Contact Face

The third method of contact area estimation is based on direct measurements after the completion of each test. The contact faces between ice and the grillage were measured manually (see Figure 3-69). The contact face was relatively flat since this experiment was crushed at extremely slow speed and no spalling or fracturing events were observed (see Figures 3-70 and 3-71). The disadvantage of this method is that area measurements can only be taken manually after the test instead of continuous area calculations based on the penetration measurements.

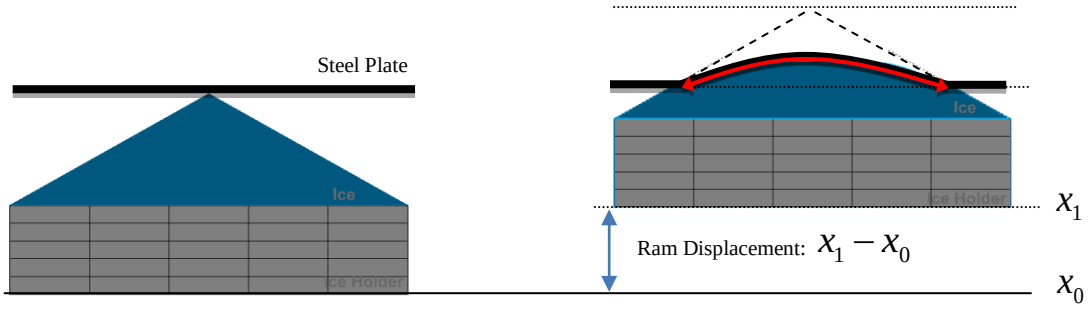

Figure 3-69: Schematic of the method based on direct measurements of the contact face

$$P_{avg} = \frac{F_t}{A_{measurement}} \qquad \textbf{(3.9)}$$

Average pressure versus direct measured contact areas using equation (3.9) are plotted in Figure 3-72. All points fall within the force range of 2.1 ~ 2.8 MN since this data is limited by a level of maximum force. The pressure-area data are presented in Table 3-3.

Figure 3-70: Ice sample after unloading

Figure 3-71: Measurement of the diameter

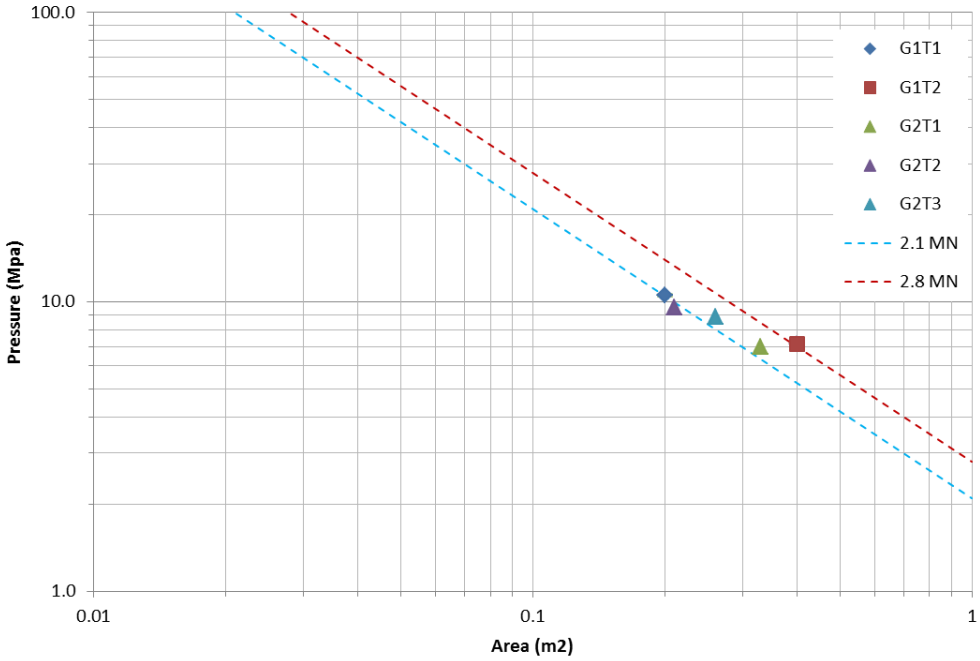

Figure 3-72: Pressure-area plot of direct measurements of the contact face

3.6.5 Discussions

In Figure 3-73, the pressure-area results of the physical experiments are compared with an assemblage of Polar Sea full scale data sets prepared by Daley (2004). The comparison demonstrates that these experiments fall within the general envelop of existing, particularly for smaller contact areas. However, it also shows the uncertainty and sensitivity of measurement methods in the use of pressure-area to describe ice loads on deforming structures.

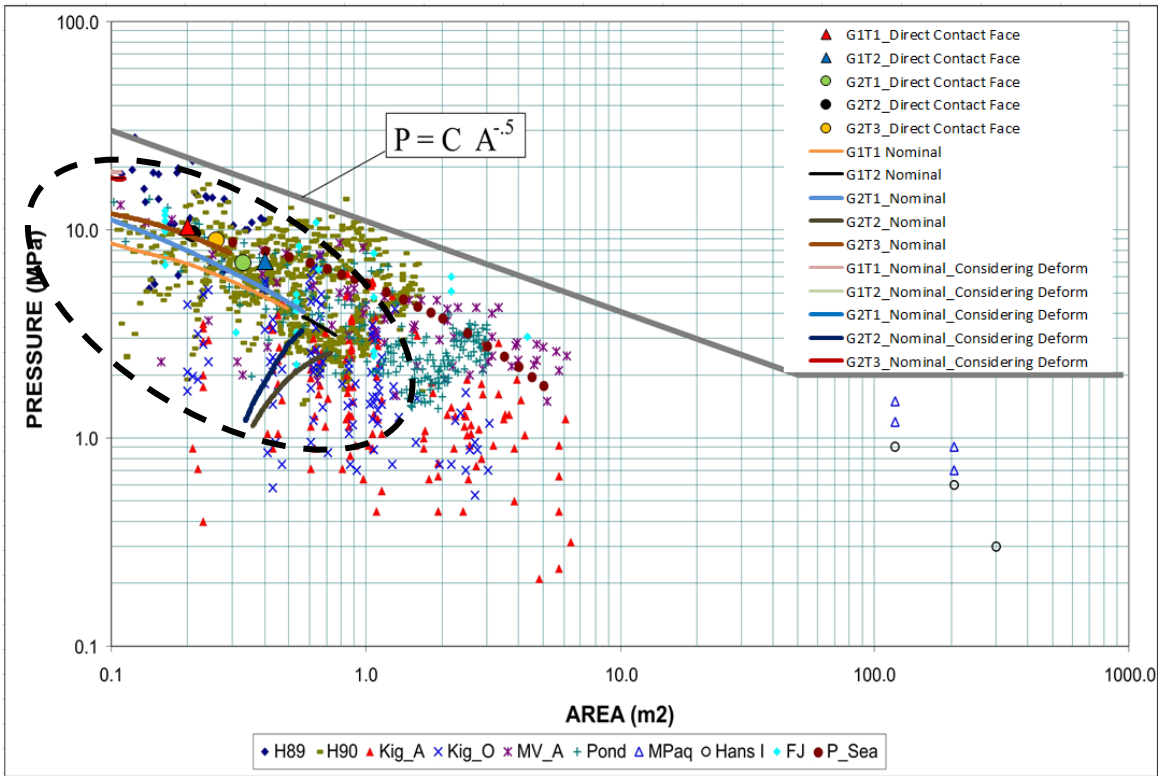

Figure 3-73: Comparison with pressure-area data of the Polar Sea (Daley, 2004)

Table 3-2: Summary of the pressure-area curves

	Average Pressure at $1m^2$	Exponent Term	Correlation Coefficient (R^2)	Loading Position
G1T1_Nominal	3.3901	-0.412	0.9884	Centre
G1T2_Nominal	2.5876	-0.709	0.9993	Centre
G2T1_Nominal	3.0622	-0.581	0.9951	Off-Centre
G2T2_Nominal	4.0083	1.1141	0.9612	Centre
G2T3_Nominal	5.681	-0.314	0.9721	Off-Centre
G1T1_Nom_Deform	25.138	0.122	0.9002	Centre
G1T2_Nom_Deform	352.1	1.4695	0.8074	Centre
G2T1_Nom_Deform	15.004	-0.218	0.981	Off-Centre
G2T2_Nom_Deform	10.694	1.9328	0.99	Centre
G2T3_Nom_Deform	17.361	-0.009	0.2317	Off-Centre

Table 3-3: Summary of direct measurements of the contact face

	Force (kN)	Displacement (mm)	Measured Contact Area (m^2)	Average Pressure (MPa)
G1T1	2,100	120	0.2	10.28
G1T2	2,800	215	0.4	7.2
G2T1	2,313	150	0.33	7
G2T2	2,100	43	0.22	9.5
G2T3	2,313	59	0.26	9.1

3.7 Uniaxial Material Tensile Tests

Ten uniaxial material tensile tests were conducted to determine the material properties of the steel used in the fabrication of the large grillage structure. The specimens were cut from the end part of Grillage #2 in order to minimize the effect of permanent deformation and residual stresses of the specimens (see Figure 3-75). Figure 3-76 shows Instron™ 5585H series tensile tester which maximum capacity is 250 kN (56,250 lbf). The yield stress, Young's modulus, engineering ultimate tensile stresses and engineering failure strains are summarized in Table 3-4.

Engineering strain is based on the initial gage length. However, as the material is strained, each incremental change in length acts over the entire length of the specimen which becomes progressively longer as the test continues. To convert from engineering to true strain, equation (3.10) can be used. The engineering stress is based on the assumption of constant cross-sectional area. However, in reality the specimen is elongated while maintaining constant volume, therefore the cross-sectional area decreases. To take this into account, engineering stress must be converted to true stress using equation (3.11). The average data was calculated from the overall results. However, the lowest yield stress of specimen #6 was used to convert from engineering stress-strain to true stress-strain in order to obtain conservative values (see Table 3-5). The engineering and true stress-strain curves are illustrated in Figure 3-74.

Table 3-4: Summary of the uniaxial material tensile tests

Specimen	Engineering yield stress [MPa]	Young's modulus [GPa]	Engineering ultimate tensile stress [MPa]	Engineering failure strain[mm/mm]
1	410	200	490	0.254
2	411	186	488	0.221
3	400	167	477	0.241
4	407	183	477	0.232
5	405	182	482	0.249
6	404	202	477	0.246
7	408	204	474	0.249
8	410	205	480	0.247
9	405	178	481	0.253
10	413	206	488	0.231
Average	407.3	191.3	481.4	0.242

$$\varepsilon_t \approx \ln(1 + \varepsilon_e) \quad \textbf{(3.10)}$$

$$\sigma_t \approx \sigma_e(1 + \varepsilon_e) \quad \textbf{(3.11)}$$

Where, σ_e is engineering stress

ε_e is engineering strain

σ_t is true stress

ε_t is true strain

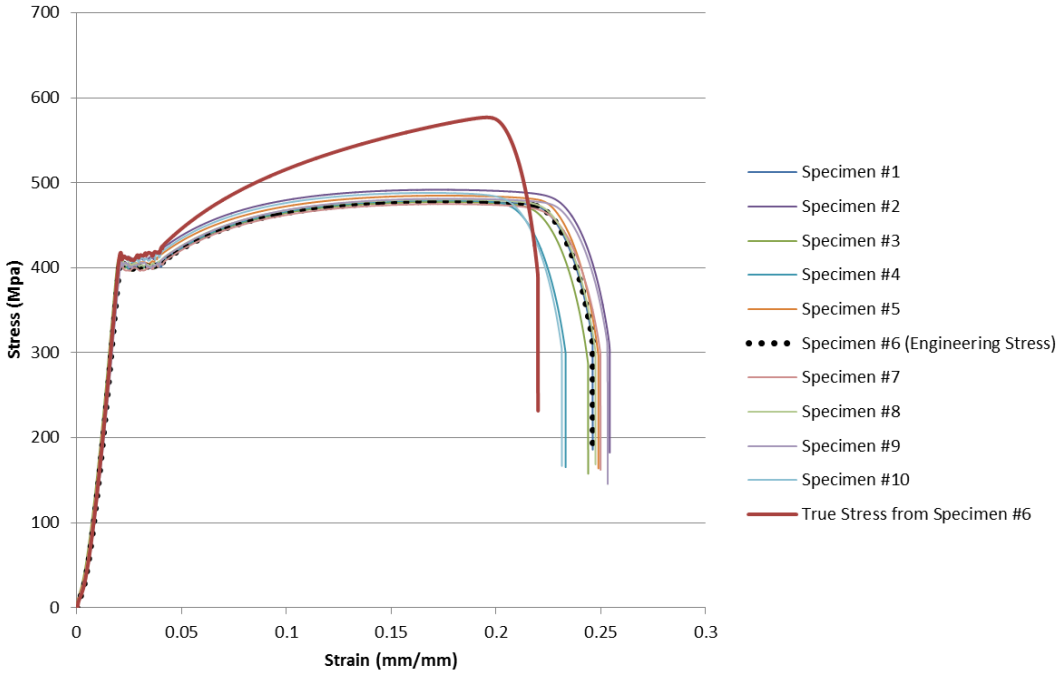

Figure 3-74: Engineering stress-strain and true stress-strain curves

However, the yield stress of the steel show relatively higher value than typical steel for ship structures (see Table 3-5). Typical steel property lies within the range 235 MPa to 355 MPa depending on the grade and type.

Table 3-5: True stress-strain properties

Density [kg/m^3]	Young's modulus [GPa]	Poisson's ratio	Yield stress [MPa]	Tangent modulus [MPa]
7850	202	0.3	410	950

Figure 3-75: The end part of the grillage where the material test specimens were taken

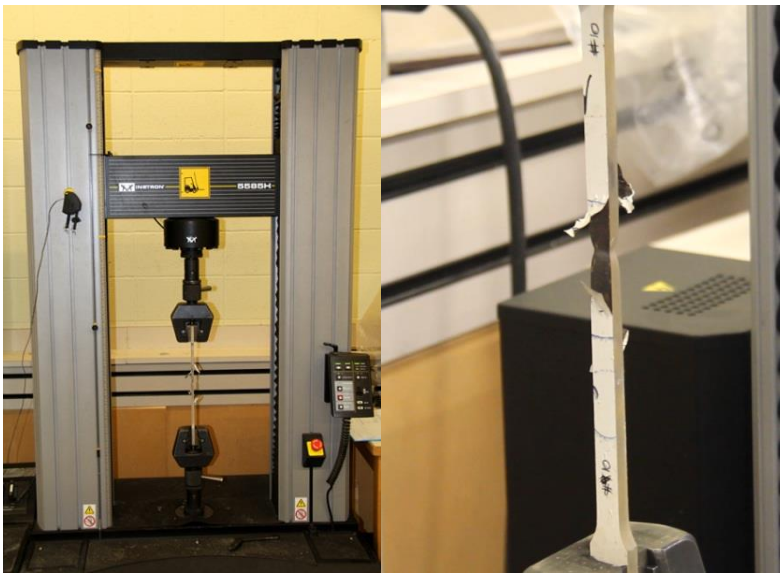

Figure 3-76: Material test machine (left) and necking at a specimen (right)

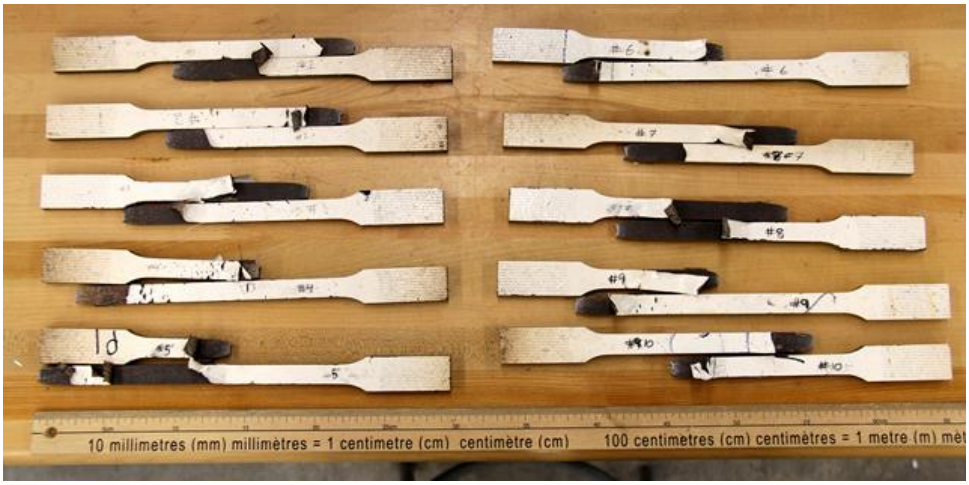

Figure 3-77: Completed specimens

3.8 Conclusion

The scantlings of the grillage used in the experiments are known. Therefore, the shear area and plastic section modulus were calculated and then compared with the required values from the UR equations in order to check compliance of the requirements. Two limit states are considered; the pressure from a central load causing three-hinge collapse and the pressure from an asymmetric load causing combined shear and bending collapse. The subsequent forces for a central load causing three-hinge collapse and an asymmetric load causing combined shear and bending collapse were 503 kN and 500 kN respectively.

Grillage #1 tests demonstrated significant overload capacity of the grillage when subject to ice loads, with deflections up to 215 mm at the peak loading condition. The maximum load applied was 2.8 MN which is greater than 5 times the design load. Also the stiffness of the elastic portions of the load-deflection curves in the second test (83.6 kN/mm) was about 73 % higher than the first test (48.3 kN/mm). Thus, these experimental results suggest that the local deformations (up to 11 % of the frame span) do not necessarily compromise the overall strength of the large grillage. In fact the grillage actually gains stiffness and exhibits higher load-carrying capacity when there is prior deformation.

Grillage #2 load cases were carried out sequentially with fresh ice samples applied to the deformed grillage from the previous cases. It was observed that the stiffness of the elastic portions of the load-deflection curves in the second and third tests were higher than the first test. Thus, these experiments suggest that prior plastic deformations at nearby locations do not necessarily compromise the overall strength of the grillage. The maximum load applied was 2.3 MN which is greater than 4 times the design load. The actual ultimate load was not reached.

Three methods were used to calculate the average pressure and characterize the process pressure-area distribution. The pressure-area relationships show the uncertainty and sensitivity of measurement methods in the use of pressure-area to describe ice loads on deforming structures.

Ten uniaxial material tensile tests were conducted to determine the material properties of the steel used in the fabrication of the large grillage structure. The average data was calculated from the overall results. However, the lowest yield stress of specimen #6 was used to convert from engineering stress-strain to true stress-strain in order to obtain conservative values. However, the yield stress of the steel show relatively higher value than typical steel for ship structures. Typical steel property lies within the range 235 MPa to 355 MPa depending on the grade and type.

4 NON-LINEAR FINITE ELEMENT ANALYSIS

4.1 Introduction

The finite element method has become a powerful tool for numerical analysis of a wide range of engineering problems along with advancements in computer technology and Computer-Aided Design (CAD) tools. In this study, non-linear finite element analysis using ANSYS® was used to simulate large deflections and plastic deformations observed during experiments. Nonlinearities, boundary conditions, loading scenarios, and element mesh sizes were appropriately considered in the simulation model then validated with the experimental results. The load-deflection curves and deformation shapes measured by the MicroScribe® were used to validate the numerical results.

4.2 Structural Idealization

4.2.1 Structural Modeling

The large grillage model is a full-scale representation of the side shell of a transversely framed 10,000 ton Ice Class PC6 midbody ice belt arrangement of an ice-strengthened ship. In this study, the entire structural grillage was modeled except for the bolt connections which were treated as boundary conditions (see Figure 4-1). Based on the experimental results as mentioned before, large deflection of the grillage was expected; therefore, the initial imperfection was not considered in the simulations. The ice load was applied as a uniform pressure distribution over contact areas measured from the experiments.

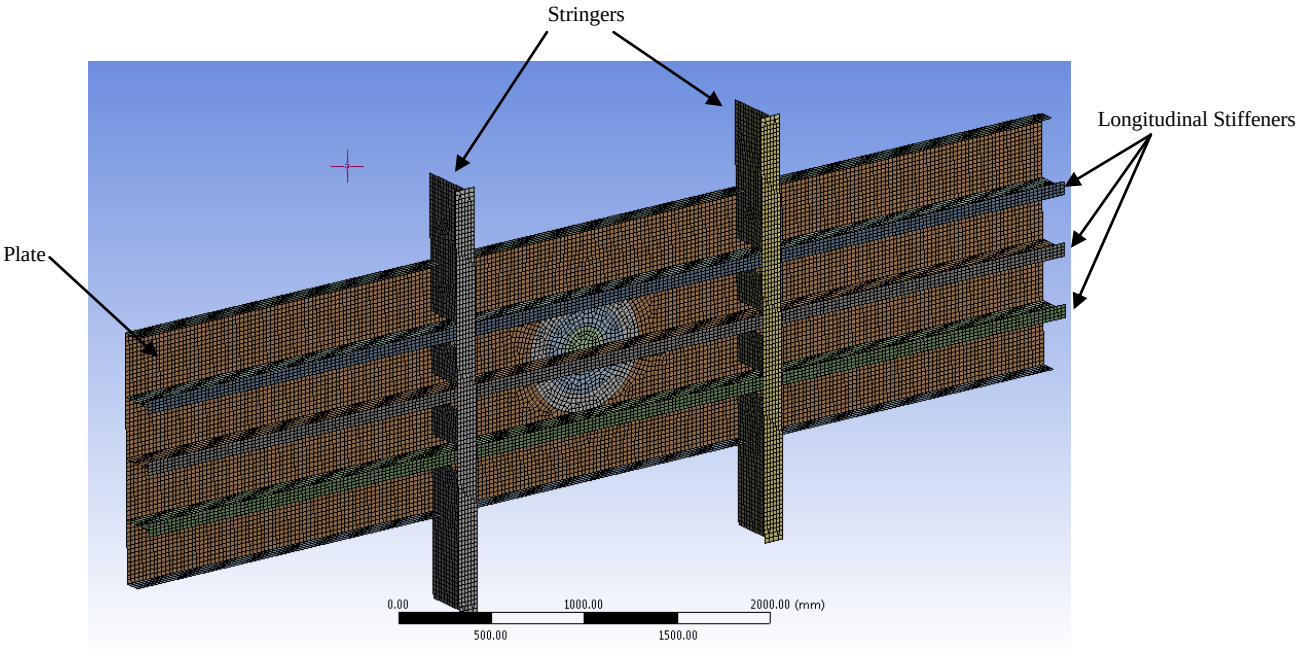

Figure 4-1: Extent of the structural model

4.2.2 Element Type and Meshing

Abraham (2008) concluded that both shell and solid elements are suitable element types for estimating capacity of a frame. In this study, the shell elements were chosen since the shell elements are suitable to present rotational deformation such as buckling of stiffeners. In addition, shell elements are more computationally efficient and take less time to solve in non-linear finite analysis. Thus, both plate and stiffeners were modelled using SHELL181 elements which are suitable for non-linear finite element analysis. Due to the use of nonlinear materials, full integration using five points of integration through the thickness of the shell elements was used. Each element has four-nodes, each with six degrees of freedom: translations in the x, y, and z directions, and rotations about the x, y, and z-axes (see Figure 4-2).

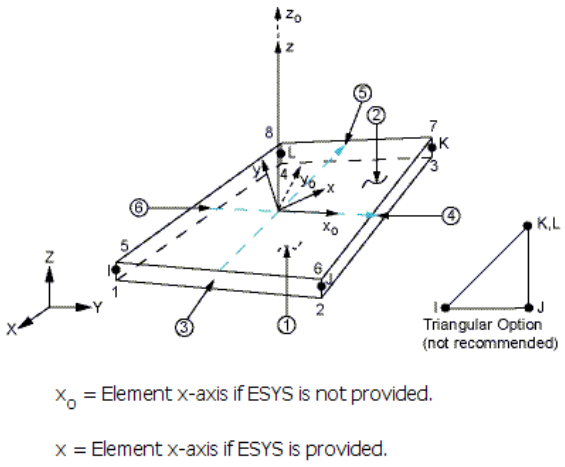

Figure 4-2: SHELL181 model (ANSYS)

In accordance with ABS guide notes on "Nonlinear finite element analysis of side structures subject to ice loads" (ABS, 2004), the web of a longitudinal should be divided into at least three elements. Therefore, the web of the stiffeners was divided into eight elements. And the flange of the stiffener was divided into four elements in order to

present the deformation of the flange. Ultimately, a 25 mm fine mesh size was applied in this simulation model.

4.3 Material Property Model

A bilinear isotropic elasto-plastic model was adopted for the material property to simplify the non-linear relationship of stress-strain in the plastic region (see Figure 4-3). Table 4-1 shows the material properties used for the finite element analysis. Young's modulus is 200 GPa; yield stress is 355 MPa, and post yield modulus is 2,000 MPa. The post yield modulus is the slope from yield point to the end in the bilinear model and it represents the rate of strain-hardening as strain increasing.

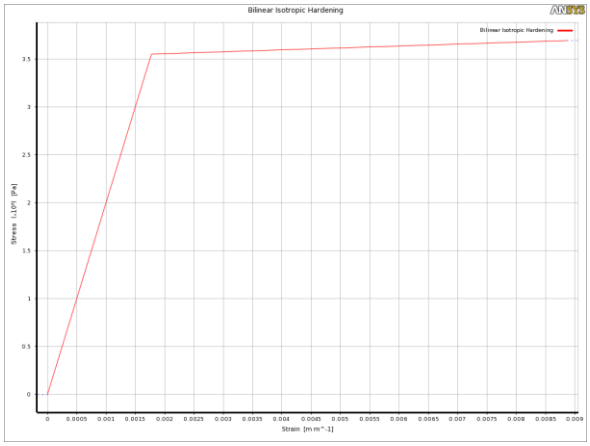

Figure 4-3: Bilinear elasto-plastic stress-strain curve

Table 4-1: Material parameters

Density [Kg/m3]	Young's modulus [GPa]	Poisson's ratio	Yield stress [MPa]	Tangent modulus [MPa]
7850	200	0.3	355	2,000

4.4 Boundary Conditions

Fixed boundary conditions were applied at the location of the bolt connections of the grillage (see Figure 4-4). Since the boundaries are far away from the point of application of load, it is assumed that the boundary conditions have no significant effect on response of the frame. Thus, both sides and longitudinal boundary conditions in this grillage configuration are presumed to be simplified representations of the actual boundary conditions in the physical experiments.

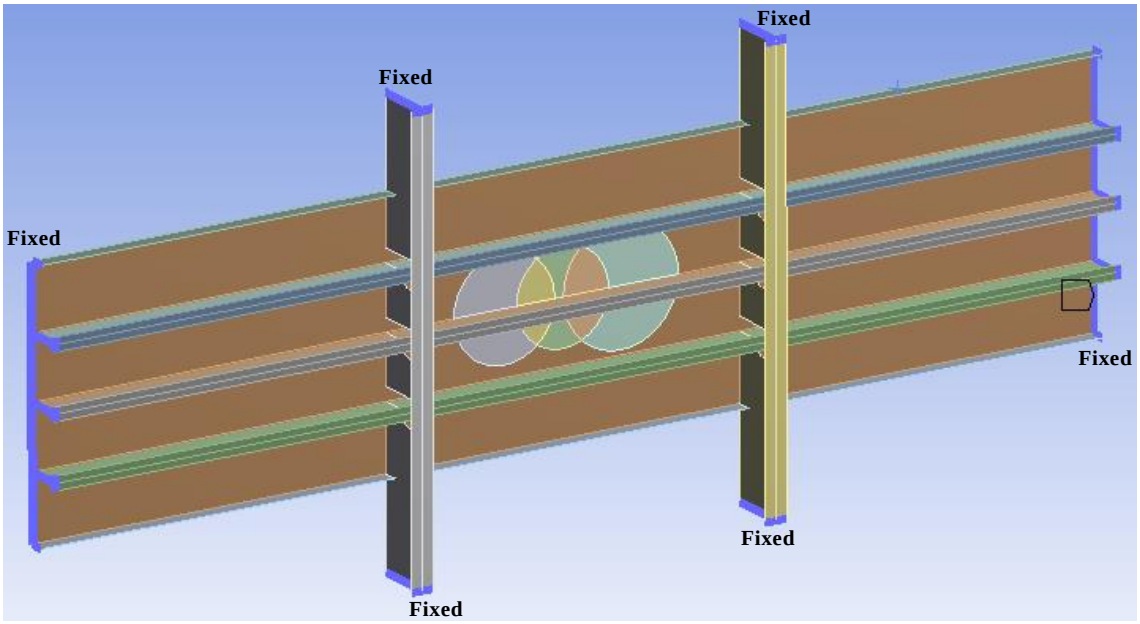

Figure 4-4: Boundary conditions

4.5 Loading

The ice pressure was applied to the FE model as uniform pressure distributions (average pressure) over defined circular contact areas. The contact forces and areas between ice and the grillage were measured manually after each test (see chapter 3.6.4). The average pressure was calculated using these directly measured contact areas and forces. The applied pressure distribution was determined based on this average pressure and the measured contact area.

Approximately 10.28 MPa was used for the inner area (0.2 m^2) and 7.2 MPa was used for the outer contact area (0.4 m^2) in the Grillage #1 FE analysis (see Figures 4-5 and 4-6).

A total of six sequential loading and unloading steps and three different locations were considered in the Grillage #2 FE analysis. The first and second steps were loading and unloading of 7.0 MPa at the left off-centre for G2T1. The third and fourth steps were loading and unloading at the centre of 9.5 MPa for G2T2. The fifth and sixth steps were loading and unloading of 9.12 MPa at the right off-centre for G2T3 (see Figures 4-7 to 4-9).

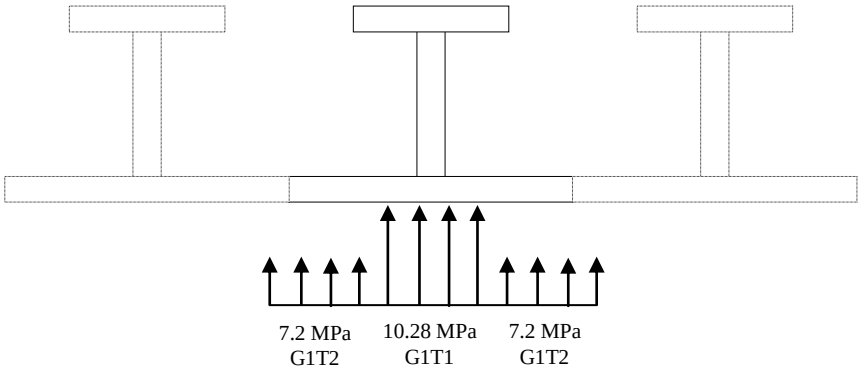

Figure 4-5: Loading scheme in Grillage #1

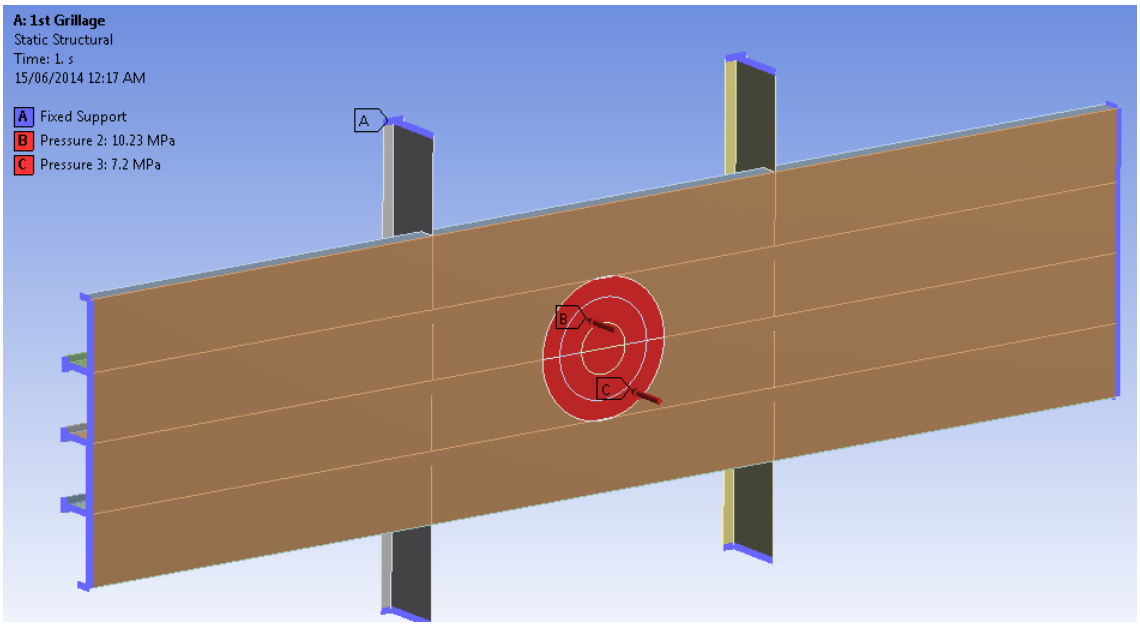

Figure 4-6: Loading conditions of Grillage #1

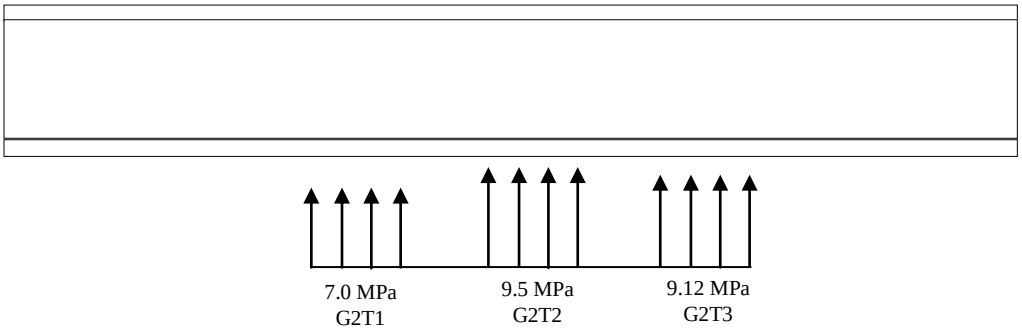

Figure 4-7: Loading scheme in Grillage #2

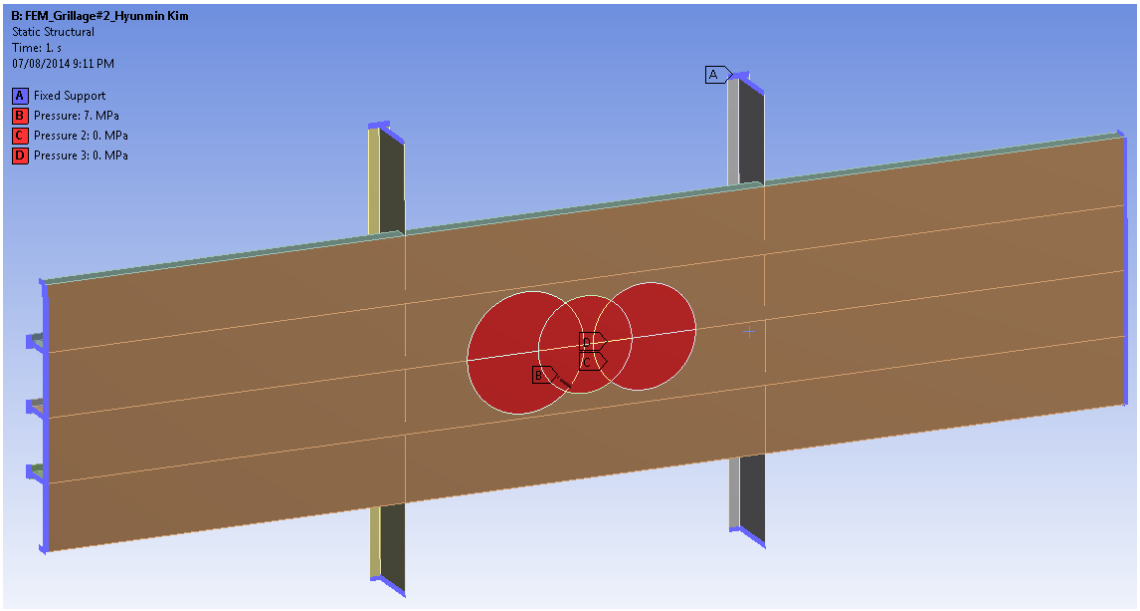

Figure 4-8: Loading conditions of Grillage #2

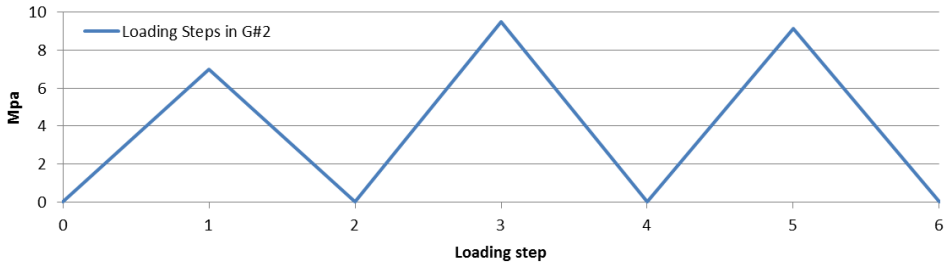

Figure 4-9: Loading steps in Grillage #2

4.6 FE Analysis Results

The calculated load-deflection curves and the cross section views of deformed shape of the FE analysis were compared with the results of the experiments.

4.6.1 Grillage #1

A comparison of the experiments and FE analysis of load-deflection curves are presented in Figure 4-10. The curve shows excellent agreement with the experimental results of Grillage #1 and G2T1 test. The stiffness of the elastic portions of the load-deflection curves in the FEM [44.3 kN/mm] is similar to those of G1T1 [48.3 kN/mm] and G2T1 [52 kN/mm].

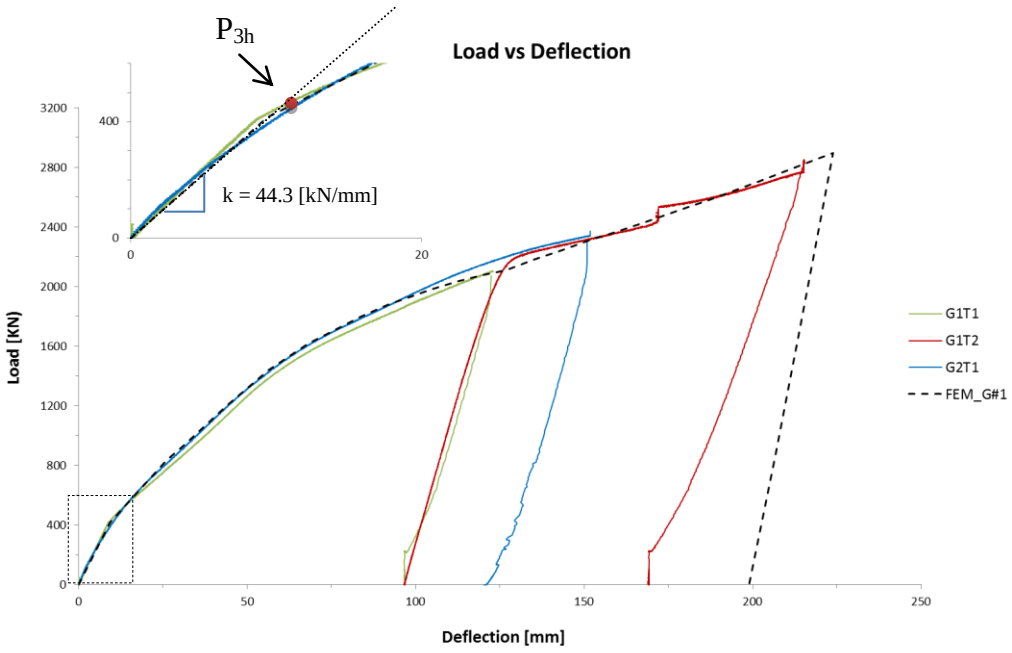

Figure 4-10: FEM load-deflection curves in comparison with the experimental results

Figure 4-11 presents the comparison of cross section views of deformed shape between experimental results and FE analysis. The result of analysis also shows that the deformations are strong agreement with experimental results. Even at the final load step, the FE analysis quite accurately captures the progressive folding over of the central stiffener.

The vertical deflection and equivalent plastic strain of the each analysis are shown in Figures 4-12 to 4-15.

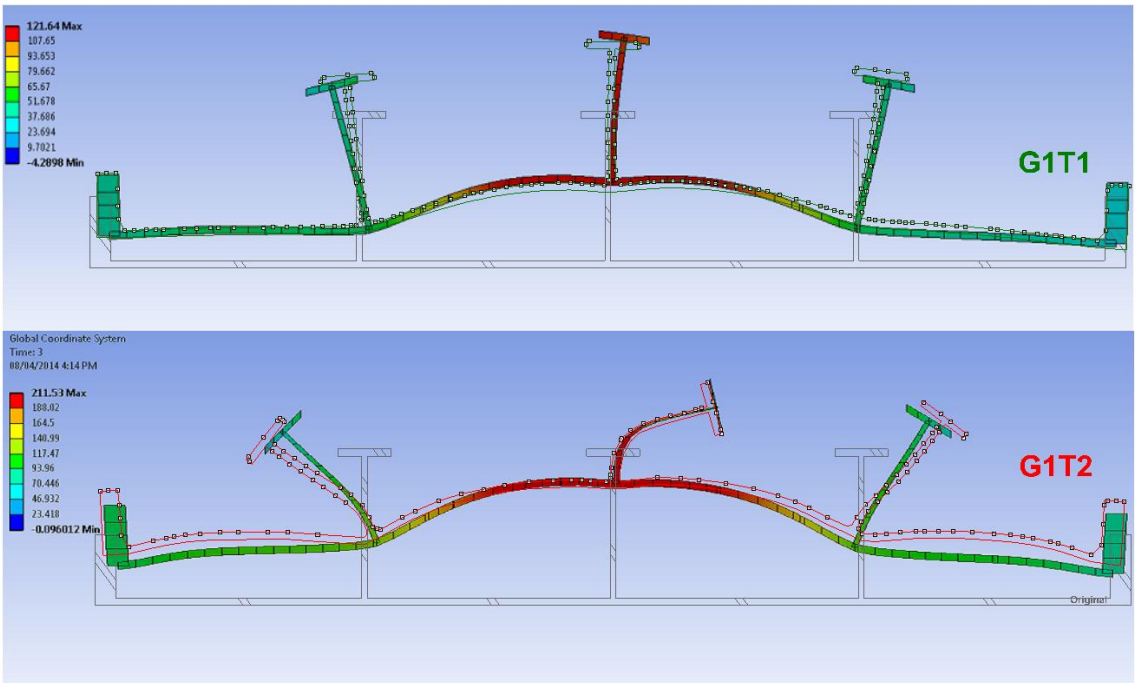

Figure 4-11: Cross section views of deformation between experiments and FEA of Grillage #1

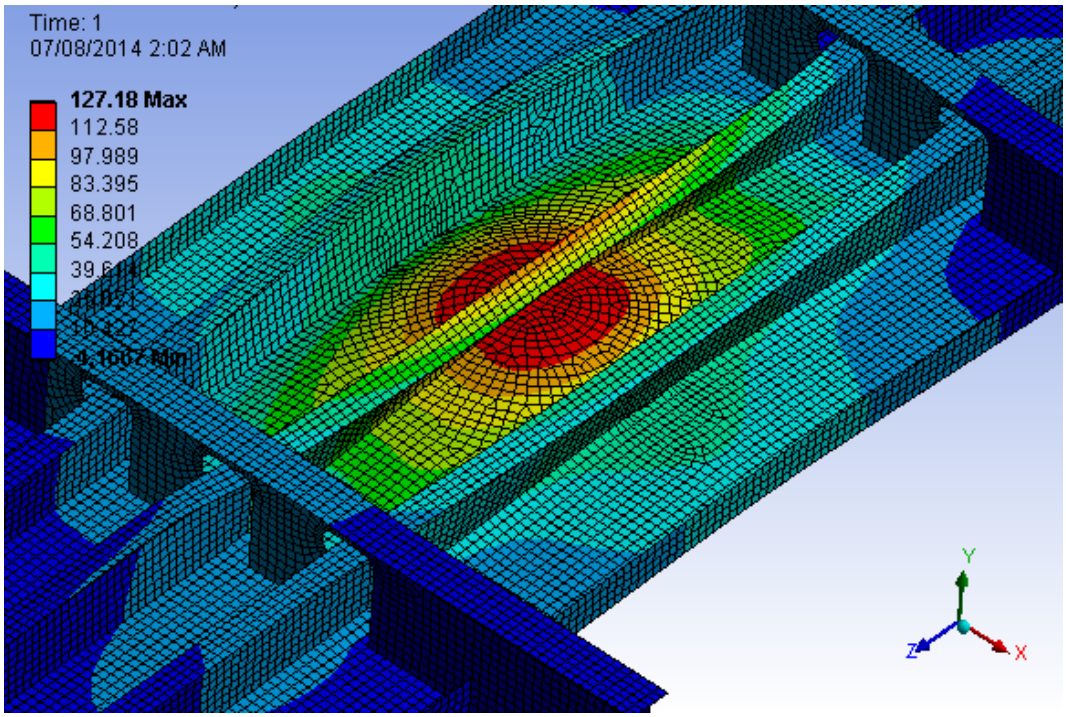

Figure 4-12: Vertical deflection of G1T1 FEM at 2.1 MN

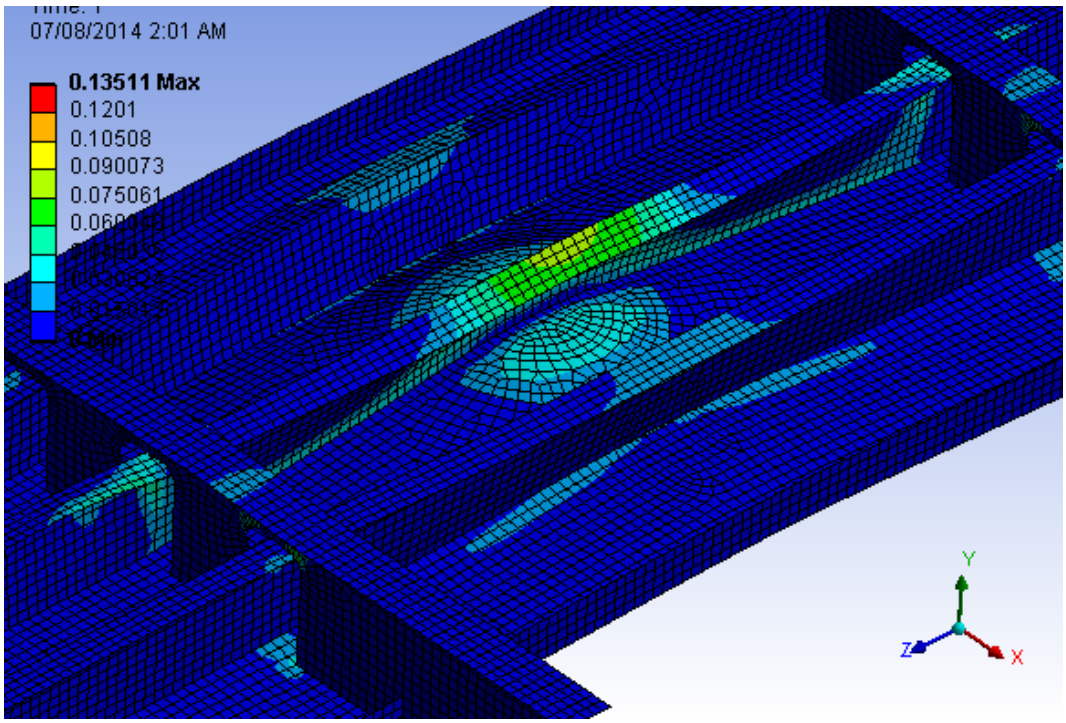

Figure 4-13: Equivalent plastic strain of G1T1 FEM at 2.1 MN

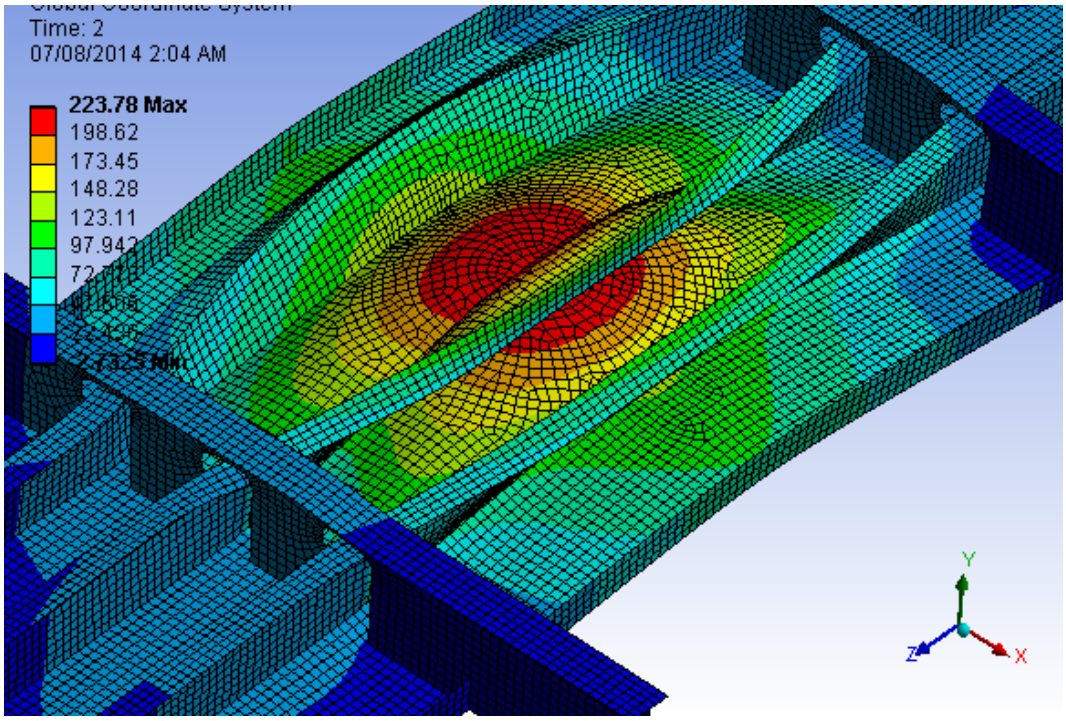

Figure 4-14: Vertical deflection of G1T2 FEM at 2.8 MN

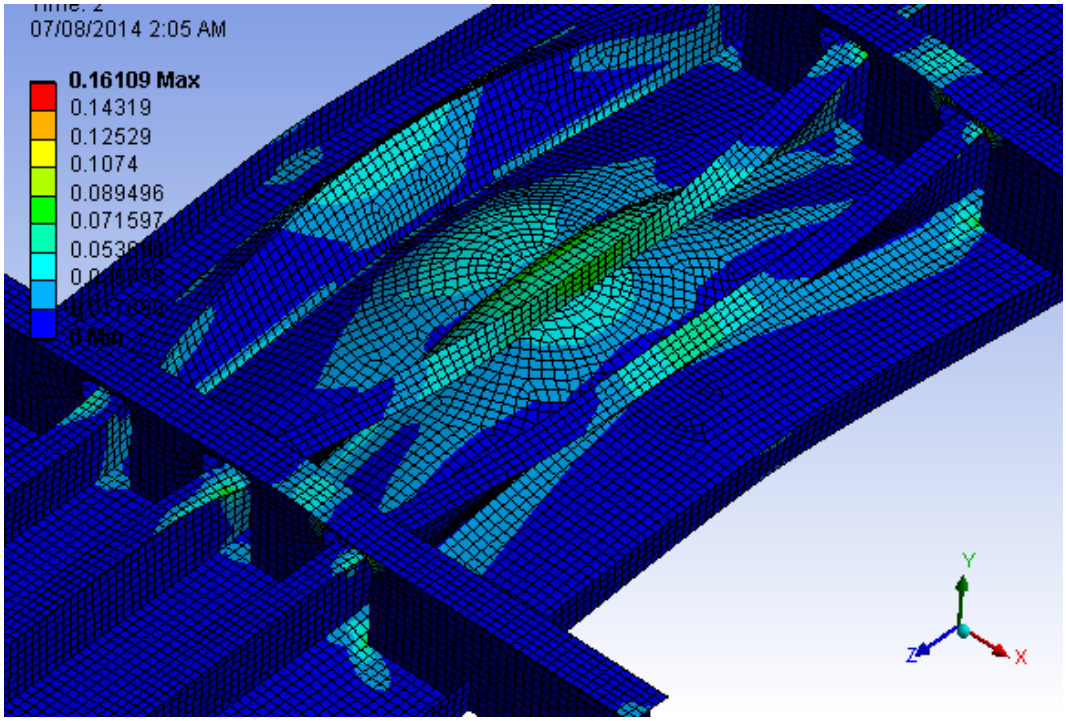

Figure 4-15: Equivalent plastic strain of G1T2 FEM at 2.8 MN

4.6.2 Grillage #2

A comparison of the experiments and FE analysis of load-deflection curves of Grillage #2 are presented in Figure 4-16. Although the FE analysis curves are slightly stiffer than the experimental results, the curves show good agreement with the experimental results of Grillage #2. The stiffness of the elastic portions of the load-deflection curves in G2T1 FEM [55 kN/mm] is similar to that of G2T1 [52 kN/mm].

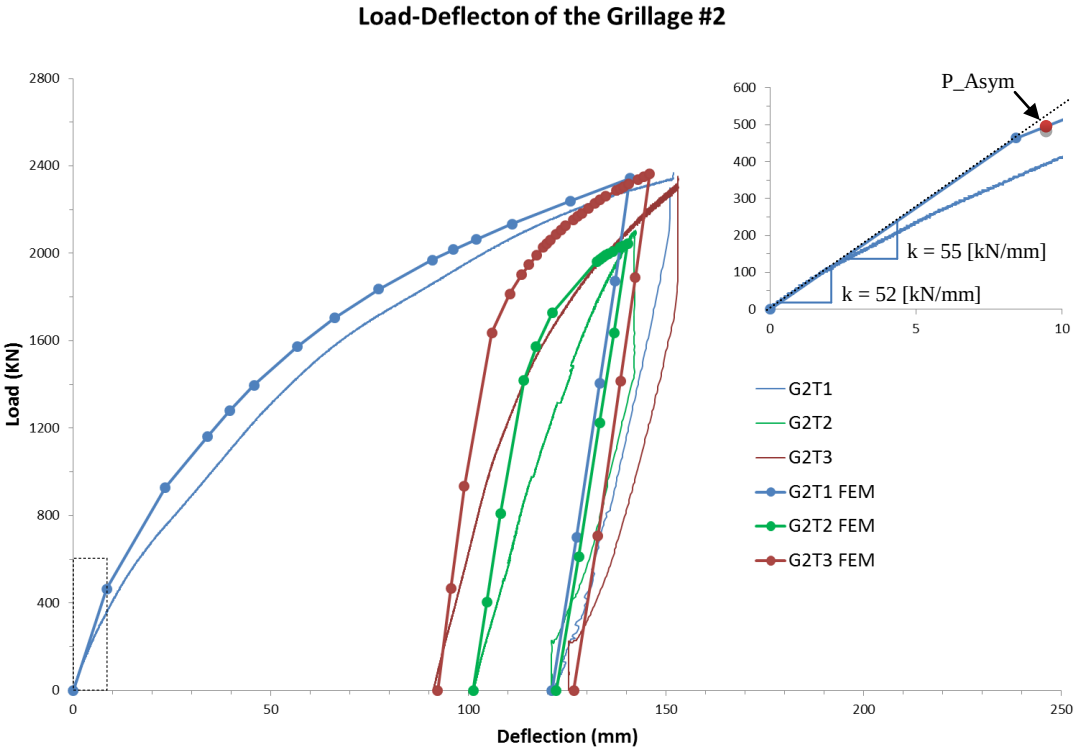

Figure 4-16: FEM load-deflection curves in comparison with experimental results

Figure 4-17 presents the comparison of cross section views of deformed shape between experimental results and FE analysis. The deformed shapes of G2T1 and G2T2 in the FEM show good agreement with experimental results. However, the deformed shape of G2T3 in the FEM shows excessive folding over behavior in the central stiffener then the experimental results.

The vertical deflection and equivalent plastic strain of the each test are shown in Figures 4-18 to 4-23.

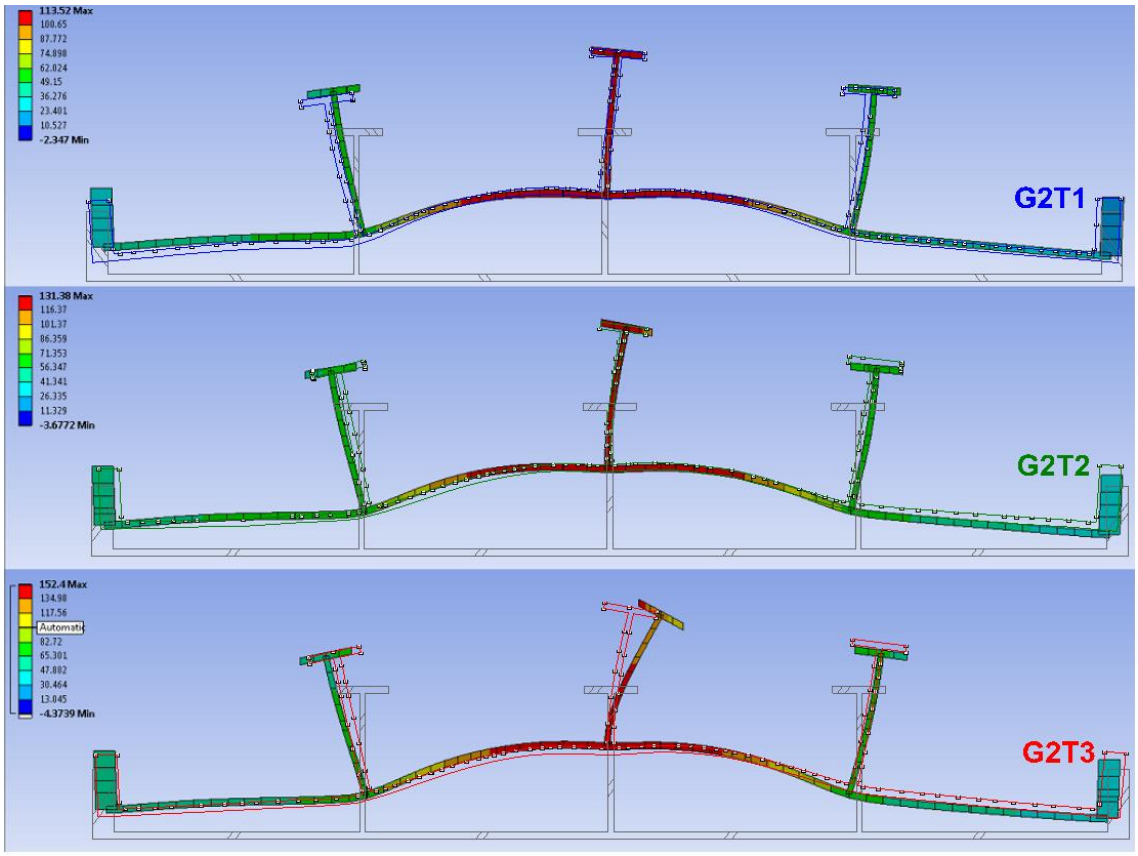

Figure 4-17: Cross section views of the FEM in comparison with the experimental results

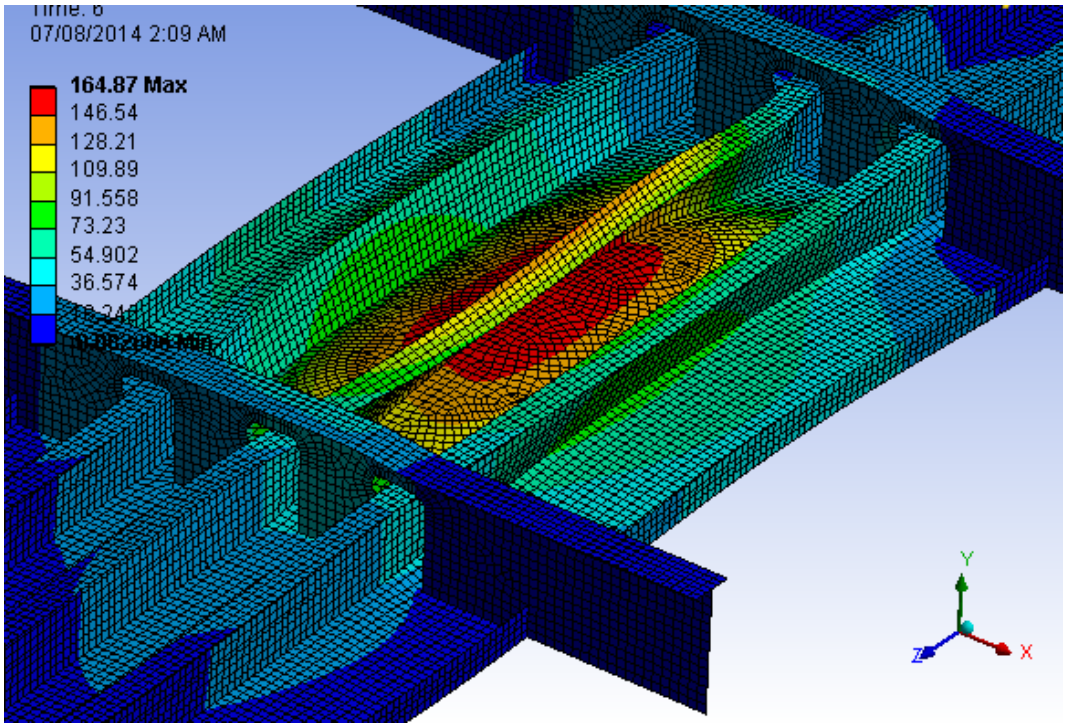

Figure 4-18: Deformation of G2T1 FEM at 2.3 MN

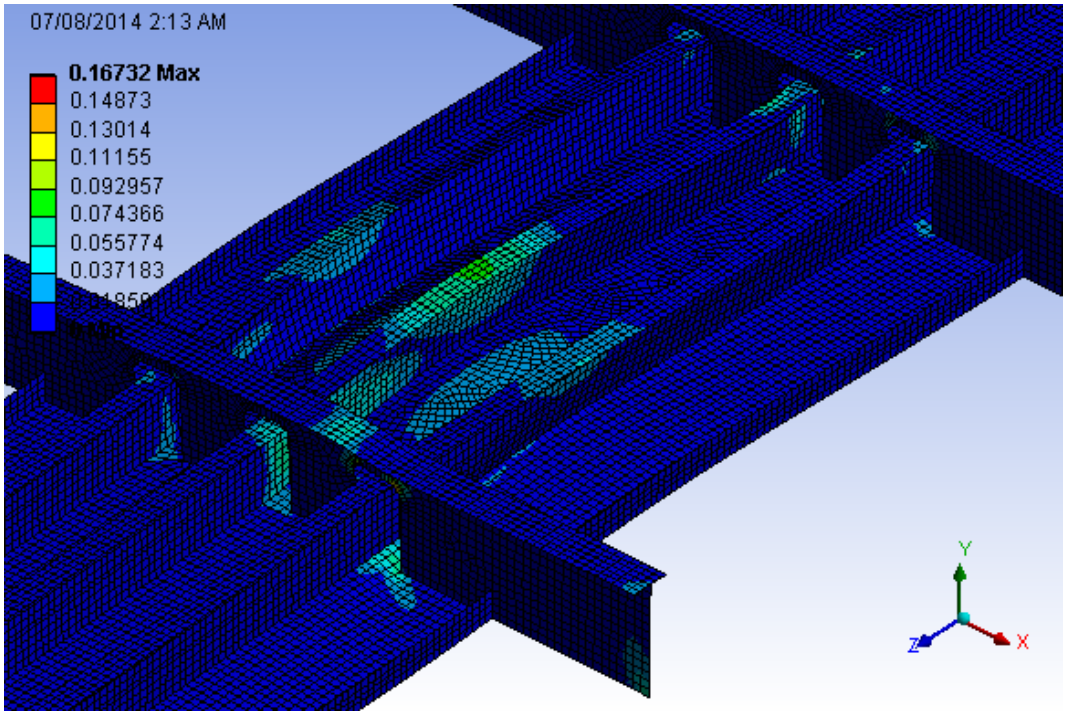

Figure 4-19: Deformed shape with equivalent plastic strain of G2T1 FEM

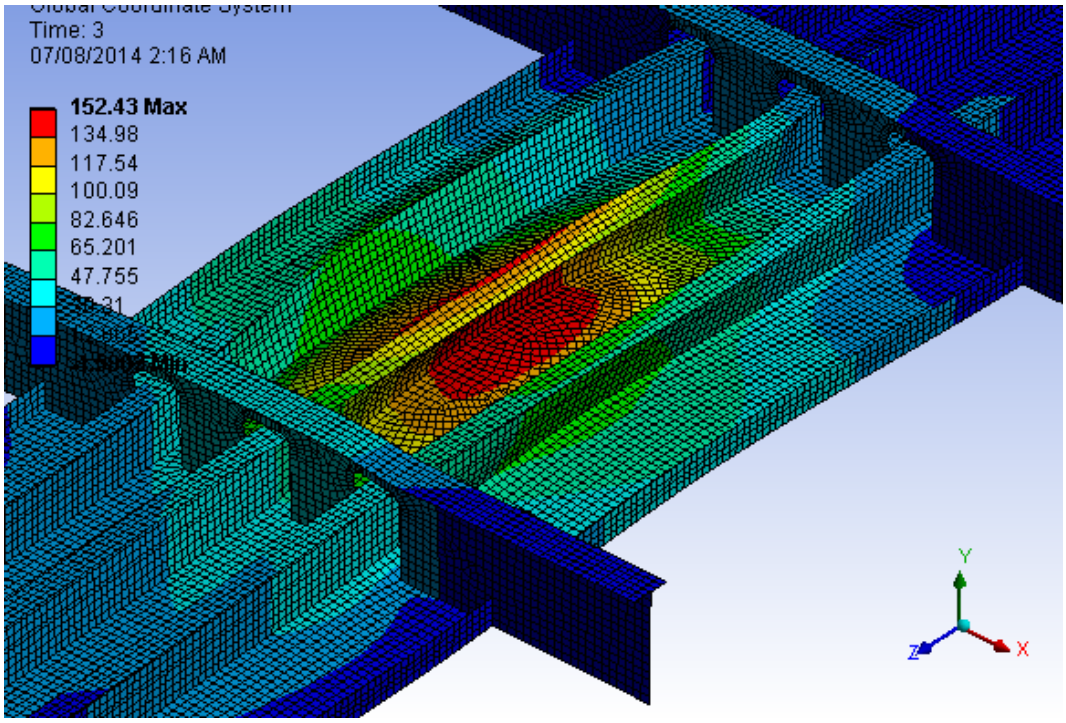

Figure 4-20: Deformation of G2T2 FEM at 2.1 MN

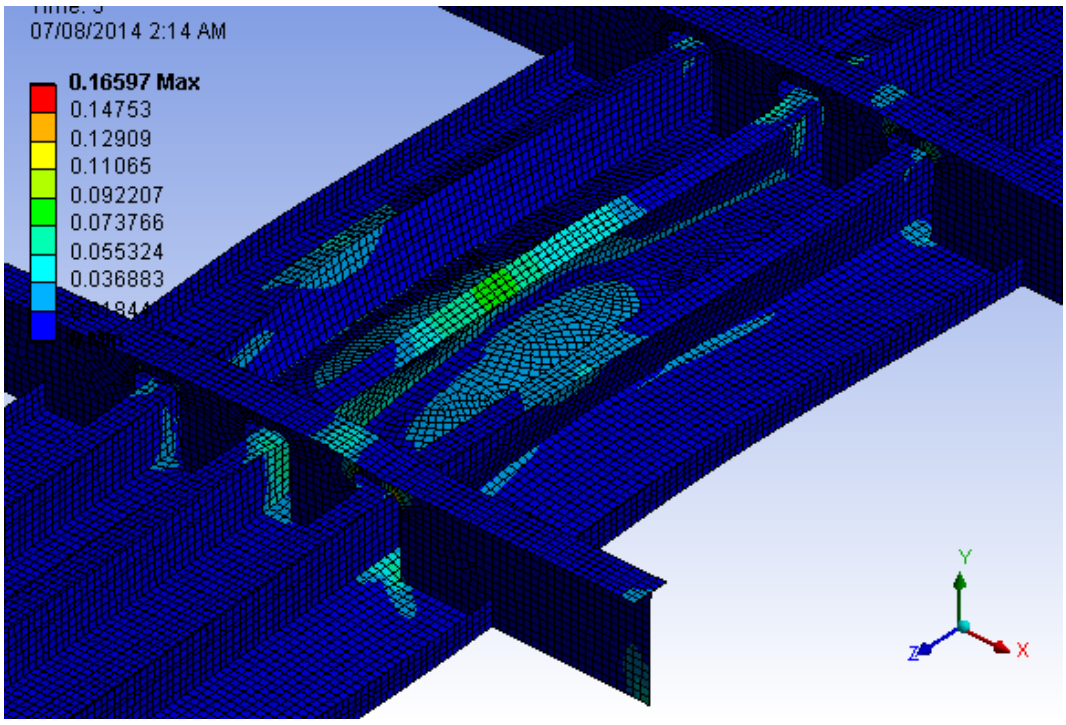

Figure 4-21: Deformed shape with equivalent plastic strain of G2T2 FEM

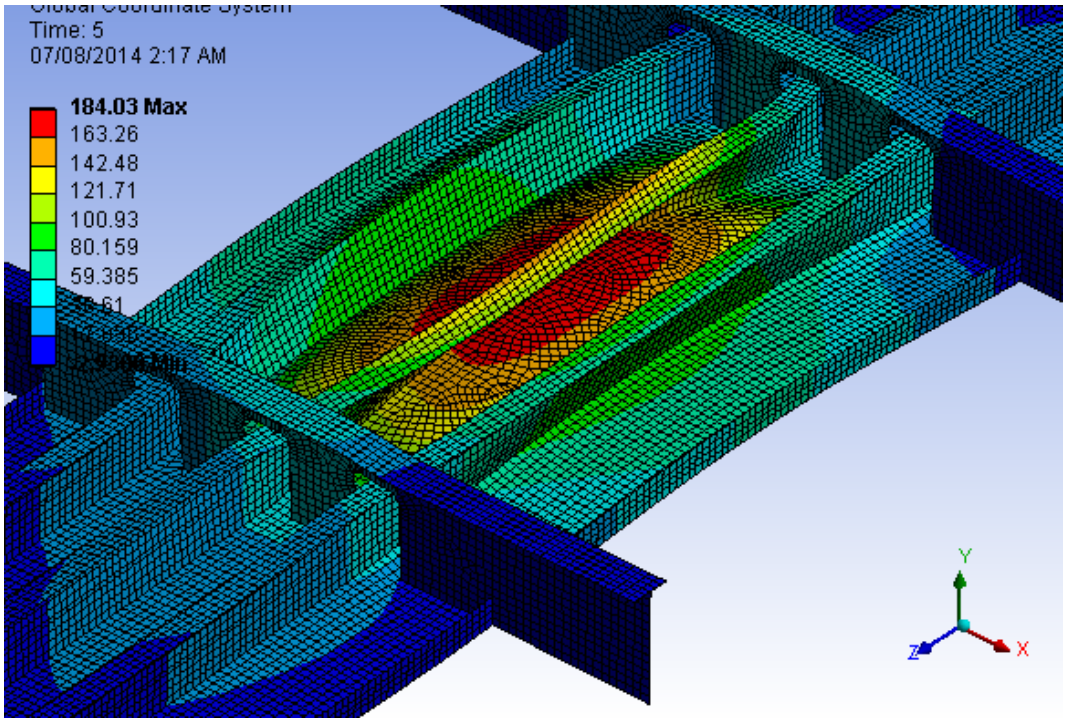

Figure 4-22: Deformation of G2T3 FEM at 2.3 MN

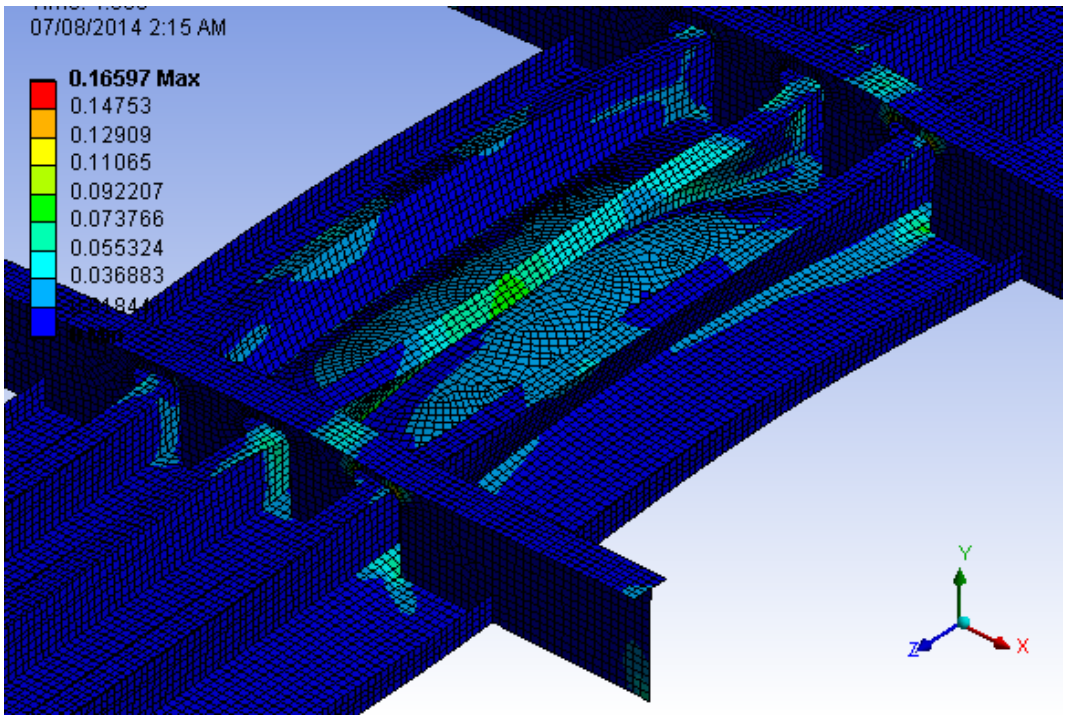

Figure 4-23: Deformed shape with equivalent plastic strain of G2T3 FEM

4.7 Conclusion

The load-deflection curves and deformation shapes measured by the MicroScribe® were used to validate the numerical results. There are a number of assumptions and simplifications considered in the FEM model of the grillage but the results shows good agreement with the physical experiments.

The load-deflection curves of the FEM show excellent agreement with the experimental results of Grillage #1 and G2T1 test. Also, the stiffness of the elastic portions of the load-deflection curves in the FEM is similar to those of G1T1 and G2T1. Although the FE analysis curves are slightly stiffer than the experimental results, the curve shows good agreement with the experimental results of Grillage #2. The stiffness of the elastic portions of the load-deflection curves in G2T1 FEM is similar to that of G2T1.

The results of the comparison of cross section views of deformed shape between experimental results and Grillage #1 FE analysis show strong agreement. The results of G2T1 and G2T2 in the FEM show that the deformations are good agreement with experimental results. However, the deformed shape of G2T3 in the FEM shows slightly excessive folding over behavior in the central stiffener relative to the experimental results. The actual unloading in experiments can be considered as an inverse loading to elastic material behavior of the structure in the FE analysis. However, the unloading of the hydraulic ram was simply treated as a decrease of measured peak load in this analysis. In addition, the ice load was applied as an uniform pressure distribution.

In reality there is a complex distribution of high and low pressure zones within the contact area. These experiments were not instrumented to capture these local pressure distributions and therefore only uniform pressures were applied.

The results showed that the FE model can be used for analysis of an ice-strengthened ship subjected to extreme ice loading. Non-linear finite element analysis can be confidently used to investigate the ultimate load-carrying capacity and the influence of variable ice loading position along a single frame. This simulation model can be useful for further related research and supportive to expand a number of other research areas.

5 CONCLUSIONS AND RECOMMENDATIONS

5.1 Conclusions

In this study, four laboratory-grown ice samples were produced and loaded onto two structural ice class grillages with a hydraulic ram (700,000 lbs capacity) at different loading positions (centre and off-centre). The ram speed was 0.5 mm/s (quasi-static condition for steel and creep behavior for ice). This allowed for a controlled investigation into large structural deformations considering the simultaneous failure of ice.

Grillage #1 tests demonstrated significant overload capacity of the grillage when subject to ice loads, with deflections up to 215 mm at the peak loading condition, despite surface cracks that initiated at the ends of the central stiffener. The limit load according to the IACS Polar Rules for this particular structure is approximately 503 kN, and the load-deflection curve shows that the overload capacity of the grillage is much greater than the required rule. The maximum load applied was 2.8 MN which is greater than 5 times the design load. The design load in the IACS Polar Rules is based on a single frame in isolation. These results indicate that a frame surrounded by adjacent frames can sustain higher loads beyond its design point while subjected to ice loading at extremely slow speeds (0.5 mm/s). Also the stiffness of the elastic portions of the load-deflection curves in the second test (83.6 kN/mm) was about 73 % higher than the first test (48.3 kN/mm). The slope in load-deflection curve implies increased resisting capacity against deformation. Thus, it can be inferred that prior deformation on the frame leads to greater resisting capacity against further plastic deformation. The intention of the experiment was to study the ultimate load-carrying capacity of the grillage; however, given the limit of

the hydraulic ram stroke it was not able to reach the maximum load before tearing or rupture. The deformation of ice may contribute to this lack of steel rupture since the load becomes more distributed. These experimental results suggest that the local deformations (up to 11 % of the frame span) do not necessarily compromise the overall strength of the large grillage. In fact the grillage actually gains stiffness and exhibits higher load-carrying capacity when there is prior deformation.

Grillage #2 load cases were carried out sequentially with fresh ice samples applied to the deformed grillage from the previous cases. It was observed that the stiffness of the elastic portions of the load-deflection curves in the second and third tests were higher than the first test. The slope in load-deflection curve which implies the resisting capacity against deformation. Thus it can be inferred that prior deformations at nearby locations on the frame lead to greater resistance to plastic deformation. The limit load for asymmetric load based on the IACS Polar Class rules for this structure is approximately 500 kN, and the load-deflection curve shows that the overload capacity of the grillage is much greater than the required rule. The maximum load applied was 2.3 MN which is greater than 4 times the design load. The varying locations of Grillage #2 tests were intended to investigate the effect of damage at nearby locations on capacity of the structure. These experiments suggest that prior plastic deformations at nearby locations do not necessarily compromise the overall strength of the grillage.

The pressure-area relationships vary depending on methods of the measurement of contact area. A decreasing trend of pressure was shown as the nominal contact area increases but an increasing trend was observed in G2T2. The process pressure-area

relationships considering the structural deformation of Grillage #1 show relatively constant trend of pressure as the nominal contact area increases. On the other hand, diverse trends that decreasing, constant and increasing trend of pressure are shown in Grillage #2 as the nominal contact area increases in the three tests. The pressure in G2T1 and G2T3 are relatively constant but the pressure in G2T2 was observed an increasing trend. Average pressure and direct measured contact area are placed within the force of 2.1 ~ 2.8 MN since this data is limited by a level of force. The pressure-area results of the physical experiments are compared with an assemblage of other experiments and full scale data sets prepared by Daley (2004). The comparison demonstrates that these experiments fall within the general envelop of existing, particularly for smaller contact areas. However, it also shows the uncertainty and sensitivity of measurement methods in the use of pressure-area to describe ice loads on deforming structures.

Ten uniaxial material tensile tests were conducted to determine the material properties of the steel used in the fabrication of the large grillage structure. The yield stress, Young's modulus and limit strains for the specimens are presented. However, the properties of the steel show relatively higher value than typical steel for ship structures. Typical steel property lies within the range 235 MPa to 355 MPa depending on the grade and type.

The load-deflection curves and deformation shapes measured by the MicroScribe® were used to validate the numerical results. There are a number of assumptions and simplifications considered in the FEM model of the grillage but the results shows good agreement with the physical experiments.

The load-deflection curves show excellent agreement with the experimental results of Grillage #1 and G2T1 test. Also, the stiffness of the elastic portions of the load-deflection curves in the FEM is similar to that of G1T1. Although the FE analysis curves are slightly stiffer than the experimental results, the curve shows good agreement with the experimental results of Grillage #2. The stiffness of the elastic portions of the load-deflection curves in G2T1 FEM is similar to G2T1.

The results of the comparison of section views of deformed shape between experimental results and Grillage #1 FE analysis show strong agreement. The results of G2T1 and G2T2 in the FEM show that the deformations are good agreement with experimental results. However, the deformed shape of G2T3 in the FEM shows slightly excessive tripping behavior in the central stiffener relative to the experimental results. The actual unloading in experiments can be considered as an inverse loading to elastic material behavior of the structure in the FE analysis. However, the unloading of the hydraulic ram was simply treated as a decrease of measured peak load in this analysis. In addition, the ice load was applied as an uniform pressure distribution.

In reality there is a complex distribution of high and low pressure zones within the contact area. These experiments were not instrumented to capture these local pressure distributions and therefore only uniform pressures were applied.

The results showed that the FE model can be used for analysis of an ice-strengthened ship subjected to extreme ice loading. Non-linear finite element analyses can be confidently used to investigate the ultimate load-carrying capacity and the influence of variable ice loading position along a single frame. This simulation model can be useful for further related research and supportive to expand a number of other research areas.

In summary, the laboratory experiments and associated numerical modeling have shown midbody icebelt structures in compliance with the IACS Polar Rules are capable of significant overload capacity in the quasi static loading condition. The strong correlation with numerical results increases the confidence in our ability to predict plastic response and quantify this reserve capacity. Using some portion of the reserve capacity can lead to the design of more efficient and lighter structures rather than using traditional working stress methods. Ultimately, the application of these findings can support a higher level of safety for ships designed for operations in ice covered water.

5.2 Recommendations

This work has led to a number of areas of recommended future work and possible enhancements to similar experiments.

1) It is desirable to use a 3D scanner to acquire more accurate deformation shape of structures and save time. The MicroScribe® measurement processes is time consuming and laborious.
2) It is recommended to develop a more advanced ice load model for simulation. In this study, idealized and simplified static ice loads were used for the simulation. An explicit deformable ice load model or a further defined spatial pressure distribution is necessary to expand research regarding interactions between ice and ship structures (Gagnon, 2007).

3) It is recommended that the developed simulation model can be used to investigate optimization of different geometries and structural arrangements and their influence to plastic capacity, structural stability, and possibly manufacturing costs.

4) These tests were performed at room temperature conditions. It is assumed that the temperature affects the results of the test. It is recommended that the effect of temperature on the capacity of the grillage and strength of the ice be further investigated.

5) These experiments were performed under extremely slow speed (0.5 mm/s) so it is recommended that experiments are carried out in which an ice sample collides with structures at speed more realistic to ship operations. Such experiments are planned within the STePS^2 research project in the large double pendulum apparatus.

6) This study considered only lateral loads but ship (and offshore) structures are likely to be subjected to various types of ice loading scenarios. It is recommended that multiple loading conditions such as combined axial compression and lateral loads are used for a grillage test.

7) Large deformations were observed in a cut-out of the stringer which is the major supporting member for the stiffeners. The IACS Polar Rules do not explicitly provide criteria for stringers and other major supporting members. Each classification society's rules are expected to provide criteria for these members. It is recommended that further studies on the major supporting member's capacity and the influence of stiffeners and other secondary members are necessary to complete the Unified Requirements.

8) The intention of the experiment was to study the ultimate load-carrying capacity of the grillage; however, given the limit of the hydraulic ram stroke it was not able to reach the maximum load before tearing or rupture. It is recommended that a grillage test apparatus which is capable of reaching the ultimate load is necessary to determine the ultimate load-carrying capacity.

Bibliography

Abraham, J. (2008). *Plastic response of ship structure subjected to ice loading* (Master's thesis). Memorial University of Newfoundland, St.John's, NL.

ABS (2004). Guidance Notes on Nonlinear Finite Element Analysis of Side Structures Subject to Ice Loads. Houston, TX, USA: American Bureau of Shipping.

Alam, M.S. et al. (2012). Double pendulum dynamic impact test set-up for ice-grillage collision, *International Conference and Exhibition on Performance of Ships and Structures in Ice, IceTech'12*, ICETECH12-134-RF, Banff, AB, Canada.

ANSYS (2011). User's manual (Release 14.0), ANSYS Inc.

Belenkiy, L. & Raskin, Y. (2001). Estimate of the ultimate load on structural members subjected to lateral loads, *Marine Technology, Vol. 38. No. 3*, pp. 169-176.

Bond, J., & Kennedy, S. (1998). Physical testing and finite element analysis of icebreaking ship structures in the post yield region. In *Proceedings of the International Offshore and Polar Engineering Conference* (Vol. 2, pp. 577–585). ISOPE. Retrieved from http://www.scopus.com/inward/record.url?eid=2-s2.0-0031635877&partnerID=tZOtx3y1

Bruneau, S., Colbourne, B., Dragt, R., Dillenburg, A., Ritter, S., Pilling,M., Sullivan, A. (2013). Laboratory indentation tests simulating ice-structure interactions using cone-shaped ice samples and steel plates. *Port and Ocean Engineering under Arctic Conditions, POAC'13*. Espoo, Finland.

Clarke, G. (2012). *Ice collision with a Pendulum Impact Apparatus* (Master's thesis). Memorial University of Newfoundland, St.John's, NL.

Daley, C. & Hermanski, G. (2005). *Ship Frame/Grillage Research Program- Investigation of Finite Element Analysis Boundary Conditions, Memorial University OERC Report 2005-02 and NRC/IOT Report TR-2005-05.*

Daley, C. (2004). *A study of the process-spatial link in ice pressure-area relationships, NRC PERD/CHC Report, pp. 7-108.*

Daley, C. G. & Hermansk.i., G. (2008a). *Ship frame research program · an experimental study of ship frames and grillages subjected 10 patch loads, volume 2 - theory and analysis reports. Ship Structure Committee, SSC Project SR 1442 • Final Report; OERC Report 2008-00 I; NRC-lOT Report TR-2oo8-11.*

Daley, C. G., & Hermansk.i., G. (2008b). *Ship frame research program · an experimental study of ship frames and grillages subjected to patch loads, volume I • data report. Ship Structure Committee, SSC Project SR 1442- Final Report; OERC Report 2008-001; NRC-lOT Report TR·2008-11.*

Daley, C.G. (2000). *IACS Unified Requirements for Polar Ships - Background Notes to Design Ice Loads*.

Daley, C.G. (2002). Application of Plastic Framing Requirements for Polar Ships, *Journal of Marine Structures, Elsevier, 15(6),* pp 533-542.

Daley, C.G. (2002). Derivation of Plastic Framing Requirements for Polar Ships, *Journal of Marine Structures, Elsevier, 15(6),* pp 543-559.

Daley. C. G. (2001). Oblique ice collision loads on ships based on energy methods, *Oceanic Engineering International, Vol. 5(2),* pp. 67-72.

FMA (2002). *Finnish-Swedish Ice Class Rules,* Finnish Maritime Administration.

Gagnon, R. E., & Derradji-Aouat, A. (2006). First Results of Numerical Simulations of Bergy Bit Collisions with the CCGS Terry Fox Icebreaker. *IAHR International Symposium on Ice, IAHR'06* (pp. 9–16). Sapporo, Japan.

Gautier, D.L. et al. (2009). Assessment of Undiscovered Oil and Gas in the Arctic, *Science, Vol. 324 no. 5931*, pp. 1175-1179. DOI: 10.1126/science.1169467.

GoPro Hero2. (2011). User's manual, GoPro.Inc.

Hughes, O. (1983). *Ship structure design: A rationally-based, computer-aided, optimization approach*. New Jersey, NY: The Society of Naval Architects and Marine Engineers.

IACS (2007). *Requirements concerning polar class*. London: International Association of Classification Societies.

Kendrick, A. & Daley, C.G. (1998). *Unified Requirements Load Model - 'Synthesized Approach', Prepared for IACS Polar Rules Harmonization, Semi-Permanent Working Group, Prepared by, AMARK Inc, Montreal and Memorial University, St. John's.*

Kendrick, A. & Daley, C.G. (2000). *Derivation and Use of Formulation for Framing Design in the Polar Class Unified Requirements, Prepared for IACS Ad-hoc Group on Polar Class Ships and Transport Canada.*

Kendrick, A. (2000). *IACS Unified Requirements for Polar Ships - Background to Definition of Polar Classes.*

Kozarski, N. (2005). *Importance of Strain Hardening in Plastic Response of Rectangular Beams subjected to Bending Loads* (Master's thesis). Memorial University of Newfoundland, St.John's, NL.

MicroScribe® 3-D Digitizers, User's manual, Solution Technologies Inc.

Paik, J.K & Thayamballi, AK. (2003). *Ultimate limit state design of steel-plated structures*., Chichester, UK: Wiley.

Pavic, M., Daley, C., Hermanski, G., & Hussein, A. (2004). *Ship Frame Research Program- A Numerical Study of the Capacity of Single Frames Subject to Ice Load, Memorial University OERC Report 2004-02 and NRC/IOT Report TR-2004-04.*

Popov, Y. N., Faddeyev, O. V, Kheysin, D. Y., & Yakovlev, A. A. (1967). *Strength of Ships Sailing In Ice (Translated), F3TC-HT-23-96-68* (Technical.). Leningrad, USSR: Sudostroyeniye Publishing House.

Quinton, B. W. (2009). *Progressive damage to a ship's structure due to ice loading* (Master's thesis). Memorial University of Newfoundland, St.John's, NL.

Reddy, P.S., Colbourne, B., Daley, C. Bruneau, S.E., & Gagnon, R. (2012). Strength and Pressure Profiles from Conical Ice Crushing Experiments. *International Conference and Exhibition on Performance of Ships and Structures in Ice, IceTech'12*, Paper No. ICETECH12-132-RF, Banff, AB, Canada.

SolidWorks (2010). SolidWorks help, Dassault Systèmes.

Transport Canada (1995). *Equivalent Standards for the Construction of Arctic Class Ships, TP12260.*

Appendix A: Load-Strain Curves of Grillage #1

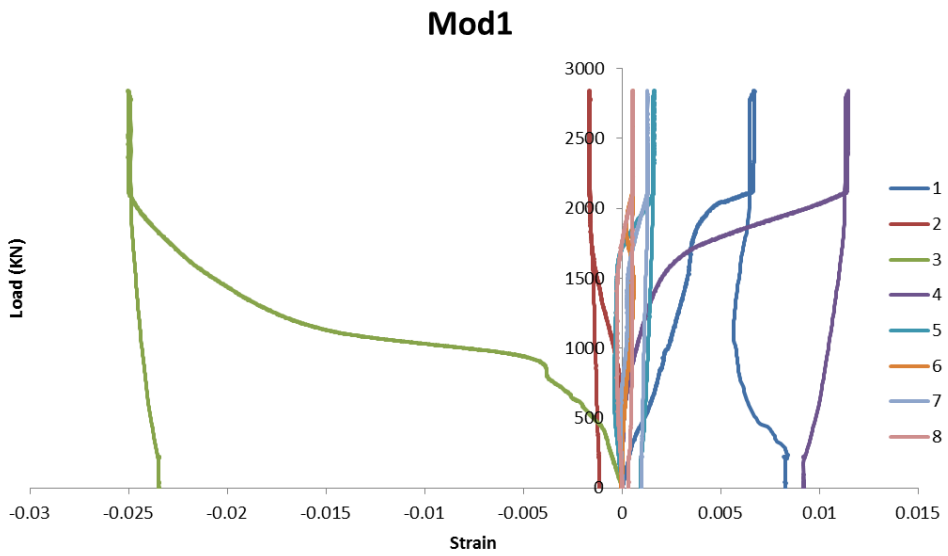

Figure A- 1: Module 1 of G1T1

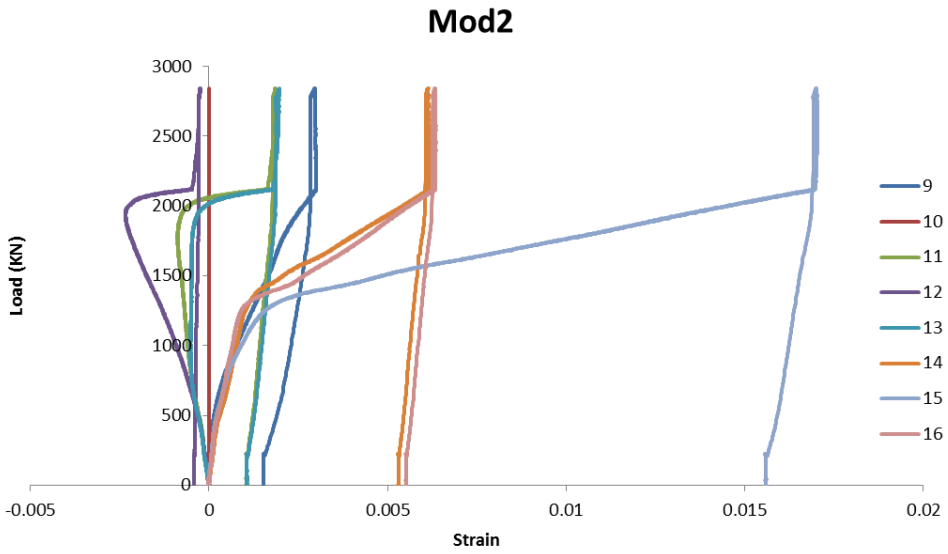

Figure A- 2: Module 2 of G1T1

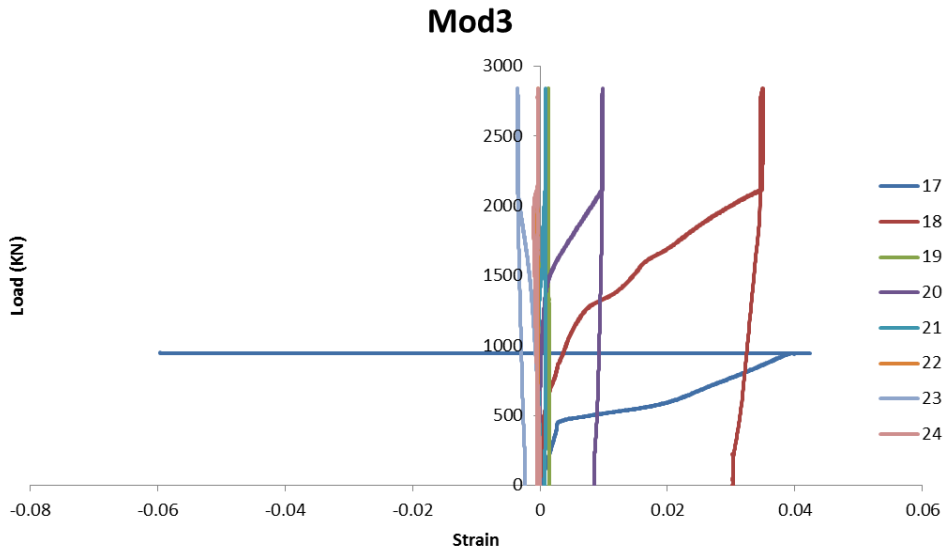

Figure A- 3: Module 3 of G1T1

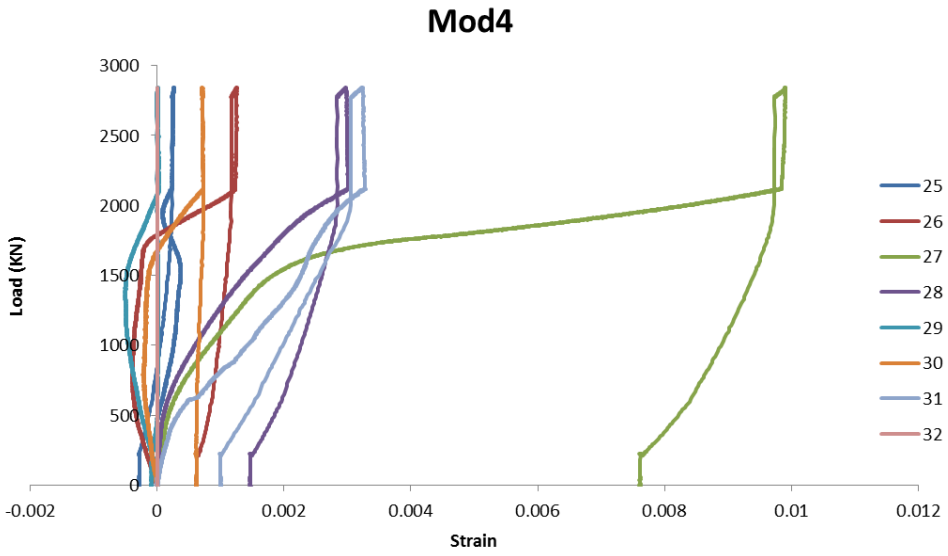

Figure A- 4: Module 4 of G1T1

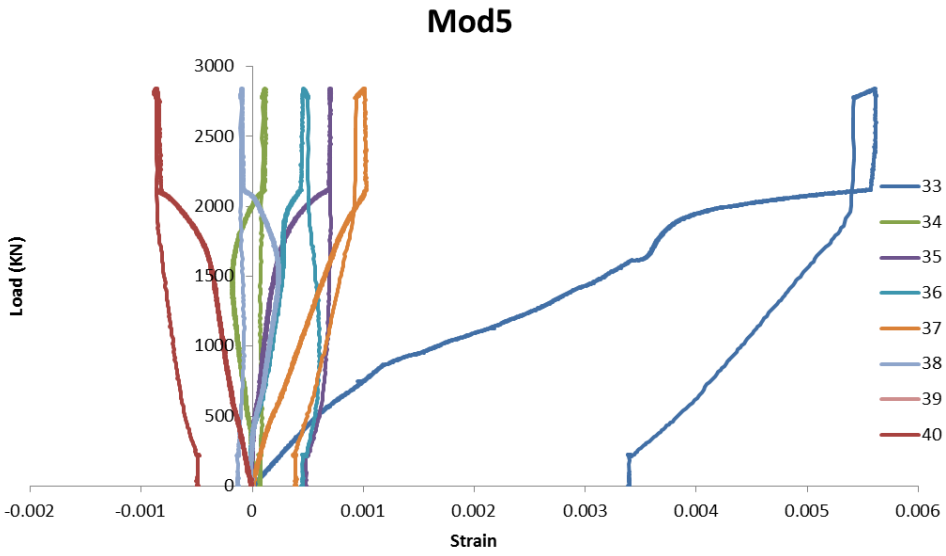

Figure A- 5: Module 5 of G1T1

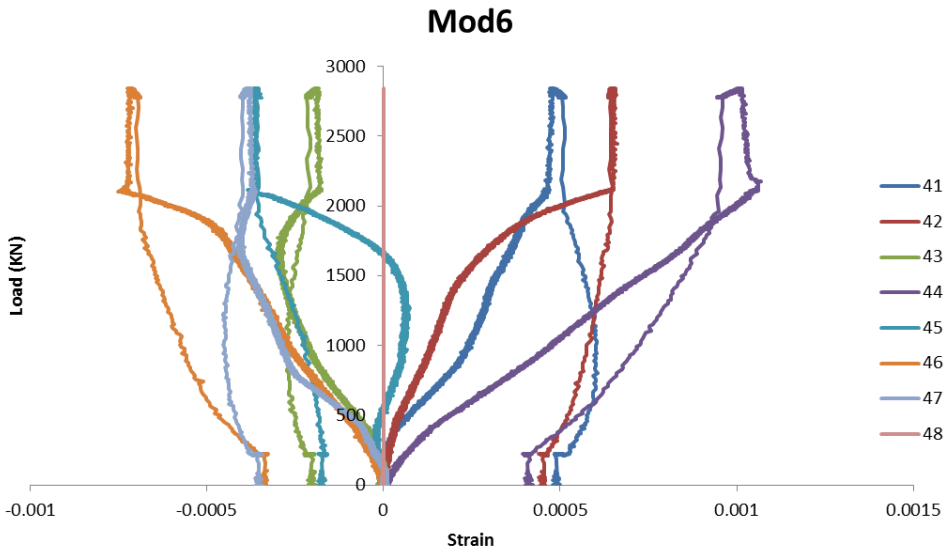

Figure A- 6: Module 6 of G1T1

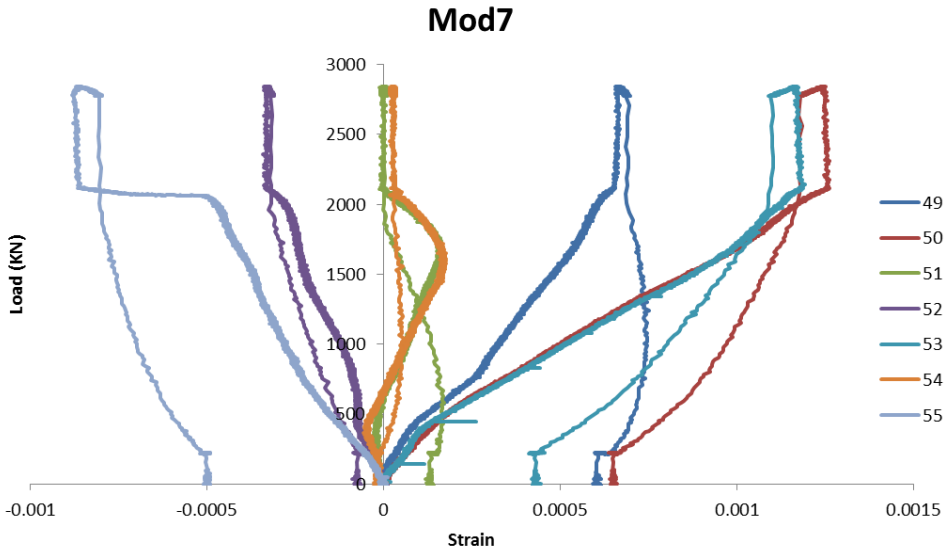

Figure A- 7: Module 7 of G1T1

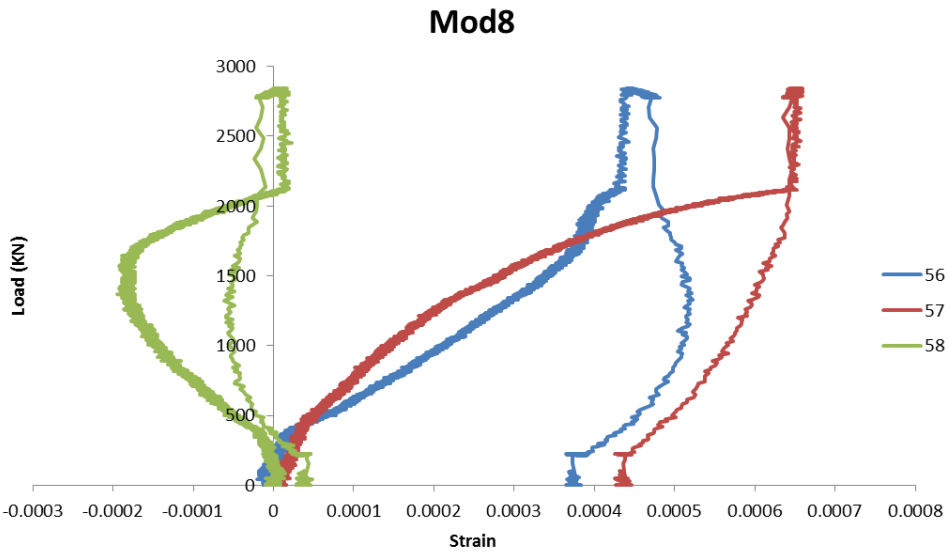

Figure A- 8: Module 8 of G1T1

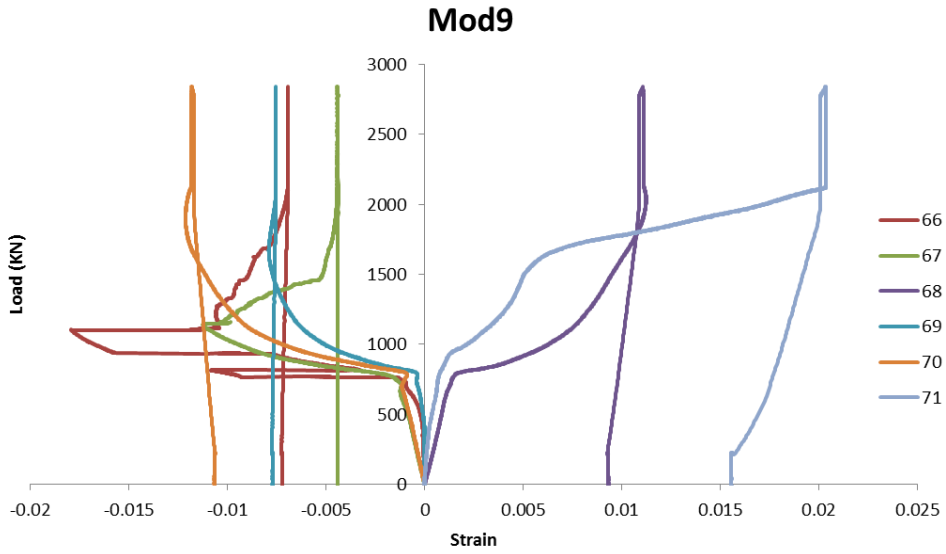

Figure A- 9: Module 9 of G1T1

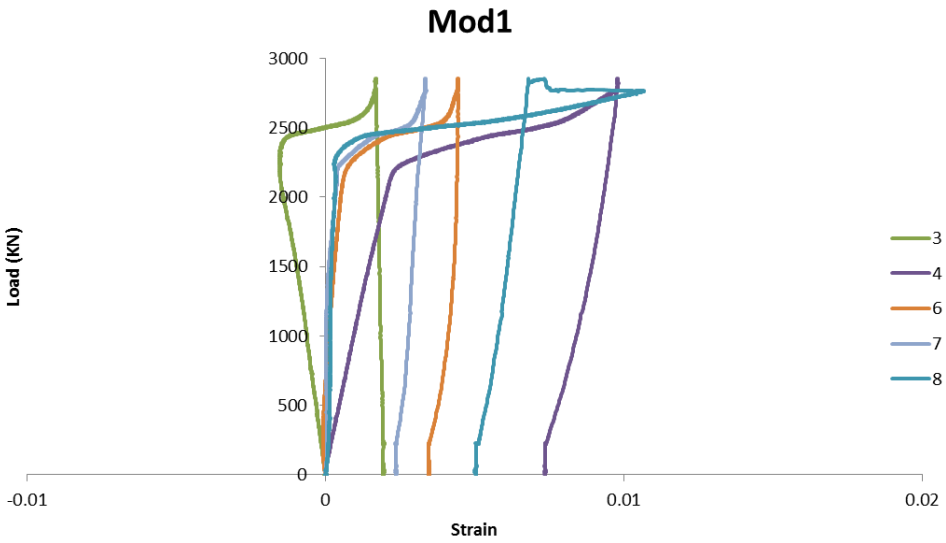

Figure A- 10: Module 1 of G1T2

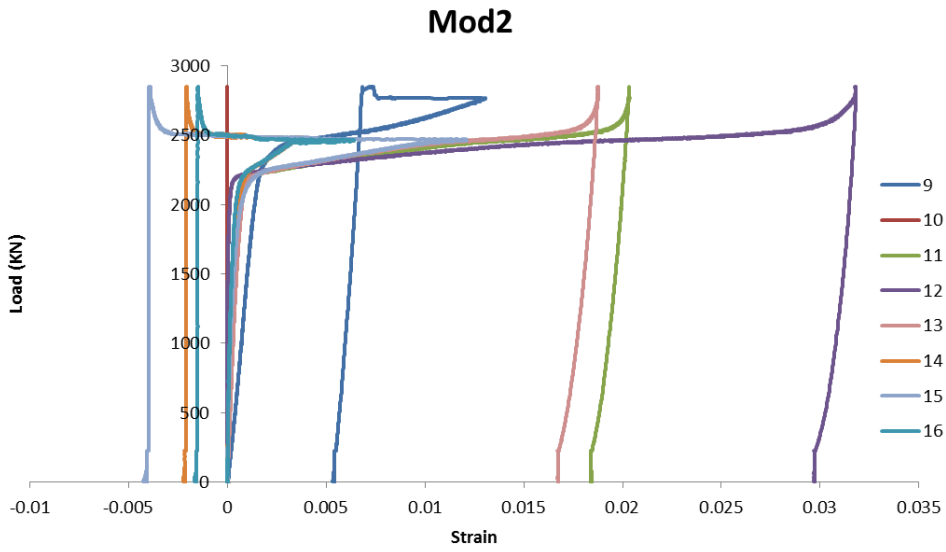

Figure A- 11: Module 2 of G1T2

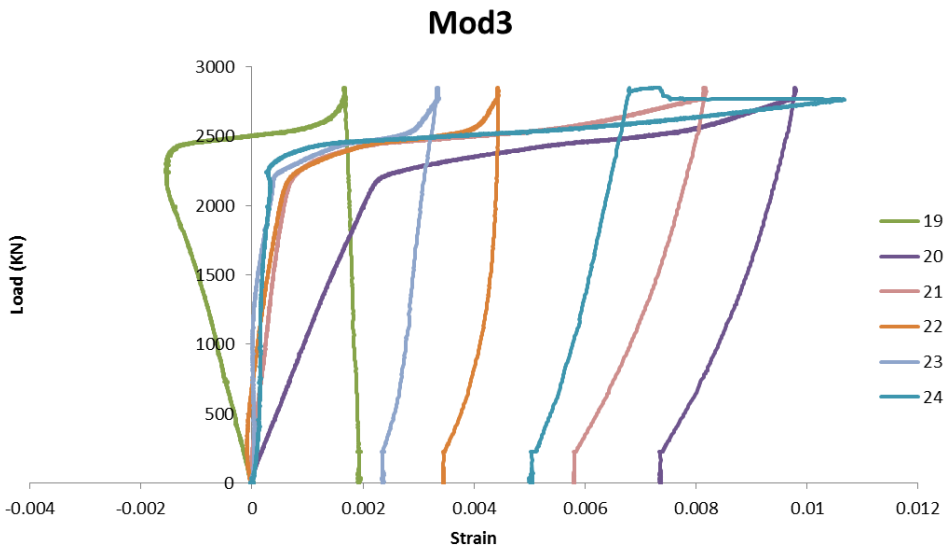

Figure A- 12: Module 3 of G1T2

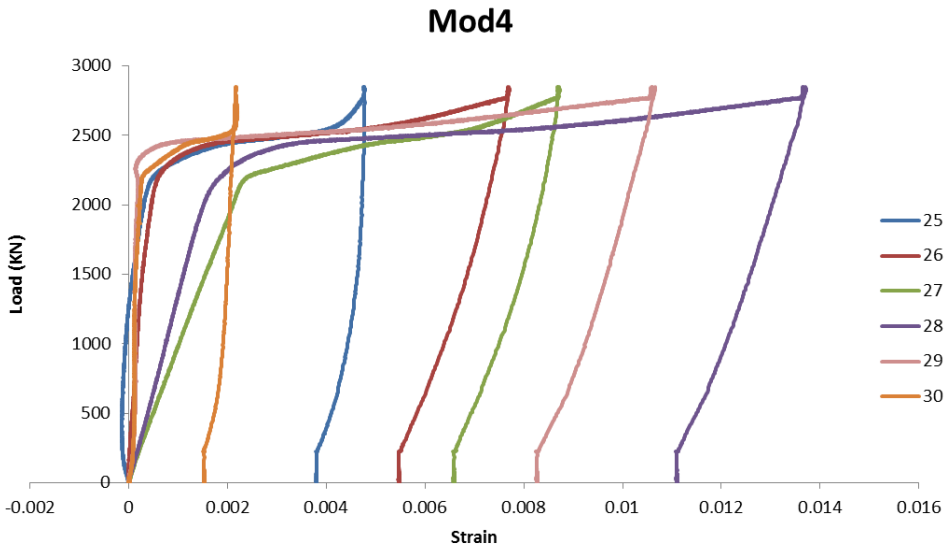

Figure A- 13: Module 4 of G1T2

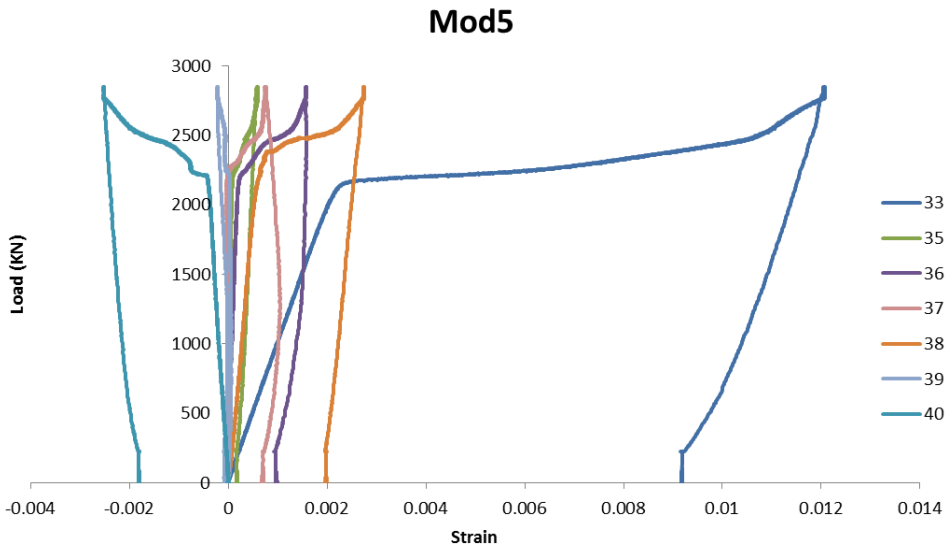

Figure A- 14: Module 5 of G1T2

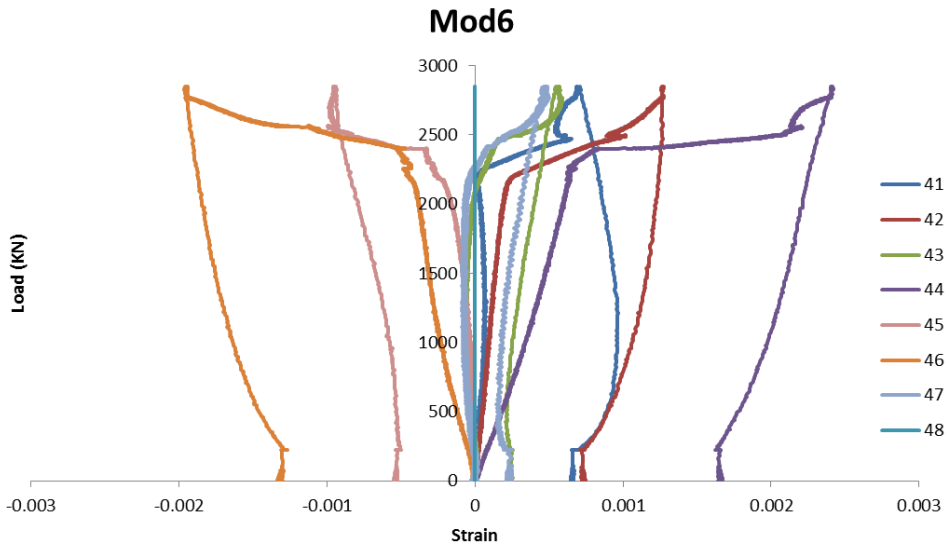

Figure A- 15: Module 6 of G1T2

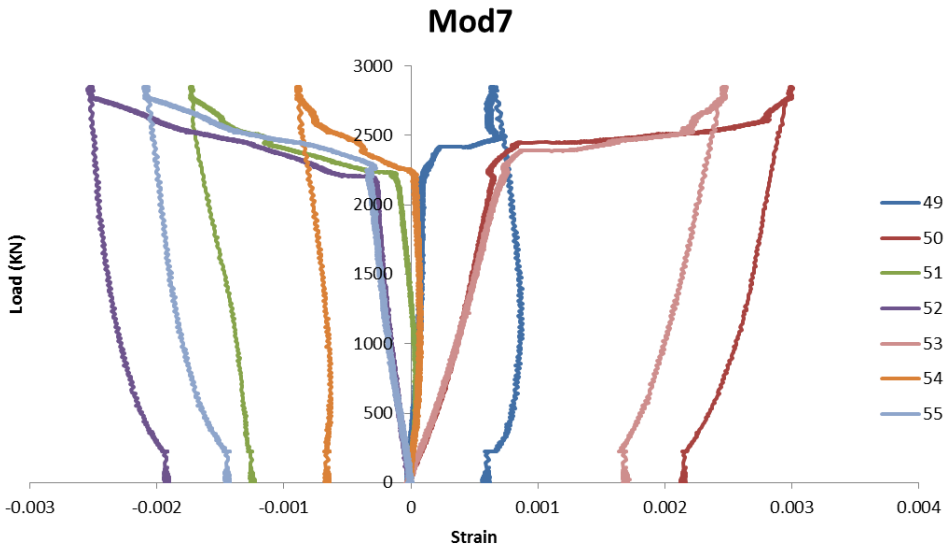

Figure A- 16: Module 7 of G1T2

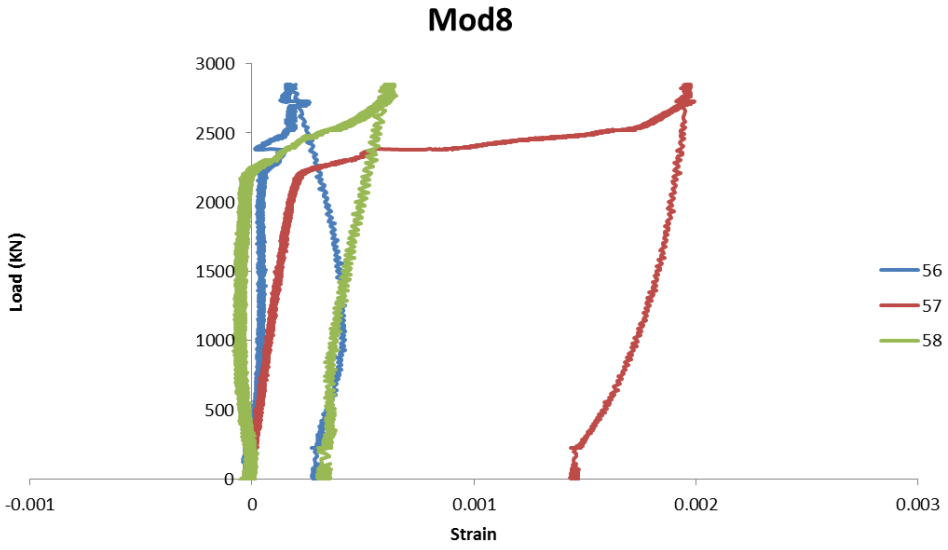

Figure A- 17: Module 8 of G1T2

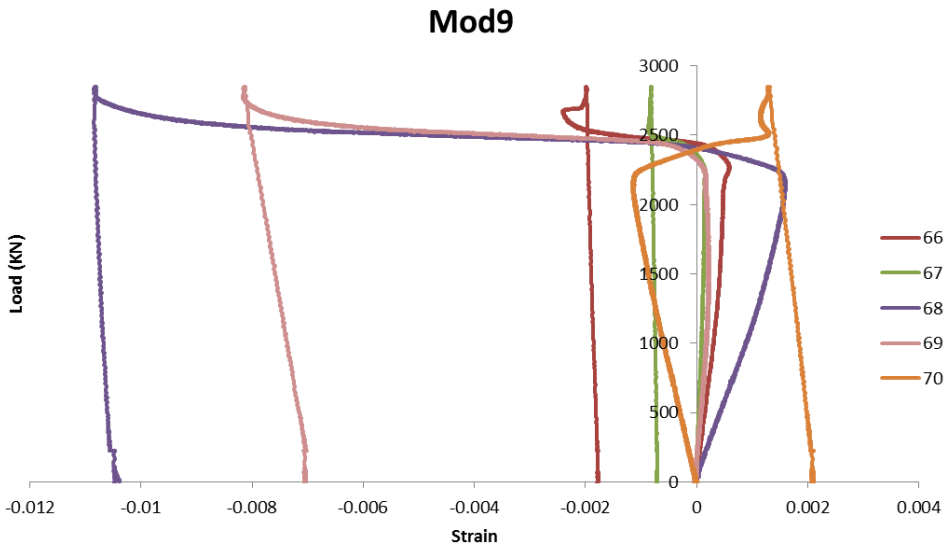

Figure A- 18: Module 9 of G1T2